BAND GAP ENGINEERING STUDIES OF PBTE, SNTE, AND CDSETE FOR CDTE SOLAR CELL APPLICATIONS

by

Elizabeth G. LeBlanc, M.S.

A dissertation submitted to the Graduate Council of
Texas State University in partial fulfillment
of the requirements for the degree of
Doctor of Philosophy
with a Major in Material Science, Engineering, and Commercialization
August 2020

Committee Members:

Thomas Myers, Chair

Matthew Reese

Luisa Scolfaro

Mark Wistey

Alexander Zakhidov

FAIR USE AND AUTHOR'S PERMISSION STATEMENT

Fair Use

Duplication Permission

ACKNOWLEDGMENTS

First, I would like to thank my dissertation committee, Dr. Tom Myers, Dr. Matt Reese, Dr. Luisa Scolfaro, Dr. Mark Wistey, and Dr. Alex Zakhidov, for their guidance and patience with me through this process. I would like to thank Dr. Myers in particular, for pushing me to work on things when I did not understand their importance, but later greatly helped produce this finished product.

I would also like to thank all my research collaborators – both those at other institutions such as NREL and First Solar, and those on my research team at Texas State University. Science is performed best when there is a team effort, and I am incredibly grateful for all the contributions to this work from the vast team of researchers I have had the pleasure of collaborating with.

A special thanks to my previous mentors, Dr. Eleanor Close, Dr. Hunter Close, and Dr. David Donnelly, who were integral to my education. Not only were these exceptional professors in my education, they also taught me to believe in my own capabilities and strive for more. I firmly believe that without their influence, I would not be where I am today.

It would be remiss if I did not also thank my friends and family for their support through all these years. I am particularly grateful for my amazing wife, Renee Chamberlain, for being so patient with me as I finished my schoolwork.

Finally, I want to thank my therapist. There is an alarmingly high rate of depression in graduate students, and I know I would not have been able to finish my degree without the amazing support my therapist provided.

TABLE OF CONTENTS

Page

LIST OF TABLES

Table **Page**

LIST OF FIGURES

Figure **Page**

ABSTRACT

In an environment of growing energy consumption, the demand for cost effective and efficient approaches to renewable energy is on the rise. One of the leading possible alternatives is solar cell technology. Thin film solar cells made of cadmium telluride (CdTe) have gained in popularity recently since they offer a unique solution to both increase the efficiency of solar cells and decrease costs associated with manufacturing. However, CdTe solar cells have not yet reached their theoretical efficiency ceiling, mainly due to suboptimal engineering at the back contact of the device. To address this, we study the band gap using luminescence measurements, as well as the positions of the valence band and conduction band using X-ray photoemission spectroscopy (XPS) in three material systems: lead telluride (PbTe), tin telluride (SnTe) and cadmium selenium telluride (CdSeTe) alloys in the context of CdTe. In this work, PbTe and SnTe are introduced as back contact buffer layers in various CdTe structures. The valence band offset (VBO) of PbTe/CdTe and SnTe/CdTe is explored with XPS and found to be 0.34 eV and 1.25 eV, respectively. Effects of doping levels in the PbTe and SnTe layers are studied using Hall measurements, time-resolved photoluminescence (TRPL), and photoluminescence intensity measurements (PLI). Hall investigations led to the measurement of a two-dimensional electron gas in the PbTe films. Effects of the inclusion of the buffer layers on the overall CdTe solar cell device are evaluated using current-voltage (JV) analysis at room temperature. PbTe/CdTe band alignments were also calculated for various doping concentrations in the PbTe film and agreed well with all

other measurement techniques. Potential CdTe solar cell device improvement with the inclusion of a PbTe back contact buffer layer is highly dependent on the carrier concentrations in both the PbTe layer and the CdTe layer. XPS measurements and JV measurements at different temperatures with SnTe layer unequivocally show that SnTe is not a suitable material for use in CdTe solar cells.

Some in industry have abandoned the traditional cadmium sulfide (CdS)/CdTe (n-p) junction of CdTe devices in favor of a $CdSe_xTe_{1-x}$ layer where the Se content (x-value) varies from 1 to 0 through the absorber layer of the device. While these devices have shown improved performance, the dynamics of the valence and conduction band as the Se content changes is not well understood. Here, we explore these dynamics with the use of XPS, photoluminescence spectroscopy (PL spectroscopy), energy dispersive x-ray spectroscopy (EDS), and x-ray diffraction (XRD) on a series of uniform $CdSe_xTe_{1-x}$ alloys, with varying x-values. PL spectroscopy and ellipsometry results consistently show a band gap of 1.67 eV for cubic CdSe. An alternative ternary VBO determination technique was developed for the CdTe/CdSeTe system which eliminated the need to accurately determine the valence band minimum – a significant source of error in more VBO determinations. XPS results predict a VBO between CdTe/CdSe of -0.487 eV.

1. INTRODUCTION

In an environment of growing energy consumption that relies primarily on finite oil and gas resources, cost effective and efficient approaches to renewable energy are in high demand across the globe. One of the leading alternative energy sources is solar cell technology. Gallium Arsenide (GaAs)-based solar cell technology is among the most highly efficient available, but high manufacturing costs limits its use to space-based and Department of Defense operations. As of August, 2018, silicon (Si), in its various forms, dominated the global market share capturing 95% of all photovoltaic (PV) technologies.[1] While Si is fairly cheap and readily available, its inherent material characteristics are not ideal for solar cell applications. Si has an indirect band gap, requiring thick layers of material for adequate absorption. These thick layers of material must also be of very high purity to achieve the long diffusion lengths necessary for charge carrier collection in the thick device. Cadmium telluride (CdTe) however, has physical properties that should allow it to surpass efficiency metrics of Si based solar cells. Thin film PV devices made of CdTe have achieved an equivalent cost/Watt as Si, while at one to two orders of magnitude smaller production scale suggesting that at greater scale, CdTe devices would be much cheaper per Watt than Si.[2] Despite this, thin film PV CdTe devices currently only hold about 2.5% of the global market share.[1]

CdTe is a II-VI semiconductor that has been a successfully used as a thin film solar cell material, with desirable intrinsic material properties for PV applications. Of most importance, it has a direct band gap of 1.51 eV, which is near the maximum of the Shockley-Queisser (SQ) limit.[3] The SQ limit predicts the maximum theoretical efficiency of a single junction solar cell based on the band gap and light absorption properties of the

material used.[4] At present, record efficiencies of 21.0+% for CdTe-based PV devices still fall well short of the predicted maximum of ~30% efficiency. There are two main reasons for this. The first is that achieving high doping concentrations in CdTe has been a challenge due to the typical self-compensating behaviors of II-VI semiconductors. Secondly, formation of a good ohmic contact with CdTe has been difficult due its relatively high electron affinity of about 4.5 eV making it more difficult to extract photogenerated carriers without a voltage loss.[5] This high electron affinity greatly limits the choice of back contact metal that can be used for p-type material.[6] Typically, a Schottky contact is formed with most metals for p-type CdTe, introducing a potential barrier that charge carriers must overcome in order for charge to flow.[7,8]

Before proceeding further, it is worthwhile to define a few key parameters associated with solar cell performance. There are three main factors that affect solar cell efficiency: black body radiation, radiative recombination, and spectral loss. The efficiency of a solar cell, η, in principle be described by the following, which assumes the sun acts as a black body source

$$\eta = \frac{qV(\phi_s - \phi_r)}{\sigma T_{sun}^4} \quad (1)$$

where q is the electric charge, V is the voltage across the device, ϕ_s is the incident photon flux entering the device, ϕ_r is the radiating photon flux leaving the device, σ is the Stefan-Boltzmann constant, and T_{sun} is the temperature of the sun.[9] While this expression can be derived from a fundamental physics perspective, it is not entirely useful for research applications. Instead, the following expression is more commonly used when testing solar cell devices

$$\eta = \frac{V_{oc} J_{sc} FF}{P_{in}} \tag{2}$$

where the parameters used are based on easily identifiable metrics when performing efficiency tests. Figure 1 shows a typical current density-voltage (JV) curve taken to determine the efficiency of the device, highlighting the parameters of importance in Eq 2. Here V_{oc} is the open circuit voltage of the device, and J_{sc} is the short circuit current density. FF is the fill factor, which is related to the maximum power point voltage (V_{mp}) and current (J_{mp}) of the device, and V_{oc} and J_{sc} through the following

$$FF = \frac{J_{mp} V_{mp}}{J_{sc} V_{oc}}. \tag{3}$$

P_{in} is the input power of the light used to test the device. Typically, P_{in} represents some variation of a standard solar spectrum although it could also represent monochromatic light. Throughout the entirety of this study, the parameters presented in Eq. 2 will be used to assess the effectiveness of our research as it pertains to solar cell applications.

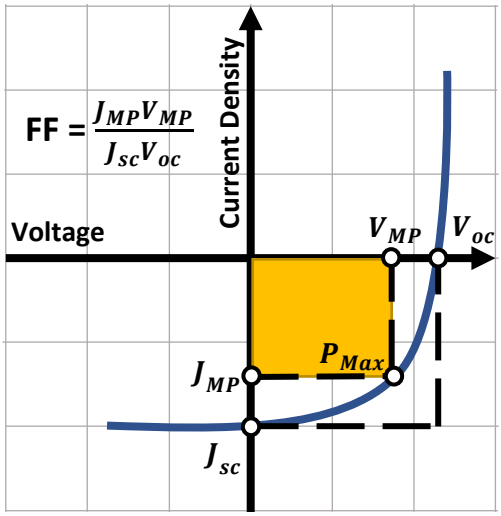

Figure 1. A typical JV response curve for solar cells. *Figures of merit including J_{sc} and V_{oc} are highlighted, as well as the determination of the Fill Factor (FF).*

1.1 Heterojunction fundamentals and band gap engineering [a]

In order optimize CdTe solar cell functionality, we must begin with a basic understanding of heterojunction fundamentals and band gap engineering. Let's start with the basic energy band diagram of a uniformly doped, compositionally uniform semiconductor as shown in Figure 2. Here, E_{vac} represents the energy of a free electron that exists outside of the surface of the semiconductor, and acts as a reference point for all other energies. E_c and E_v are the energy levels of the bottom of the conduction band and top of the valence band, respectively. The positions of these energy levels can be calculated by solving the Schrödinger equation, or measured, using E_{vac} as a reference

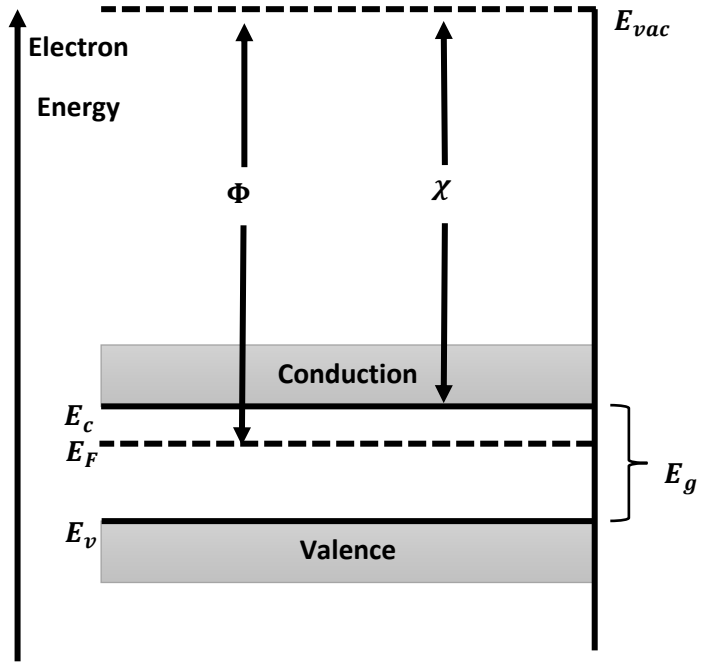

Figure 2. The basic band diagram of an isolated, uniformly doped semiconductor, illustrating the figures of merit relevant to junction formation

[a] This section closely follows the formalism that can be found in textbooks such as [71] and [72]

point. The Fermi energy, E_F, represents the average energy of an electron in the highest energy level of a material. In a metal, at 0 K, this would correspond to the highest filled energy state. In a semiconductor, E_F is typically located in the band gap as it represents a statistical average energy of the highest electron energy in thermal equilibrium. The electron affinity χ, represents the minimum needed energy for an electron to escape a semiconductor and become free, while the work function, Φ is the average energy needed to take an electron from the material to the vacuum level. From this, we can make some basic mathematical definitions.

$$E_c = E_{vac} - \chi \tag{4}$$

$$E_v = E_c - E_g = E_{vac} - \chi - E_g \tag{5}$$

where E_g is the band gap energy of the semiconductor.

Now that we have the basics of the band structure of an isolated semiconductor, let us consider a junction made with the same semiconductor material on both sides of the junction but with different impurity concentrations. As described in detail in any semiconductor physics textbook, some impurities produce excess electrons which reside in the conduction band and produce an electron-like, or n-type conductivity. Other impurities capture electrons in the valence band producing an absence of electrons to fill the band, or holes, which act as positive charge flow to give so-called hole-like, or p-type conductivity.

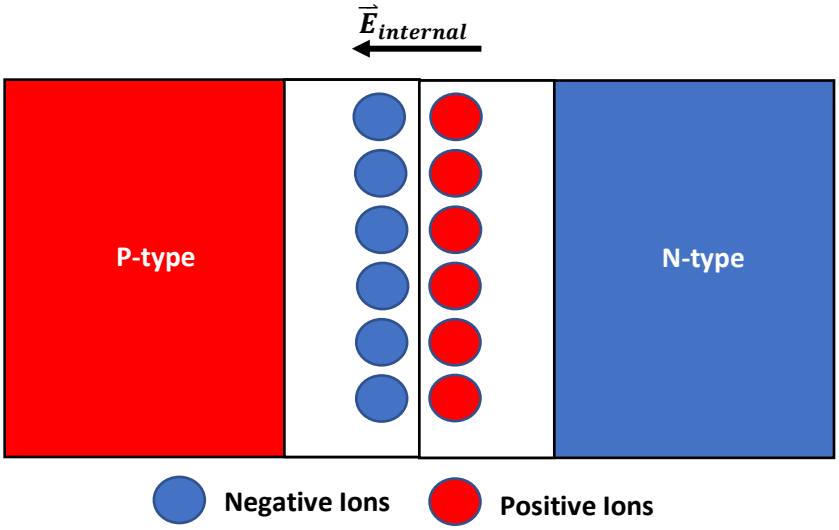

Figure 3. Depiction of the depletion region formed upon contact of an n-type and p-type semiconductor

In this scenario, we have a uniformly p-type semiconductor and a uniformly n-type semiconductor that form the junction. Upon contact, the majority carriers on both sides of the junction will migrate to the other side, leaving behind atomic ions on both sides of the junction (see Figure 3 above), forming the depletion or quasi-neutral region in the immediate vicinity of the junction. These atomic ions then induce an internal electric field that limits further charge flow in thermal equilibrium. We know that a charge in the presence of an electric field will produce a force

$$F_e = -qE(x) \tag{6}$$

for electrons and

$$F_h = qE(x) \tag{7}$$

for holes. An electron will experience a change in energy, ΔE as it moves through the E-field by

$$\Delta E = -\int F_e dx = -qV(x) \tag{8}$$

This means that the conduction and valence bands must shift with position, x, as they represent the energy levels of the electrons or holes with respect to the vacuum, and Eqs. (1) and (2) become

$$E_c(x) = E_{vac} - \chi - qV(x) \tag{9}$$

and

$$E_v = E_{vac} - \chi - E_g - qV(x) \tag{10}$$

Figure 4 below depicts this scenario. Before the two semiconductors are joined together, their Fermi levels are separated by

$$E_{F_n} - E_{F_p} = E_g - \delta_n - \delta_p \tag{11}$$

where

$$\delta_n = \left(E_c - E_{F_n}\right) = kT \log(N_C/n_0) \tag{12}$$

and

$$\delta_p = \left(E_{F_p} - E_v\right) = kT \log(N_V/p_0)\,. \tag{13}$$

In Eqs. (12) and (13), N_C is the density of states at the conduction band minimum, while N_V is the density of states at the valence band maximum.

Once the two semiconductors come into contact, the energy bands must adjust so that the Fermi levels on either side of the junction are equal to represent thermal equilibrium. This represents the driving force behind the initial migration of majority carriers discussed previously, which in turn causes the formation of atomic ions at the interface. These atomic ions form the basis of the contact, or built-in potential, V_{bi}, which is determined by the separation in the Fermi levels of the isolated semiconductors

$$qV_{bi} = E_{F_n} - E_{F_p} = kT \log\left(\frac{N_A N_D}{n_i^2}\right) \tag{14}$$

It is critical to note here that the last expression is only true for homojunctions, i.e. the same semiconductor material is used on both sides, but with different doping levels. However, the built-in potential is always given by the difference in Fermi levels of the isolated semiconductors. If we reference the Fermi levels directly to the vacuum level, then we obtain a general expression for the built-in potential

$$qV_{bi} = \Phi_{\mathrm{p}} - \Phi_n \tag{15}$$

where

$$\Phi_p = \chi_p + E_{g_p} - \delta_p \tag{16}$$

and

$$\Phi_n = \chi_n + \delta_n \tag{17}$$

are the work functions of the p and n type semiconductors. Combining (13) and (14) with (12), we can also come up with an expression for the built-in potential in terms of the electron affinity

$$qV_{bi} = (\chi_p - \chi_n) + E_{g_p} - \delta_p - \delta_n \tag{18}$$

The above mathematical formalism provides us with a first order approximation of the band alignment for junctions at equilibrium. Figure 4 summarizes this formalism for a homojunction. At this point, it is worthwhile to note that for a "perfect" solar cell that experiences no recombination, the V_{oc} of the device would be exactly equal to the V_{bi} associated with the junction occurring when the diffusion currents from each side are balance. However, recombination currents, which occur when an electron and a hole

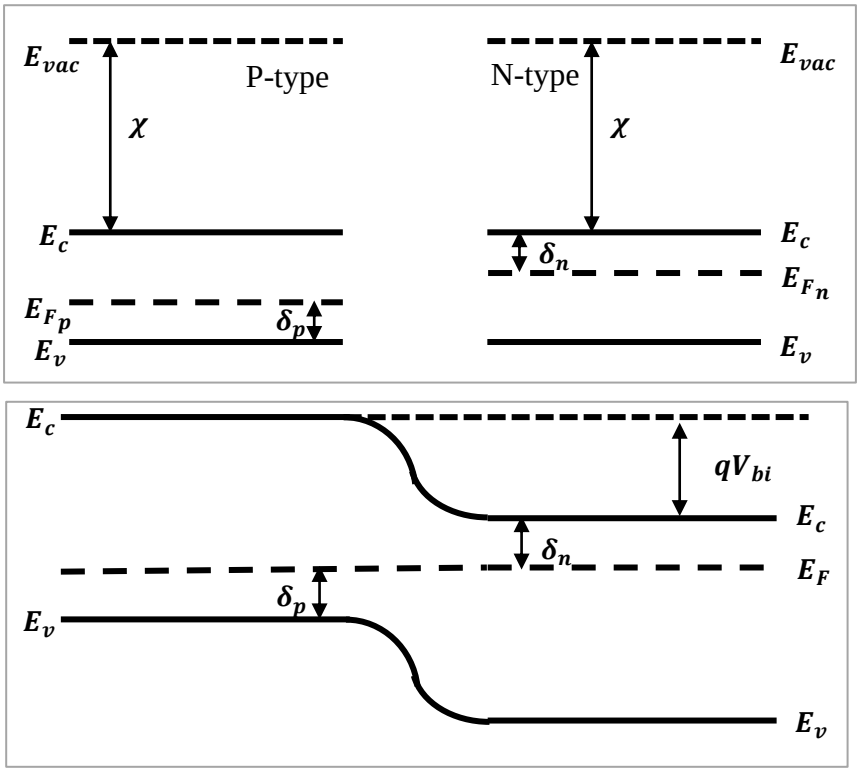

Figure 4. Band alignment diagrams for (Top) two isolated semiconductors of the same material but doped oppositely and (Bottom) when the semiconductors are brought into contact.

meet and annihilate each other outside the junction, will always exist in a real material and thus the V_{oc} of the solar cell will always be less than the V_{bi}.

To draw energy band diagrams for heterojunctions, we must know how the bands line up at the junction in addition to how the band gap varies with position. Consider an $Al_{0.3}Ga_{0.7}As/GaAs$ heterojunction as shown in Figure 5.

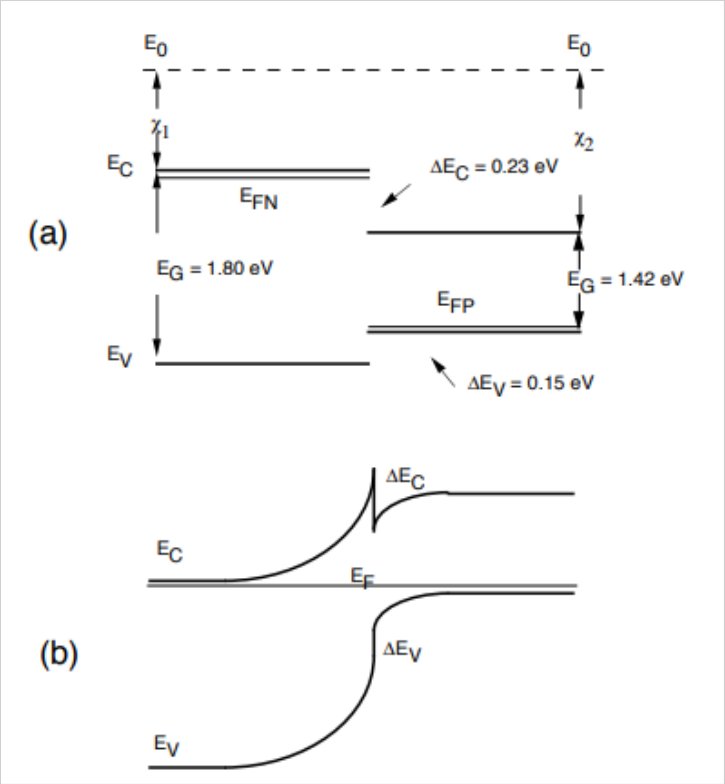

Figure 5. $Al_{0.3}Ga_{0.7}As/GaAs$: n-p heterojunction band alignment (a) before contact and (b) after.

From Figure 5 we see that the change in the conduction band ΔE_c is given by

$$\Delta E_c = \chi_2 - \chi_1. \tag{19}$$

This change in the conduction band energy is also known as the conduction band offset (CBO). We also see that the change in valence band energy, ΔE_v, or the valence band offset (VBO) is given by

$$\Delta E_v = \Delta E_g - \Delta E_c \tag{20}$$

where ΔE_g is the difference in band gap between the two materials. Equations (19) and (20) are known as the Electron Affinity Rule and play a role in how we draw band alignment diagrams. For a general heterojunction, the following rules describe how we draw them

(1) First, draw the band diagrams for each isolated material, referenced to the vacuum level.

(2) Determine the CBO and the VBO from the difference in electron affinity and the respective band gap for the two materials

(3) Align the Fermi levels of the two materials and draw the conduction band and valence band positions for the bulk materials.

(4) Insert the CBO and VBO

(5) Finally, draw the band bending in the conduction and valence bands so that they connect the CBO and VBO on either side of the junction.

The difference in band alignment differing doping types in the $Al_{0.3}Ga_{0.7}As$/GaAs heterojunction example are shown in Figure 6 and Figure 7 to illustrate the application of these rules.

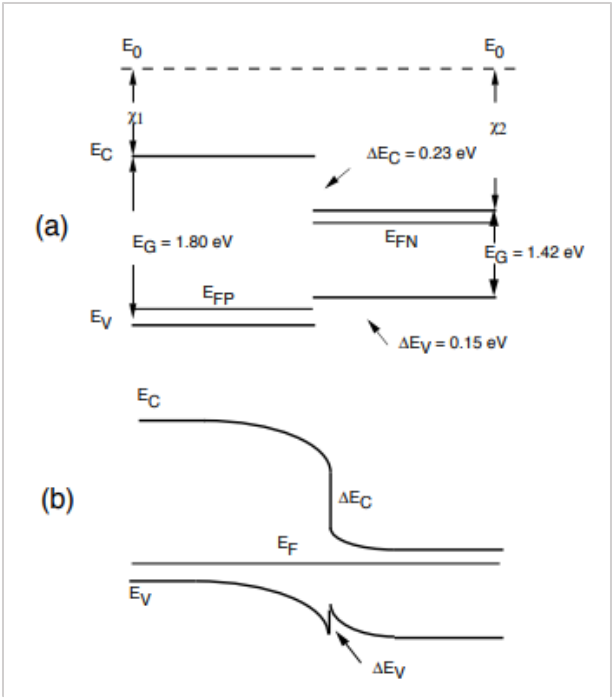

Figure 6. $Al_{0.3}Ga_{0.7}As/GaAs$: p-n heterojunction band alignment (a) before contact and (b) after.

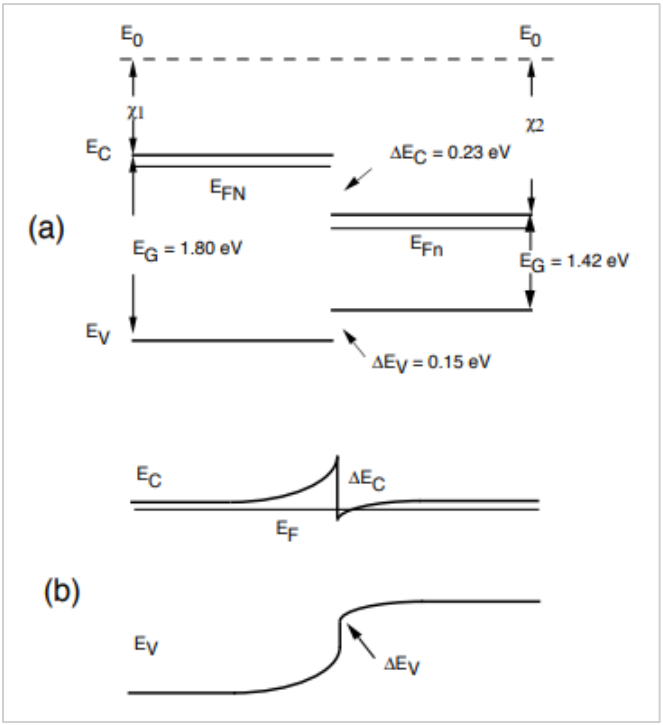

Figure 7. $Al_{0.3}Ga_{0.7}As/GaAs$: n-n heterojunction band alignment (a) before contact and (b) after.

At this point, it is worth emphasizing that the electron affinity rule at best only provides a first order approximation of the band alignment. In practice, the electron affinity rule has proven to be an unreliable way to deduce band offsets. This is because electron affinities, and work functions of materials are also highly sensitive to the state of the surface of the material, and their accurate prediction is non-trivial as an interfacial dipole layer typically forms to accommodate the chemical and energy mismatch. Often there is also chemical interdiffusion. See, for example, the work presented by Kahn that discusses these issues.[10]

As an example of this, consider a thin film of polycrystalline gold (Au); when exposed to ambient atmosphere, it exhibits a Φ of 4.4-4.7 eV; when atomically cleaned and ordered in ultra-high vacuum (UHV) conditions, it exhibits a Φ of 5.0-5.1 eV; and when sputter cleaned the Φ is 5.3-5.4 eV.[10] In addition, to the non-trivial nature of accurate χ's and Φ's for isolated materials, when two semiconductors are brought into contact, there is a charge transfer between the bond at the interface which sets up a dipole as mentioned above. There is no reason to believe that the dipole formed at the semiconductor-semiconductor interface will be the same as the dipole that forms at the semiconductor-vacuum interface. For these reasons, experimental approaches to determine the band offsets of heterojunctions have been undertaken with one of the most reliable being to measure them directly using x-ray photoemission spectroscopy (this method will be discussed in greater detail later).

While the electron affinity rule does not provide accurate determinations of band offsets, it does provide guidance in the search for appropriate back contact materials for CdTe solar cells. A typical CdTe solar cell is based on a cadmium sulfide (CdS)/CdTe, n-

p junction. Thus, holes are the majority carrier in the p-type CdTe layer that must be collected at the back-contact. To optimize this, the band alignment between the CdTe and the back material should be either valence neutral (no VBO), or have the valence band of the back material be at a higher level than that in the CdTe (this equates to hole injection). To optimize even further, it would be ideal if the band alignment included some sort of electron barrier in the conduction band, whether that be in the CdTe layer or in the back contact layer, which electrostatically "reflects" the minority electrons from the interface to decrease minority carrier recombination at the back interface – a significant source of carrier loss.

Gold was the original choice for a direct back contact material in laboratory settings, however, the expense and the rectifying contact behavior it exhibited (Schottky barrier formation), it was modified to include a zinc telluride (ZnTe) back contact buffer layer between the CdTe and metal. ZnTe was thought to be valence band neutral, meaning there was no VBO between ZnTe and CdTe, which is critical for the current device structure. The lack of VBO in conjunction with a substantial CBO, suggested that ZnTe would be ideal for producing an ohmic contact with p-type CdTe and serve as an electron reflector. ZnTe also has a lower work function than CdTe, and so is easier to contact with metals without the formation of a Schottky barrier.[11]

However, issues with resistive loss and interface recombination continued. More recently, the VBO between ZnTe and CdTe has been re-calculated, suggesting a substantial predicted hole barrier of ~320meV.[12] While low VBO is observed in x-ray photoemission spectroscopy measurements, some type of barrier appears to be consistent with issues remaining with this contact material. That is, while ZnTe has been

demonstrated to be the most effective back-contact buffer layer to date, it is still not optimal and leaves room for improvement as CdTe technology attempts to push the limits of performance. Thus, new approaches to back contact materials are needed.

1.2 Statement of the Problem

One of the primary issues remaining with optimizing CdTe-based solar cell technology is the formation of ohmic contacting at the back interface. During the work performed for this dissertation, I have investigated the efficacy of thallium doped lead telluride as well as thallium doped tin telluride as back contact buffer layers in CdTe-based devices. Through this work, the following questions were addressed:

1. What is the valence band offset between CdTe and lead telluride, and separately, between CdTe and tin telluride? Are these band alignments favorable for use in CdTe-based solar cells?
2. How does doping level of lead telluride films effect the band bending at the junction with CdTe? How does this in turn effect minority carrier lifetimes in CdTe devices?
3. Do devices with lead telluride or tin telluride back contact buffer layers show improved performance over bare CdTe devices?

Some in industry have abandoned the traditional cadmium sulfide/CdTe junction present in most CdTe based solar cells in favor of a graded cadmium selenium telluride alloy layer. However, these layers are not well understood, particularly regarding the dynamics of the valence and conduction bands. This dissertation also explores the following

questions while seeking to optimize the use of cadmium selenium telluride alloy layers in solar cells:

4. How do the valence and conduction band change as we move through a graded cadmium selenium telluride alloy layer? What is the valence band offset between single crystal CdTe and cadmium selenide? How does the band gap of the cadmium selenium telluride alloy layer change with varying selenium content? By answering each of these, we can provide guidance for future research regarding contacting of these layers.

1.3 Lead Telluride

Lead telluride (PbTe) is a narrow gap semiconductor and has been shown in the past to create ohmic contacts with p-type CdTe.[13] Ohmic contacting implies that no hole barrier exists between the two materials. PbTe's high electron affinity (about 4.2 eV) makes it worthy of consideration for a back-contact material in CdTe based solar cells while the ability to heavily dope p-type ($> 10^{19}/cm^3$) indicates that an ohmic PbTe-metal junction can be obtained. Recall that the work function for semiconductors is defined as the energy required to remove an electron from the Fermi level to the vacuum level, while the electron affinity is defined as the energy to remove an electron from the bottom of the conduction band to the vacuum level. This means that with varying doping levels, the Fermi level can be tuned and thus the "effective" work function can be tuned as well. This means that with appropriate p-type doping, the Fermi level of the PbTe film can be dropped such that it may be possible to match the work functions of the PbTe layer and the CdTe layer, yielding at a minimum, valence neutrality. An intrinsic

CdTe/PbTe interface creates a type-I heterojunction – i.e. the entirety of the PbTe gap exists within the CdTe gap. A previous x-ray photoemission spectroscopy study on CdTe/PbTe(111) heterojunctions found a relatively small valence band offset (VBO) of 0.135 eV between the two materials, allowing for hole injection into the PbTe layer.[14] Let's contrast this with the predicted behavior of the band alignment based on the electron affinity rule employed in SCAPS modeling. SCAPS is a one-dimensional solar cell simulation program developed at the Department of Electrons and Information Systems of the University of Gent, Belgium, often used for solar cell modeling in the photovoltaic research community.[15] SCAPS will be used repeatedly throughout this work to provide a theoretical basis for comparison of experimental results. In Figure 8, the band alignment between the materials using SCAPS modeling was calculated based on reported χ's and carrier concentrations for the CdTe and PbTe layers used in a previous study where PbTe back contact buffer layers were investigated for ultra-thin CdTe solar cells.[16] The exact values used in the SCAPS model are shown in Figure 9.[16] From Figure 8, we see that the VBO predicted based on the difference between the χ's is significantly larger (> 0.7 eV) than the previously measured VBO of 0.135 eV. Not only this, but SCAPS also predicts a hole barrier leading to the interface on the CdTe side, which does not support the previous work showing successful ohmic contact on CdTe using highly p-type PbTe.

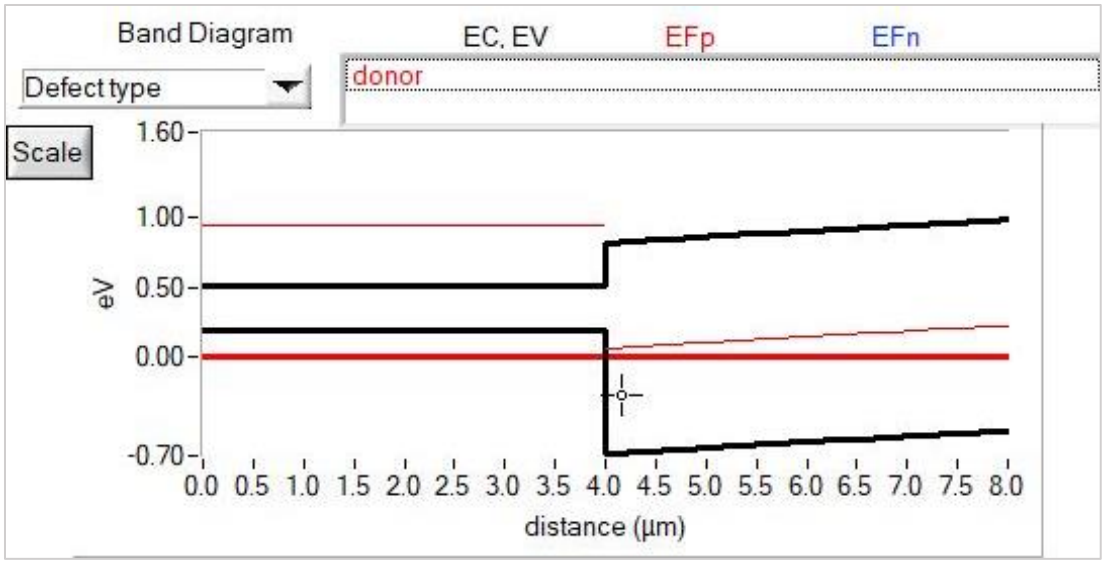

Figure 8. First approximation of the band alignment of a PbTe/CdTe interface using SCAPS modeling based on the electron affinity rule. *The VBO predicted here is substantially larger than previously measured, and shows evidence of a hole barrier in the CdTe VB.*

Table 1 The material parameters used for the numerical analysis of the proposed cells.

Parameters	Back contact		
Φ_b [eV]	Φ_{bp} = 1.25 (Ag), 0.3 (BSF)		
S_e [cm/s]	1×10^2 - 1×10^8		
S_h [cm/s]	1×10^2 - 1×10^8		
R_f [I]	0.9 - 0.95		
Parameters	**CdS:O**	**p-CdTe**	**BSF**
W (µm)	0.05	0.1-10.0	0.1
$\varepsilon/\varepsilon_0$	10.0	9.4	40
μ_c (cm^2/Vs)	100	320	1600
μ_p (cm^2/Vs)	25	40	600
n, p (cm^{-3})	10^{17}	5×10^{15}	8×10^{19}
Eg (eV)	2.8	1.45	0.29
N_c (cm^{-3})	2×10^{18}	8×10^{17}	1×10^{16}
N_v (cm^{-3})	2×10^{19}	1.8×10^{19}	2×10^{17}
χ (eV)	4.50	4.28	4.6

Figure 9. Exact values for material parameters used for the SCAPS calculation used in Figure 8.

It has been suggested that if the PbTe layer is highly p-typed doped, it can create a back surface field (BSF) at the interface between the two materials.[16] This highly p-type

layer should cause upward band bending in the CB of the CdTe layer thus reflecting electrons away from the interface, decreasing carrier recombination at the interface and increasing overall device performance. Thallium (Tl) has been a successful p-type dopant in PbTe for many years, substituting for Pb in the PbTe lattice.[17] For these reasons, I will investigate the use of a PbTe back contact buffer layer with varying concentrations of Tl doping as a possible replacement for ZnTe as a back contact.

1.4 Tin Telluride

Tin telluride (SnTe), is another narrow gap semiconductor also with a relatively high electron affinity (about 4.2 eV). While the VBO between CdTe and SnTe is not available in the literature, the measured VBO between SnTe and PbTe suggest that SnTe may act directly as an electron reflector for CdTe, while also promoting hole injection (see Figure 10).[18] The measured VBO for PbTe/CdTe was used to estimate the band line up, with PbTe as the reference for both materials. To ensure that carrier recombination at the SnTe/CdTe interface is kept to a minimum, the SnTe layer will be kept highly p-type to achieve a BSF, in a similar manner as the PbTe investigation. Tl should also be a successful p-type dopant for SnTe, substituting for Sn in the lattice structure, although it has been reported to be difficult to obtain low p-type SnTe by molecular beam epitaxy (MBE). That is, a native defect often produces hole concentrations greater than $10^{20}/cm^3$ under MBE growth conditions. For these reasons, I will also investigate the use of a SnTe back contact buffer layer doped with Tl as a possible replacement for ZnTe as a back-contact material.

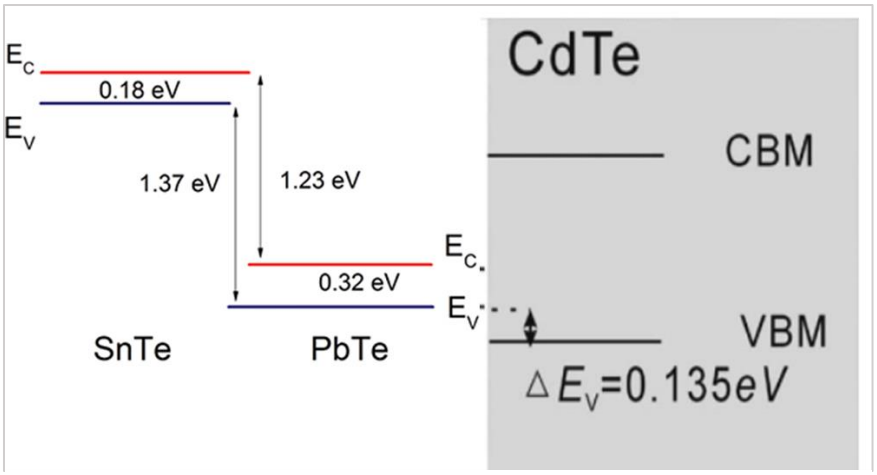

Figure 10. VBO between SnTe/PbTe, depicted in conjunction with the VBO between PbTe/CdTe.

1.5. Cadmium Selenium Telluride Alloys

Recently, some in industry have moved away from strictly CdTe solar cell production using the traditional CdS/CdTe (n-p) junction in favor of using a cadmium selenium telluride (CdSeTe) alloy layer with a gradient in Se content in the absorber layer. The addition of Se lowers the band gap of the absorber layer, leading to increased solar collection.[19] While these devices have shown improved performance and have set new record efficiencies, they are not well understood, particularly in regards to the dynamics of the valence band and the band gap as the Se content changes.[20] While studies of optical properties and device performance have been conducted, more research is needed to understand the valence band and conduction band offsets (VBOs and CBOs, respectively) for device optimization, particularly in regards to choosing an optimal back contact material. In fact, the literature reports a wide range of VBOs for CdTe/CdSe, summarized in the Table 1.[21,22,23,24,25,26,27] Legacy materials such as ZnTe also continue to

be used for back contact materials. For these reasons, I will also investigate VBOs between $CdSe_xTe_{1-x}$ alloys with varying Se concentrations and CdTe so that predictions for good back contact materials can be made for various applications. This also allows for a better understanding of the valence and conduction variation with the absorber layer and potential optimization of layer design.

Table 1. CdTe- CdSe VBOs as reported in the literature determined through various means.

Source	CdTe-CdSe Valence Band Offset
Theory (Su-Huai Wei, 1999)	-570 meV
Theory (M. Ribeiro, 2012)	-530-850 meV
Theory (Yong Hua Li (Su-Huai Wei), 2009)	-690 meV
Theory (Yoyo Hinuma, 2014)	-870 meV
Experiment (PL of SL)(Jing-Jing Li, 2012)	-670 meV
Experiment (PESA) (Jasieniak, 2012)	-490 meV
Experiment (PESA) (MacDonald, 2011)	-690 meV

2. EXPERIMENTAL DETAILS

2.1 Molecular Beam Epitaxy

2.1.1 Overview

Molecular Beam Epitaxy (MBE) is an ultra-high vacuum (UHV) deposition technique typically used to manufacture or fabricate semiconductor layers and devices. MBE systems typically have background pressures of 10^{-10} -10^{-12} Torr. Such (ultra) high vacuum levels help to maintain compositional purity and help control epitaxial growth. Epitaxial growth, defined as the ordered growth of a crystal structure on the surface of another crystal, is typically achieved using slow deposition rates, often < 1μm/hr. Such slow growth rates also allow changes in composition to be achieved on an atomic layer basis. This work focuses solely on solid source MBE. With this type of MBE, solid source materials of very high purity, such as cadmium or tellurium, are separately heated in effusion cells until they begin to sublime. The temperature at which materials sublime is entirely dependent on the specific material being used. Once the material sublimes, the gaseous material can then escape the effusion cell and travel within the chamber towards the substrate. Because the system is kept at such a high vacuum level, the mean free path of gaseous material is many orders of magnitude larger than the path between the effusion cell and the substrate, thus creating a "beam" of source material, somewhat shaped by the opening of the effusion cell. After material has travelled from the effusion cell to the substrate, it then condenses on the surface of the substrate, where different atoms and molecules from the source materials may interact with each other. Typical interactions may include adsorption and desorption, as well as crystal formation and growth. The impingement rate, or how much material reaches the substrate per second, is

dependent on the temperature of the source materials. The adsorption and desorption rates are dependent on the substrate temperature. To monitor the crystalline quality of the growths, reflection high energy electron diffraction (RHEED) is typically used to monitor the surface of the substrate to check for ideal conditions. A basic schematic of a typical MBE chamber is shown below in Figure 11.

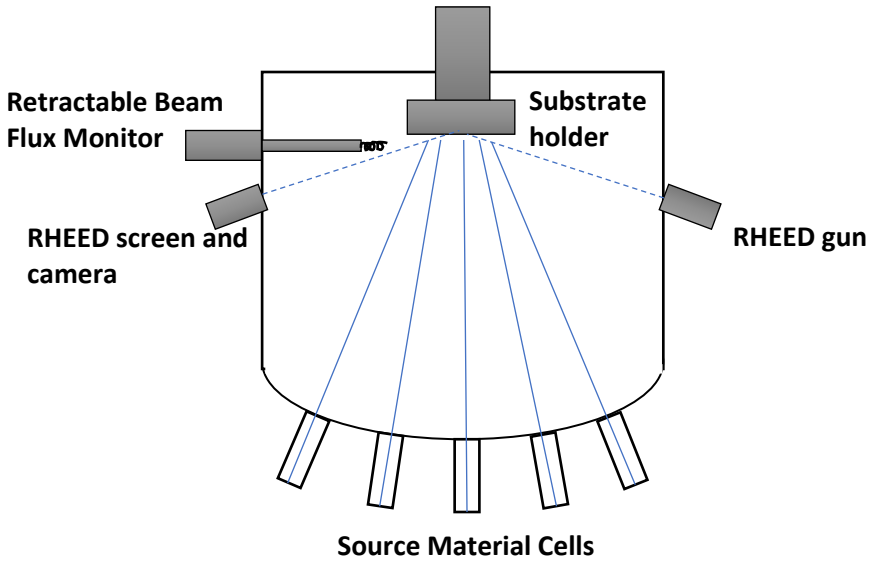

Figure 11. A simplified schematic of an MBE growth chamber.

2.1.2 Equipment

MBE growth of PbTe:Tl, SnTe:Tl, and various compositions of $CdSe_xTe_{1-x}$ alloys was performed at TXST using the 8-chamber MBE system complex, a schematic of which is shown in Figure 12. This system includes a transfer buffer line, maintained at 10^{-9} Torr by a combination of Varian Star Cell and Varian Triode ion pumps, connecting all chambers, with load locks available at both ends. The transfer line is equipped with multiple gate valves for several reasons. The first is to protect as much of

the system as possible in the event of accidental exposure to atmosphere; the second is to aid in pumping efficiency. The load locks are equipped with dry nitrogen gas sources for venting to mitigate water contamination from atmospheric exposure, and turbo pumps to return the load locks to UHV. The load locks are also equipped with heaters to encourage water outgassing and subsequent pumping after each loading, limiting water vapor introduction and contamination throughout the rest of the system. Four specific chambers were used in this work: the Pb-chalcogenide chamber, the Sb chamber, the II-VI chamber, and the atomic hydrogen cleaning chamber.

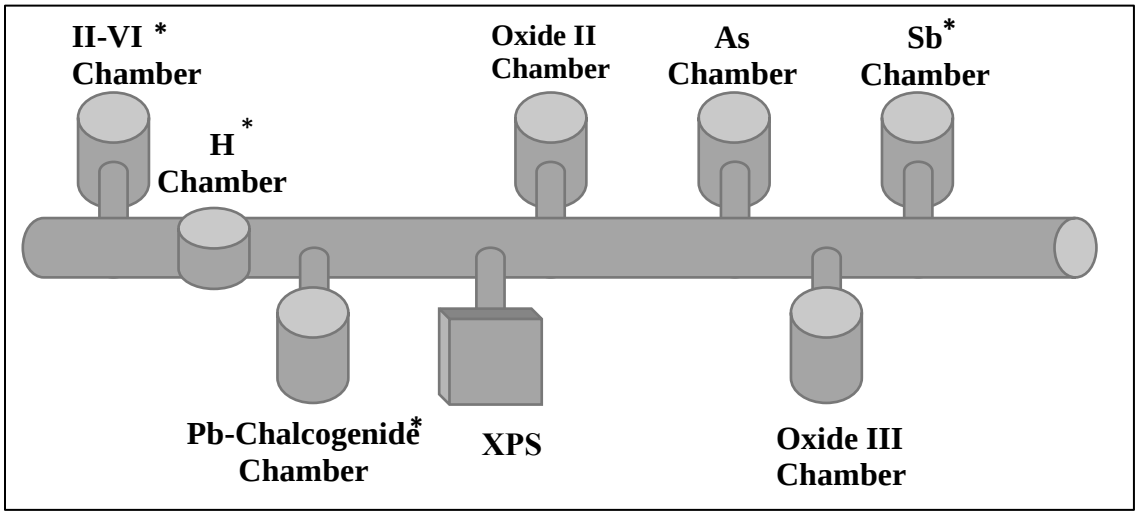

Figure 12. Schematic of the MBE cluster system at Texas State University. *Chambers used in this research are indicated by an asterisk.*

For almost all materials used in this study, standard thermal effusion cells were used. A schematic of a typical effusion cell is shown in Figure 13.[28] Individual cases where this was not true will be explained in further detail in the appropriate section. Effusion cells typically consist of a resistive heater element surrounding a pyrolytic boron nitride crucible containing the source material. A water-cooling shroud around the

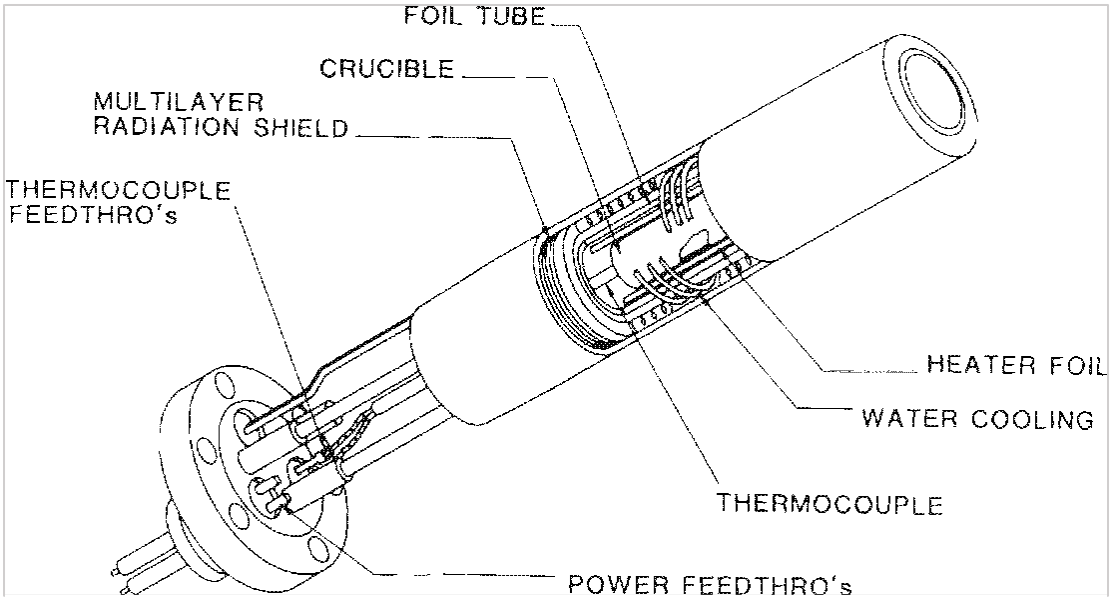

Figure 13. Schematic of a typical effusion cell.

effusion cells is employed to limit the effects of cross-heating between source cells. The temperature of the source cells was monitored using thermocouples and feedback-controlled power supplies manufactured by Eurotherm. Some cells employed dual-zone heaters, one for the bulk of the material and one for the tip of the crucible, to help stabilize and control the flux from the cells with greater precision, as well as prevent clogging of the cell due to deposition of source material around the tip of the crucible. The flux from an idealized effusion cell can be described by the following

$$J = (1.118\ x\ 10^{22}\ cm^{-2})\frac{pA}{l^2\sqrt{MT}} \qquad (21)$$

where J is the flux (number of molecules or atoms striking a unit of area of the substrate per second), T is the temperature of the cell in Kelvin, p is the source pressure in the cell in Torr, M is the molecular mass of the source material, l is the distance between the cell aperture and the substrate in cm, and A is the area of the aperture in cm^2.[29] Typically, M,

l, and A are all fixed, meaning that the flux is essentially controlled by changing the temperature, T, which in turn changes the material's vapor pressure, p. The vapor pressure of a given material is often close to an exponential function of the source temperature, indicating that tight control of T is required for accurate flux control.

2.1.3 Pb-Chalcogenide chamber

The Pb-chalcogenide chamber was used for the growth of PbTe:Tl and SnTe:Tl films. This DCA nstruments chamber is basically a cylinder with a 45° tilt, where the various source cells are located at the bottom of the chamber, pointing towards the target substrate loaded into the chamber manipulator. The manipulator could adjust the position of the substrate relative to the source cells, provide rotation for greater film uniformity, and heat the substrates to the desired temperature for growth. The manipulator temperature, and the substrate temperature, were controlled with the use of appropriate thermocouples and Eurotherm feedback-controlled power supplies. However, since the thermocouple cannot be placed directly on the substrate in this system, the substrate surface temperature needed to be calibrated. This was done by loading a substrate into the chamber with a thin, stretched cone of solid indium (In). The manipulator temperature setpoint was slowly increased, until the cone of In melted, retracting into a tight ball of liquid In on the surface of the substrate due to surface tension. The melting point of In is very well known and so this plus the initial unheated temperature serve as a two-point calibration of substrate temperature. This has proven efficacious based on numerous calibration studies in the various systems in the past. Both PbTe:Tl and SnTe:Tl films were grown at a (real) substrate temperature of 250 °C.

UHV was maintained in the deposition chamber with use of an Oxford Instruments CTI-Cryogenics Cryo-Torr cryopump, an ion pump, and the periodic use of a titanium sublimation pump (TSP) cycled every 8 hrs. While this chamber is equipped with a liquid nitrogen shroud, it was not used during this investigation, as base pressures for this system were routinely below mid-10^{-10} Torr, while growth pressures rarely exceeded mid-10^{-8} Torr. A phosphor screen and an electron gun for RHEED are also equipped on this chamber, however because most of the substrates used in this chamber were polycrystalline in nature, crystalline quality was not monitored during these growths.

Standard effusion cells were used for PbTe, SnTe, Te, and Tl_2Te source materials, manufactured by EPI Scientific, Applied Epi, and Veeco. Cells were set to growth temperatures and allowed to stabilize for two hours before growth. A beam flux monitor (BFM) consisting of an exposed ion gauge was used to measure the relative fluxes of the different source materials used. The BFM can be extended into the beam path where the substrate would be positioned during growth and retracted before growth starts. Before each growth, the beam equivalent pressure (BEP) for each source was monitored and recorded for the set temperature by determining the difference between the BFM background reading and the pressure reading when exposed to the source material. This is not an absolute measurement of flux but provides a relative estimate to allow for reproducible conditions. These BEPs were periodically calibrated against the growth rate. A BEP ratio of about 10:1 was used for PbTe and Te, as well as SnTe and Te for PbTe and SnTe growths, respectively. Because the Tl_2Te source was used as a dopant source only, the BEP of Tl_2Te was too low in all cases to accurately measure, and Tl

incorporation was monitored through other characterizations and was primarily controlled by adjusting the oven temperature.

2.1.4 Sb chamber

The Sb chamber was used for substrate surface preparation for lower Se concentration $CdSe_xTe_{1-x}$ alloy growths. Specifically, InSb(100) wafers were mounted onto molybdenum blocks with In and loaded into the chamber for native oxide removal and for growth of an InSb buffer layer on the substrate to improve surface crystallinity. The Sb chamber is the same DCA Instruments chamber model as the Pb-chalcogenide chamber with the same geometry and general operation as described in the previous section. Due to the wafer mounting method used, i.e. 2" wafers were quartered, then mounted using In, variation in thermal mass from sample to sample was unavoidable. There was only a small temperature window between oxide desorption and actual melting of the InSb substrate, thus exact control over the substrate temperature was crucial. Because of this, an In-melting point calibration had to be performed with every growth. A few cones of In were placed around the substrate on the molybdenum block, which was slowly heated, and the melting point of the In was recorded. This allowed a controlled achievement of the desorption temperature of about 500 °C while staying below the melting temperature of 527 °C.[30]

UHV was maintained in this growth chamber with use of a CTI-Cryogenics ON-BOARD cryopump and a Gamma Vacuum TiTan ion pump. This chamber is also equipped with a liquid nitrogen shroud that was filled prior to growth to help control the chamber pressure. Normal idle conditions would leave the chamber with a mid 10^{-9} Torr base pressure, while the use of the liquid nitrogen would bring the base pressure down to

the 10^{-10} Torr range and keep the growth pressure in the 10^{-8} Torr range. The use of liquid nitrogen in this chamber was of crucial importance due to previous use of arsenic (As) sources. As has a relatively high room temperature vapor pressure, meaning that even without intentional heating, appreciable amounts of As are present in the chamber. The liquid nitrogen combats this by cooling the chamber and encouraging condensation of As that may have outgassed due to the heat provided by the substrate heater or the source cells. A phosphor screen and an electron gun are also equipped on this chamber, to allow for RHEED monitoring of crystalline quality, which was of utmost importance in these growths. A k-Space Associates, Inc. kSA 400 camera was equipped to monitor the RHEED response.

Effusion cells manufactured by MDC MFG Inc and Veeco were used for In and Sb source materials, respectively. Once again, cells were set to the required temperatures and allowed to stabilize for two hours before growth. A BFM was used to monitor the In and Sb BEP's for InSb growths. After the In melting point was determined for each growth, the manipulator temperature was elevated another 175 °C under and an Sb flux of $2x10^{-7}$ Torr was introduced. From there, the manipulator temperature was slowly increased until the start of a RHEED pattern became visible. At this point the manipulator temperature was held constant and the Sb flux was increased to $5x10^{-7}$ Torr for five minutes to ensure successful removal of the native oxide. Next, the temperature was dropped to a real temperature of 345 °C and the Sb shutter was closed, until the target growth temperature was achieved. Finally, both In and Sb fluxes were introduced and allowed to grow for one hour, producing a thin InSb buffer layer on the substrate. A BEP ratio of 1:4 was used for In and Sb during growth.

Once this surface buffer layer growth was complete, the sample was transferred along the UHV buffer line to the II-VI chamber for subsequent $CdSe_xTe_{1-x}$ alloy layer growth.

2.1.5 II-VI chamber

The II-VI chamber was used for growth of uniform $CdSe_xTe_{1-x}$ alloy layers of selected Se compositions. This chamber is a custom built DCA Instruments chamber with a vertical orientation, i.e. the manipulator is at the top of the chamber while the source flange is at the bottom rather than the more typical tilted chambers. Manipulator temperature and control in this chamber is the same as others discussed.

UHV was maintained in the deposition chamber with use of a CTI-Cryogenics Cryo Torr 8 cryopump and Gamma Vacuum TiTan ion pump. This chamber is also equipped with a liquid nitrogen shroud that was filled prior to growth to help drop the chamber pressure. Similar to the Sb chamber, normal idle conditions would leave the chamber with a mid 10^{-9} Torr base pressure, while the use of the liquid nitrogen would bring the base pressure down to the 10^{-10} Torr range and keep the growth pressure in the 10^{-8} Torr range. Once again, an As source had been previously used in this chamber, and liquid nitrogen was used to minimize As contamination. A phosphor screen and an electron gun are also equipped on this chamber, to allow for RHEED monitoring of crystalline quality, guiding the overall dynamics of the growth. A k-Space Associates, Inc. kSA 400 camera was equipped to monitor the RHEED response.

Dual-zone effusion cells were used for Cd and CdTe source materials, while a single zone effusion cell was used for the Se source and a corrosive series valved cracker cell was used for the Te source. All source cells in this chamber were manufactured by

Veeco. A cracker cell has two furnace zones, one at the bulk, and a much higher temperature zone closer to the aperture of the cell. The flux from the bulk is directed into this higher temperature zone where, typically, the multi-atomic species is broken apart into a simpler species which can more easily be incorporated into the growth structure. This is often used to reduce As_4, P_4 and Se_n (n=4, 6, 7, 8, etc.) into diatomic species for better growth. This is not the case for Te however. Te will naturally form Te_2 upon subliming, which is incredibly difficult to crack. Here, the use of the cracker cell provided two important advantages. First, the dual heating zones greatly reduced clogging that occurs with Te by having a hot zone. Secondly, the Te cracker cell was also equipped with a needle valve, which acts as a way to change the aperture area, A, in Equation (21) above. Needle valves like this can provide a convenient way to fine tune the material flux without changing thermal loads allowing rapid tailoring of alloy levels.

Unlike the previous growths mentioned, a more detailed consideration of the growth dynamics must be given for the $CdSe_xTe_{1-x}$ alloy growths. The lattice parameters of all materials involved must be considered, especially given the fact that the binary endpoint CdSe does not naturally form a zinc blende structure, preferring a hexagonal structure, but can be forced into the zinc blende structure by the underlying material. Minimizing lattice mismatch between the alloy and the substrate is therefore of utmost importance to ensure the desired lattice structure in the $CdSe_xTe_{1-x}$ alloy layer. If we know the CdTe lattice parameter (6.482 Å)[31], the CdSe zinc blende lattice parameter (6.077 Å)[32], and assume Vegard's law, then we can predict the lattice parameter of the $CdSe_xTe_{1-x}$ alloy to change linearly with changes in Se composition as shown in Figure 14. With this in mind, we chose two substrates to conduct $CdSe_xTe_{1-x}$ alloy growths on:

InSb(100) and GaSb(100) with lattice parameters of 6.479 Å and 6.0959 Å respectively.[31,33] The lattice mismatch for the $CdSe_xTe_{1-x}$ alloys and the two chosen substrates are also shown in Figure 14. From this, we see that significant lattice mismatch will occur in the mid-region, for Se composition $0.4 < x < 0.85$, making epitaxial growth more difficult for this composition.

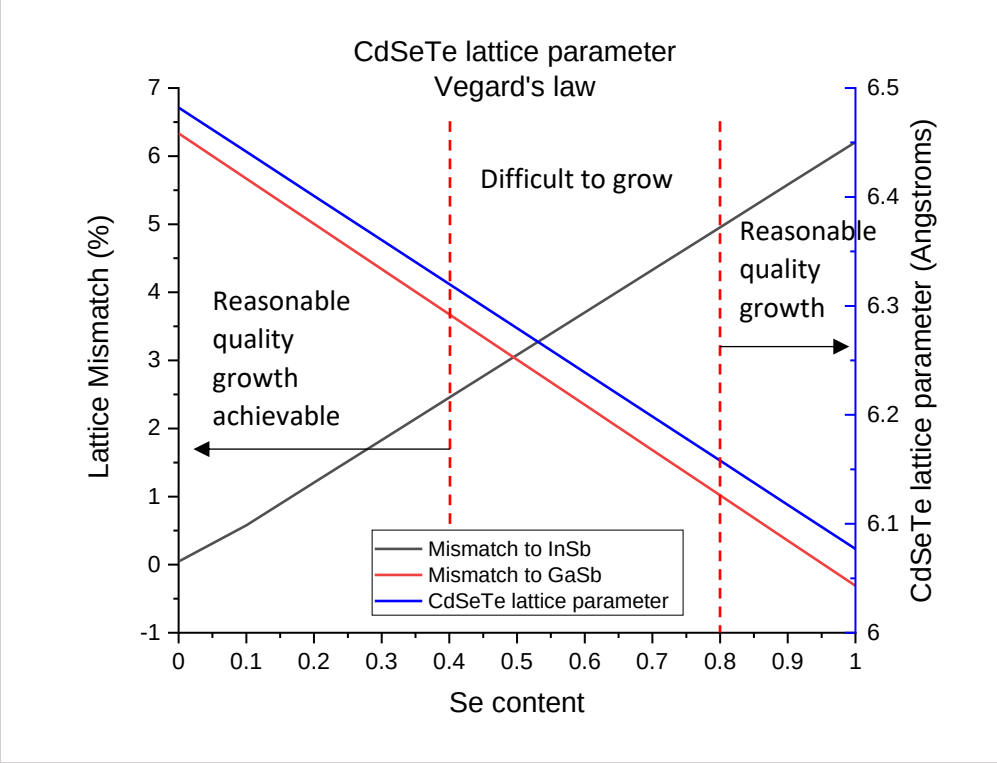

Figure 14. The changes in lattice parameter for $CdSe_xTe_{1-x}$ alloys as the Se content changes is presented along with the percent lattice mismatch with InSb and GaSb.

In II-VI growth in general, the high vapor pressure of the constituent materials at the substrate growth temperature ensures that excess material on the surface of the substrate re-evaporates or desorbs from the surface, leaving a stoichiometric material behind. Of the materials used in these growths, Te has the lowest vapor pressure, but if

the growth substrate temperatures are kept above 180 °C there is no Te precipitation. Thus, above 180 °C CdTe can be grown with excess Cd or Te and remain stoichiometric. The same is true for Cd and Se with CdSe growth, as well as Zn and Te for ZnTe growth. However, once we begin to investigate alloys, relative bonding strength considerations become critical for successful growth. For an intended $Cd_{1-x}Zn_xTe$ growth, we must consider that Te will always bond with Zn before it will bond with Cd. The same is true of Se if we were considering a $Cd_{1-x}Zn_xSe$ growth, i.e. Se will always bond with Zn before it bonds with Cd. Thus, if you provide a stoichiometric flux of Cd and Te_2 by subliming CdTe, you can grow $Cd_{1-x}Zn_xTe$ by providing Zn flux, all of which will be captured by bonding to the Te. This is true even when you provide an excess of Cd flux.

A similar situation occurs when Se and Te are competing for bonding sites. For low x-value $CdSe_xTe_{1-x}$ growths, a small amount of Se flux was provided to a stoichiometric flux of CdTe, all of which was either captured by any excess Cd and/or displaced Te, to grow CdSeTe. Early growths of intended high x-value $CdSe_xTe_{1-x}$ were inadvertently grown with excess Se such that when a Te flux was provided, there was no appreciable Te incorporation due to the excess Se capturing all of the Cd, while the Te desorbed. This was initially indicated with PL spectroscopy (discussed in detail in section 2.7) and subsequently verified by EDS (discussed in detail in section 2.5). The growth conditions for these samples as well as the band gap as determined by PL spectroscopy are shown in Table 2, highlighting that despite differing growth conditions, CdSe was the result in all cases.

Table 2. Growth conditions for select $CdSe_xTe_{1-x}$ alloy samples along with the band gap found via PL spectroscopy.

Sample Number	Target Se x-value	Cd flux (Torr)	Se flux (Torr)	Te flux (Torr)	PL Band gap (eV)
z-853	1.0	4.3E-7	1.8E-6		1.669
z-860	0.9	3.8E-7	1.7E-6	1.7E-7	1.667
z-863	0.8	4.2E-7	1.7E-6	2.4E-7	1.667
z-864	0.8	4.4E-7	1.6E-7	5.0E-7	1.669

With this evidence indicating that the Te was not incorporating into the CdSeTe growth, determination of the relative Cd and Se flux (BEP) that gave stoichiometric and excess Cd conditions was needed. To do this, the Se flux was lowered so that the growth rate of CdSe was lower (leading to increased crystalline quality) and to discourage appreciable contamination of the chamber and held constant, while the Cd flux was varied. During this time, RHEED patterns were closely monitored in order to identify Se/Cd induced reconstruction on the surface of the substrate, indicative of Cd- or Se- rich conditions.[34] The Cd flux was slowly increased while the RHEED patters were monitored. To verify that Cd rich conditions had been achieved, a small layer of CdSe was grown while monitoring the RHEED conditions. Then, the Cd shutter was closed. Once closed, the surface would become Se rich, resulting in the reconstruction observed in the RHEED pattern. If this reconstruction was observed during growth, it would indicate Se-rich growth. Once the Cd was opened again, the Se reconstruction pattern disappeared as now the surface was in Cd excess, indicating that Cd-rich conditions had been achieved. To double check this, the Se shutter was closed to verify that there was no

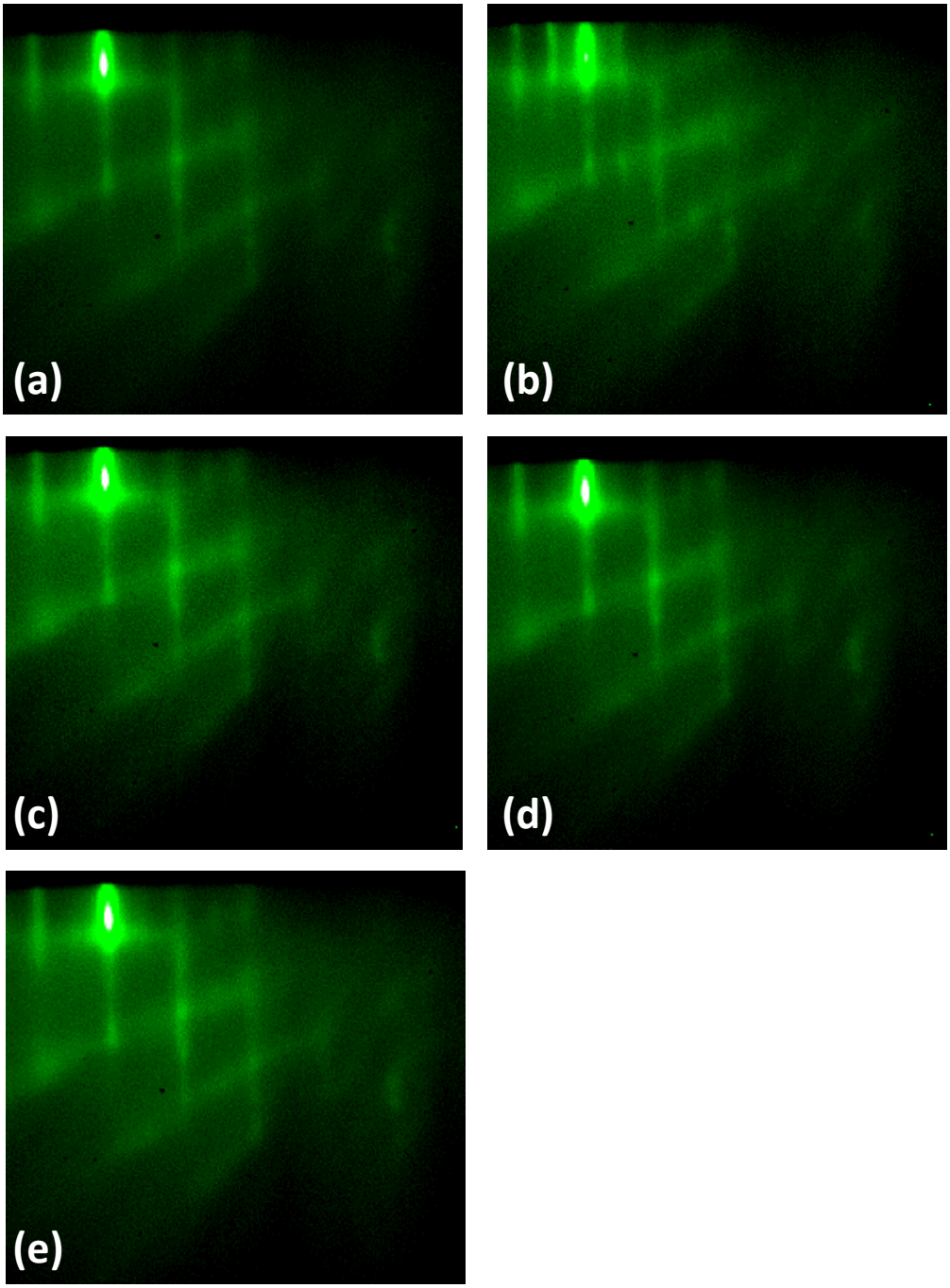

Figure 15. RHEED patterns monitoring the growth dynamics of a $CdSe_xTe_{1-x}$ alloy sample. *The patterns shown are a sequence at (a) the end of the CdSe seed layer, with both Cd and Se sources closed, (b) with the Cd then closed and the Se open – here we see Se reconstruction which indicates Se-rich conditions, but the pattern reverts when (c) the Cd and Se are both open, indicating Cd-rich conditions. (d) shows the pattern for Se now closed and Cd open – indicating a Cd reconstruction and establishing the pattern for Cd-rich growth dynamics, and (e) shows the pattern for both Cd and Se open. These patterns suggest Cd-rich conditions in all instances except for (b) as desired.*

change in the RHEED pattern under a Cd-only flux. The RHEED patterns observed during this process are shown in Figure 15.

With the Cd rich growth conditions determined, we were able to control the Se x-value in high x-value CdSeTe growths. With plenty of excess Cd flux, more than the Se and Te fluxes combined, all Se and Te was captured and the x-value was given by

$$x = \frac{[Se]}{[Se] + [Te]} \tag{22}$$

Rather than supplying individual Cd, Se, and Te fluxes though, it was easier to use already available, known growth rates for CdTe using CdTe and Cd sources, and separately, known growth rates for CdSe using Cd and Se sources. From the perspective of growth rates, one could determine the Se x-value through the following expression

$$x_{Se} = \frac{GR_{CdTe}}{GR_{CdSe} + GR_{CdTe}} \tag{23}$$

Here, GR represents the growth rate of the material in μm/hr. Because the CdSe growth rate was not as extensively calibrated as the CdTe growth rate, it was kept constant. Rearranging the above, one can determine the required GR'_{CdTe} for a desired Se x-value

$$GR'_{CdTe} = \frac{GR_{CdSe}}{x_{Se}} - GR_{CdSe} \tag{24}$$

The standard GR_{CdTe} is directly proportional to the BEP of the CdTe used for the growth. Thus, if the GR'_{CdTe} required for a desired Se x-value is 50% of the GR_{CdTe}, then the standard BEP of the CdTe can be reduced by 50% to achieve the desired GR'_{CdTe}, while maintaining a BEP ratio of about 10:1 for CdTe and Cd.

To reduce strain and misfit dislocation effects in the analysis of $CdSe_xTe_{1-x}$ alloy layers, these layers were grown intentionally thick (~3μm) to encourage relaxation of the film with dislocation reduction. In a well-behaved system, relaxation of the film will yield most dislocations confined near the interface between the film and the substrate. With some compositions of the $CdSe_xTe_{1-x}$ alloy, however, this did not appear to be the case. For these compositions, a superlattice structure was introduced between the substrate and the thick CdSeTe film to encourage dislocations to collect at the interfaces of the superlattice. This superlattice structure consisted of six alternating layers of the desired $CdSe_xTe_{1-x}$ alloy and CdSe films, each approximately 50 nm thick.

2.1.6 Hydrogen cleaning chamber

The GaSb(100) wafers used for higher Se composition $CdSe_xTe_{1-x}$ films were prepared using atomic hydrogen in the hydrogen cleaning chamber. As mentioned previously, this chamber is part of the buffer line of the entire MBE system. While not in use, an ion pump and a turbo pump are used to keep the chamber at UHV. This chamber is equipped with a manipulator and ultra-purity hydrogen source. The hydrogen gas, which occurs naturally as H_2, is passed over a high temperature tungsten filament which catalytically "cracks" the hydrogen molecules into atomic hydrogen. Atomic hydrogen is highly reactive and interacts with any impurities on the surface of the substrate. During the cleaning process, the substrate is heated to at least 400°C, and a hydrogen flux of about $4\ x\ 10^{-6}$ Torr is introduced. The substrate is then left in this environment for 1 hour. On the surface of the GaSb substrate, there exists two oxide species which we wish to remove: Ga_2O_3 and Sb_2O_5. The exposure of the surface to atomic hydrogen yields the following reactions

$$Ga_2O_3 + 4H \rightarrow Ga_2O + 2H_2O$$

$$2Sb_2O_5 + 20H \rightarrow Sb_4 + 10H_2O$$

At temperatures in excess of 400°C, Ga_2O and Sb_4 are volatile and desorb from the surface, along with the water by products, leaving behind a clean GaSb surface for subsequent epitaxial growth.[35]

2.2 X-Ray Photoemission Spectroscopy

X-Ray Photoemission Spectroscopy (XPS) is a non-invasive characterization technique that can be used to determine a variety of things about a material. XPS utilizes high energy x-rays of energy typically greater than 1200 eV to excite electrons deep in the core levels of the atoms in the material under investigation. Ejected photoelectrons are then collected into an analyzer, which determines the electrons' energy, based on its ejection velocity. Basic schematics of both an XPS system and the basic physical principles involved are shown in Figure 16. By measuring the energy of the ejected electrons, material composition can be determined based on known binding energies associated with each element, as determined by the photoelectric effect. For a monochromatic source of x-rays, with energy hf, the ejected electrons will have a kinetic energy KE of

$$KE = hf - BE - \phi \tag{25}$$

where ϕ is the work function of the spectrometer, and BE is the specific binding energy associated with that atom.[36] The ϕ of the spectrometer can be neglected if the system has

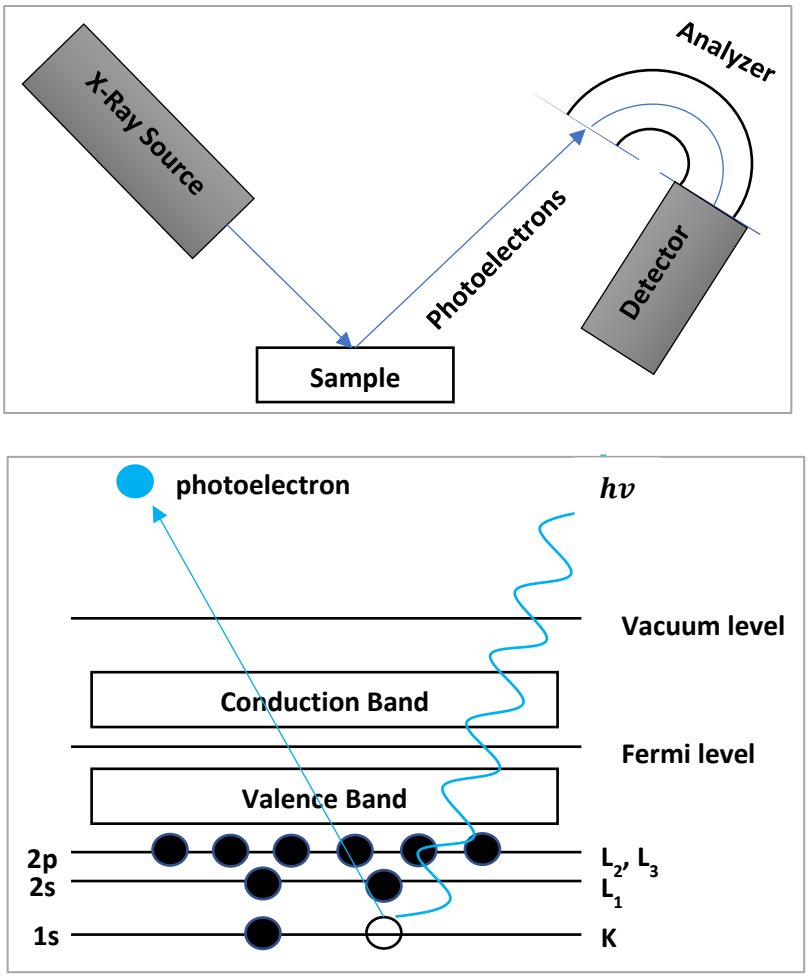

Figure 16. A simplified diagram of an XPS setup (top) and a depiction of the physical phenomenon of photoemission (bottom).

been calibrated by measuring the Fermi level of a metal, which can be used to set the zero point of the BE scale. The BEs are then used to identify specific elements within the material. The spectrum obtained from XPS can also be used to determine material work function, and in semiconductors, can be used to determine the energy of the valence band maximum.

During this investigation, three different XPS systems were used. For the PbTe and SnTe investigation, these measurements were performed in collaboration with Dr.

Craig Perkins, local XPS expert at the National Renewable Energy Laboratory (NREL). These measurements were obtained on a modified Physical Electronics 5600 photoemission system. The photoemission system is equipped with Ar^+ and N^+ ion bombardment, as well as atomic hydrogen for surface cleaning, a SPECS UVS 10/35 He lamp for UPS, standard Al and Mg x-ray sources and a monochromatic Al $K\alpha$ x-ray source.[37] The base pressure for the system is $< 1x10^{-10}$ Torr. The binding energy scale of the instrument was calibrated according to the standard approach outlined by Powell using the Au $4f_{7/2}$ peak and Cu $2p_{3/2}$ peaks of sputter-cleaned gold and copper foils.[38]

For the CdSeTe alloy VBO investigation, a PHI VersaProbe II system available at Malaga University in Spain was used by Dr. Tom Myers and Dr. Dietmar Leinen who performed preliminary investigations. This system is equipped with both ionized Ar and C_{60}^+ etching sources working at 0.5 – 5 kV and 10 – 20kV with angles of incidence -ion beam to sample surface- of 33° and 20°, respectively. The binding energy scale of this instrument was calibrated in the same fashion as the instrument at NREL.

Due to the extenuating circumstances arising from the COVID-19 pandemic, a third XPS system was also used. A select few samples were sent to ThermoFisher for XPS analysis using a NEXA XPS system equipped with an Ar ion etching source working at 200 eV – 4 keV. It is equipped with a microfocused, monochromatic Al $K\alpha$ x-ray source, with an adjustable spot size from 10 – 400 μm. The binding energy scale of this instrument was calibrated in a similar fashion as the instrument at NREL.

2.3 X-Ray Diffraction

X-Ray Diffraction (XRD) is another non-invasive characterization technique that utilizes X-rays to probe materials. Here, monochromatic X-rays are directed towards a sample of interest. A detector placed symmetrically about the sample collects the diffracted rays. The detector and the X-ray source are then rotated around the sample, so that diffraction information can be gathered over a range of incident and diffraction angles. For single crystal materials, x-rays interact with the lattice within the material to produce constructive interference as described by Bragg's law:

$$n\lambda = 2d\ sin\theta \tag{26}$$

where λ is the wavelength of the x-rays, θ is the incident angle, n is the principal number that describes the order of interference, and d is the characteristic spacing between crystal planes.[39] From here, the lattice parameter a_0 can be determined. For a cubic crystal lattice, the interplanar distance d is described by

$$d = \frac{a_0}{\sqrt{h^2 + k^2 + l^2}} \tag{27}$$

where $h, k,$ and l are the Miller indices of the lattice plane considered. Substituting this equation into the previous and rearranging yields a direct expression for the lattice parameter.

$$a_0 = \frac{\lambda\sqrt{h^2 + k^2 + l^2}}{2sin\theta} \tag{28}$$

While this expression is true for all cubic lattices, it fails to consider lattices with multiple atoms at a single lattice point, the so-called basis, such as diamond or zinc-blende structures studied here. For zinc-blende structures, certain Miller indices will not produce

diffraction because of the interference that occurs due to the presence of additional atoms forming the basis. For instance, in the CdTe system, the (200) plane will not produce a diffraction peak, so the (400) plane must be used instead. A shorthand list of conditions for diffraction peaks to occur for a few crystal structures is provided in Table 3 below.[40]

Table 3. Rules and conditions for diffraction peaks to occur in XRD measurements.

Crystal structure	**Condition for peak to occur**
Simple cubic	Any h, k, l
Body centered cubic	$h + k + l =$ even
Face centered cubic	h, k, l all even or all odd
Diamond	h, k, l all even and twice an even #, or all odd Note: the all-even scenario will be more intense than the all-odd.

XRD measurements were performed at TXST on a Rigaku SmartLab X-Ray Diffractometer. This system uses a monochromatic Cu $K\alpha$ x-ray source of wavelength 1.54 Å. A basic schematic of a Bragg-Brentano XRD set up as well as the basic physical principles involved are shown in Figure 17. This system was used to perform rocking-curve measurements. Proper alignment is of crucial importance for rocking-curve measurements. Consider the geometry of the system shown in Figure 17. Here, Θ is the angle of incidence, Ω is the angle of reflection, χ is the tilt angle, and Φ is the rotational angle. In a perfect system, Θ and Ω would be exactly equal at the diffraction condition, χ

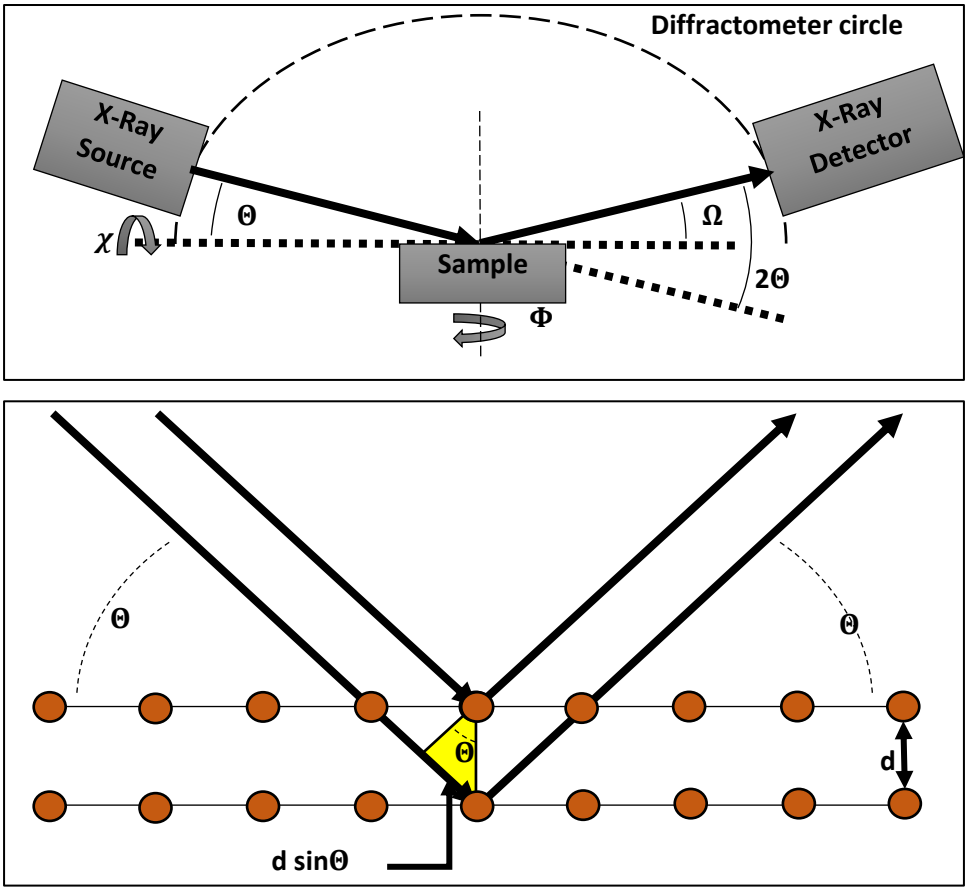

Figure 17. A simplified diagram of a typical XRD setup (top) and a detailed depiction of the geometry involved in the Bragg equation (bottom).

would be zero, and any change in Φ should not produce changes in the intensity of the detected signal. However, in real world systems, Θ and Ω will have slight differences, χ would be non-zero, and changes in Φ will change the intensity due the surface of the crystal not being parallel to the plane of interest, which would occur with the presence of an off-cut orientation. To correct for this, the strongest diffraction peak, typically, that of the substrate, is used to optimize the alignment. Ω, χ, and Φ are swept over small ranges to increase the overall intensity of the substrate peak. Once diffraction condition for the substrate peak has been optimized, Θ is swept over a small region of interest, while the

detector is rocked over the corresponding region in Ω. This produces high-resolution scans over a small region, from which the interplanar atomic spacing of the crystal lattice was determined. This, in conjunction with Vegard's law, was used to determine alloy composition in $CdSe_xTe_{1-x}$ layers.

2.4 Hall Measurements

2.4.1 Simple Hall

Hall measurements were used to determine the carrier concentration of PbTe:Tl and SnTe:Tl films. This measurement technique is well-established and is based around the Lorentz Force, which describes how a moving charge, in the presence of a magnetic field will be deflected

$$\vec{F} = q(\vec{v}\, x\, \vec{B}) \tag{29}$$

Here, $\vec{v}$ is the velocity of the charge, $\vec{B}$ is the magnetic field, and q is the magnitude of the charge. For a sample with applied current, I, in a steady state magnetic field, B, perpendicular to the plane of the sample, the Lorentz force will cause a buildup of charge on the edges of a sample. Once enough charge has built up to create an internal electric field equal in strength to the Lorentz force but opposite in direction, charge will flow uninhibited through the sample. This represents an equilibrium condition which can be expressed as

$$qE = qv_dB \tag{30}$$

where q is the charge of the carrier, E is the (internal) electric field, B is the magnetic field strength and v_d is the drift velocity of the charge carrier. The applied current can be expressed as

$$I = nqv_dA \tag{31}$$

where n is the charge carrier concentration, and A is the cross-sectional area of the sample, defined as the thickness, t multiplied by the length, l. Rearranging the previous relation to solve for v_d and substituting into the above yields

$$I = nq\left(\frac{E}{B}\right)A \tag{32}$$

The internal electric field is related to the potential difference V between the edges of the sample, separated by length l.

$$E = \frac{V}{l} \tag{33}$$

Substituting into the previous and rearranging, we arrive at the so-called Hall voltage

$$V_H = \frac{IB}{nqt} \tag{34}$$

This is the quantity measured in Hall measurements. Based on the resultant sign of the Hall voltage, one can quickly surmise the carrier type present in the sample. Similarly, the Hall coefficient, R_H is defined as

$$R_H = \frac{1}{nq} \tag{35}$$

The mobility, μ, of the charge carriers can also be determined, so long as the resistivity, ρ has been determined. For Hall measurements taken in a Van der Pauw

configuration, the resistivity is numerically determined by measuring the resistance across two perpendicular axes, R_a and R_b and solving

$$\exp\left(\frac{-\pi R_a}{\rho t}\right) + \exp\left(\frac{-\pi R_b}{\rho t}\right) = 1 \tag{36}$$

Once ρ and n have been determined, then the mobility can be calculated using

$$\mu = \frac{1}{qn\rho} \tag{37}$$

Note that this is true in the steady state configuration only, i.e. there is no presence of a magnetic field while the resistance measurements are taken.

Hall and Van der Pauw measurements were taken using a BioRad HL5500 Hall system on PbTe:Tl and SnTe:Tl films. Ohmic contacts were formed using indium solder at the center of the edges of the square samples. All contact configurations were measured using an internal switching matrix to provide averages of relevant figures of merit.

2.4.2 Variable Field Hall

In the case where a sample has multiple types of charge carriers, simple Hall measurements at a single magnetic field will yield an overall average of the concentration and mobility of the charge carriers in the sample, depending on each carrier's contribution to the total conductivity of the sample. In a steady state configuration, with a single carrier type, the conductivity of the sample can be determined using the mobility

$$\sigma = qn\mu \tag{38}$$

However, in the presence of a magnetic field, of strength B, perpendicular to the sample, the conductivity in the plane of the semiconductor becomes a tensor

$$\sigma = \begin{bmatrix} \sigma_{xx} & \sigma_{xy} \\ -\sigma_{xy} & \sigma_{xx} \end{bmatrix} \tag{39}$$

where

$$\sigma_{xx} = \frac{\rho}{\rho^2 + (R_H B)^2} = \frac{qn\mu}{1 + (\mu B)^2} \tag{40}$$

and

$$\sigma_{xy} = \frac{R_H B}{\rho^2 + (R_H B)^2} = \frac{qn\mu^2 B}{1 + (\mu B)^2} \tag{41}$$

This represents the first order correction to the linear Hall effect and considers the orbital motion of charge carriers in a magnetic field. When multiple types of charge carriers exist the conductivity of each type adds to the total conductivity. This turns the conductivity tensor components σ_{xx} and σ_{xy} into sums

$$\sigma_{xx} = \sum_i \frac{qn_i\mu_i}{1 + \mu_i^2 B^2} \tag{42}$$

$$\sigma_{xy} = \sum_i \frac{qn_i\mu_i^2 B}{1 + \mu_i^2 B^2} \tag{43}$$

From this, we can see that the conductivity of each carrier type scales with $(\mu B)^2$. This means that as we vary B, the relative contributions of each carrier to the overall conductivity will be revealed. Thus, by varying the magnetic field between Hall measurements, we can determine the electrical properties of multiple charge carriers within a sample. A multiple carrier fit analysis can be performed on the variable field Hall results. This technique requires fitting the n_i's and μ_i's to the data by assuming a given number of layers.

2.5 Energy Dispersive X-Ray Spectroscopy

Energy dispersive x-ray spectroscopy (EDS) is a non-invasive characterization technique that can be used to identify the chemical makeup of materials. This technique is very similar to XPS, but the excitation source and the collected particle are flipped. In EDS, high energy electrons, typically from an electron beam, are incident on a sample, exciting bound (or core) electrons within the sample into higher energy orbitals. These electrons then fall back to lower energy states, releasing energy in the form of characteristic x-rays. These x-rays are then collected in a detector and passed through an analyzer to determine x-ray energies and associated elements. A basic schematic of this is shown in Figure 18.

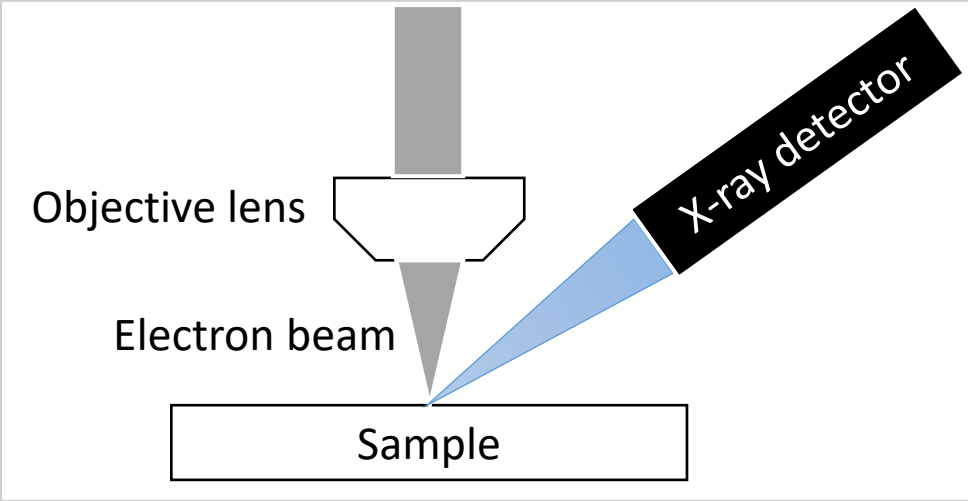

Figure 18. A simplified schematic of typical EDS setups.

Here at TXST, a JEOL JSM-6010PLUS/LA scanning electron microscope (SEM) equipped with a JEOL EX-9400T4L11 Dry SD Extra Detector EDS system was used. The electron beam of the SEM was used to excite electrons within $CdSe_xTe_{1-x}$ films to produce x-rays that were quantifiably analyzed. Single crystal CdTe and CdSe samples

were used as standards to aid quantification. The open source NIST-DTSAII EDS software was used to quantify the overall composition of $CdSe_xTe_{1-x}$ films. For quantification of EDS spectra to be implemented properly, six basic steps need to be taken.

1. Define the list of elements to be analyzed. In this case, Cd, Se, and Te.
2. Perform any calibration of the system that is necessary for quantitative analysis. At a bare minimum, the SEM beam current needs to be measured.
3. Measure spectra from standards for the elements that you want to analyze for. This should be done under the same measurement conditions to be used for sample analysis.
4. Collect spectra from the sample.
5. Process the spectra to calculate the mass fraction or weight percent of the elements present or the percentages of the elements defined in an element list.
6. Assess the quality of the analysis.

2.6 Photoluminescence Intensity Measurements

Photoluminescence Intensity (PLI) measurements are a very useful, non-invasive characterization technique. For this work, two lasers were used, a COHERENT INNOVA 90 laser with excitation wavelength of 514 nm, and an Oxxius S.A. solid state laser with excitation wavelength of 660 nm, to produce electron-hole pairs within the semiconductor samples being tested. With no electrical contact in place, the pairs have

nowhere to go, and end up recombining, either non-radiatively or radiatively, producing photoluminescence (PL). This is an indirect way of measuring the non-radiative defect content in semiconductors. A combination of Raman edge, short and long pass filters in the optical beam path ensure that only photoluminescence is collected, and that no laser light passes through to the detector. The laser excitation was chopped, and the photoluminescence was measured using either a ThorLabs Si amplified photodiode detector or a Hamamatsu R943-02 photomultiplier tube (PMT), spanning over 10 orders of magnitude in detection capabilities, in conjunction with a lock-in amplifier to decrease noise in the signal and reduce any detection of ambient light. A schematic of this technique is shown in Figure 19 below. Combining the known spot size of the laser with the absolutely power of the light used, as determined by a calibrated ThorLabs optical power meter, the PLI efficiency, defined to be the PLI divided by the excitation intensity, was monitored as a function of excitation intensity. Neutral density or optical density (ND and OD respectively) filters are used to step down the absolute laser power in a known, controllable, and repeatable fashion over 7 orders of magnitude. This typically results in an “S” shaped curve. At the low excitation end of the curve, we are considering the low-injection regime where the carrier lifetime and surface recombination velocity are well defined. At the high end of the curve, we are considering the high-injection regime where the PL of the sample is reaching the radiative limit and is approaching 100% internal quantum efficiency. From this, information on recombination, interface trap state density and trap state energy can be determined with appropriate analysis. This technique was used on device and mirror structures to monitor any improvements in recombination at the back interface.

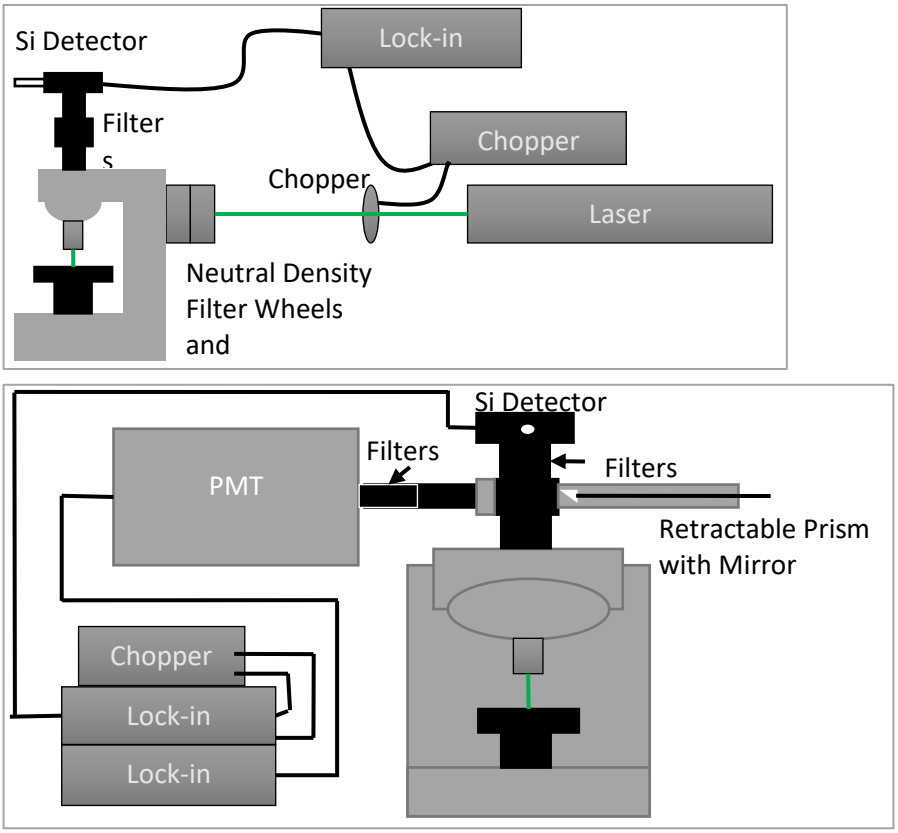

Figure 19. Schematic of PLI setup at Texas State University.

Because of the strong dependence on accurate input intensity that PLI analysis requires, a daily calibration routine was performed before measurements were taken to ensure consistency between measurements. To do this, the power of the laser on the stage was measured using a NIST traceable power meter and adjusted if necessary, to match an agreed upon value. The laser alignment was then checked using a calibration sample on the stage and removing the Si Detector from the setup, allowing the reflected laser light to pass through the top of the microscope onto a target placed on the ceiling. Mirrors in the beam path were adjusted as necessary to hit the target. This target was placed relatively far away, so that small changes in the beam path were exaggerated and could be finely tuned accurately, and repeatedly. In addition, the magnified laser spot on the

target was geometrically linked to the spot size on the sample. By focusing to get the same reflected spot size on the target, we ensured the same spot size on the sample. After alignment of the laser, the PL of a standard GaAs/AlGaAs DH calibration sample was taken. The phase of the Lock-In Amplifier was adjusted to produce the maximum signal. The standard calibration sample was then measured in an agreed upon spot, and the value of the reading was checked. For consistency, this measurement was intended to produce the same value every time it was measured. If there was variation in the measurement, then slight adjustments to the laser alignment would be made, usually in the form of very small changes in the stage height to fine tune the spot size. If a change in stage height occurred, then the power of the laser at the stage would be re-measured to ensure that it had not changed. Once everything was determined consistent, then the sample to be tested would be placed on the stage, the Si Detector would be removed again, and alignment of the laser with the target on the ceiling would be verified for again. If it were misaligned due to a surface gradient on the sample, then adjustments to mirrors in the beam path would occur. Only by performing this strict calibration routine before every measurement we were able to determine absolute efficiencies and accurately compare measurements for different samples.

For structures that were measured through glass, i.e. device and mirror structures, a slight alignment adjustment needed to occur to ensure that the laser light was properly focused on the film to be measured, and not on the surface of the glass. To correctly adjust for this, one must consider the refraction dynamics of the laser as it passes through the glass. As the light passes through the glass, which has a higher index of refraction than air, the light will be bent towards the normal, extending the point of convergence by

some distance x. Using small angle approximations, this extended distance can be described with the following

$$x = t\left(1 - \frac{1}{n_2}\right) \tag{44}$$

where t is the thickness of the glass, and n_2 is the index of refraction of the glass. If the thickness of the glass, t, and the thickness of the standard sample, $t_{standard}$, used to focus the beam were of the same thickness, then x would describe the change in stage height needed to ensure that the beam is focused on the film. However, in the more general case when the thicknesses are not the same, the change in stage height is given by

$$\Delta h = t_{standard} - x \tag{45}$$

where Δh is the change in stage height needed for proper alignment. This is shown in Figure 20.

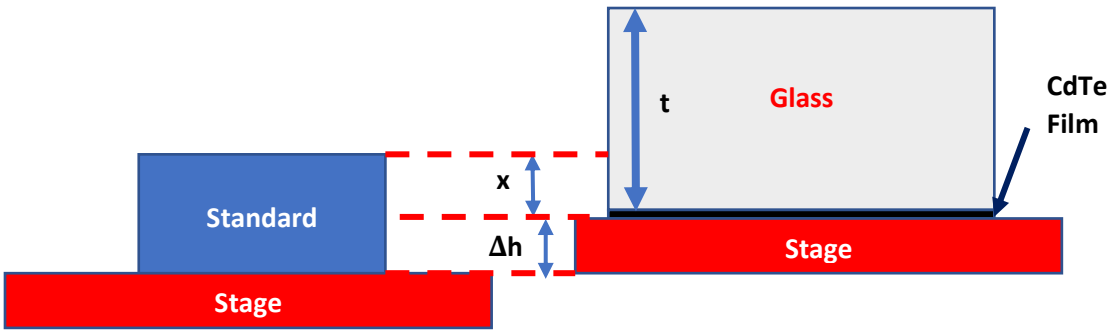

Figure 20. Geometry considerations for adjusting the stage height when measuring PLI through glass.

A typical PL curve exhibits an "S" shaped curve like those shown below in Figure 21. At the low end of the curve where it begins to flatten out, we are considering the low-injection regime where surface recombination dominates, and the lifetime and surface recombination velocity are well defined. At the high end of the curve where it begins to

flatten out again, we are considering the high-injection regime and PL of the sample is beginning to reach the radiative limit. This sample is also approaching 100% internal quantum efficiency and radiative recombination dominates. In between the two, the physics of the PL is complicated and dominated by a mix of non-linear effects. The interface trap state density the energy of the trap states affects the slope of the curve between the two well defined regimes. Due to the complexity required for modelling this behavior, this work will mainly use PLI as a qualitative assessment of these dynamics.

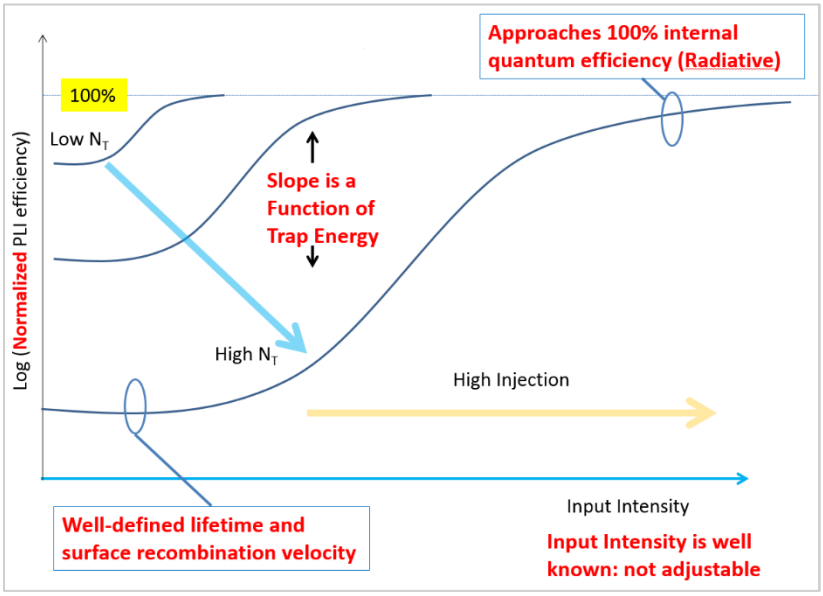

Figure 21. Basic concepts for interpreting PLI data

2.7 Photoluminescence Spectroscopy

While PLI provides a non-invasive technique for assessing the overall PL response from a device, photoluminescence spectroscopy (PL spectroscopy) can provide more details about the nature of the PL. Here, the same lasers used in PLI were used to

excite PL from semiconductor samples. The subsequent PL was then passed through a fiber optic cable to an Acton Research Corporation SpectraPro 300i monochromator where the PL was separated by wavelength using either a 300 line/mm or 600 line/mm grating and sent to a liquid nitrogen cooled indium gallium arsenide (InGaAs) linear array CCD detector, where the spectrum was spread along the array. The alignment process for this technique was the same as the PLI technique, with a few added steps. The standard GaAs/AlGasAs DH from Motorola was used to align the laser. Once the standard returned the expected PLI response, the chopper for the laser was turned off, setting the laser to a continuous mode use. From there, a background spectrum with the light to the monochromator blocked was obtained from the InGaAs detector, with no intentional external excitation. With the monochromator set to the laser wavelength, the laser was passed through to the detector and fine adjustment screws on the fiber optic cable were used to optimize the signal. From there, the standard was swapped out for the sample to be tested, and the monochromator moved to the region of interest. Before collection of every data set, a background spectrum was taken to help eliminate detector dark current from the spectrum. The InGaAs detector produced a reasonable amount of dark current during a measurement because of defect generation, hence the need to collect a "dark" background which could then be subtracted out of the spectra. A Voigt line shape was then used to identify the peak of the PL spectrum. Although not strictly correct, this peak energy was taken as the band gap of the sample. This technique was used to identify the band gap energy of $CdSe_xTe_{1-x}$ alloys which could be used to determine alloy content.

2.8 Time Resolved Photoluminescence Measurements

Time-Resolved Photoluminescence (TRPL) measurements are another non-invasive characterization technique used in this study. The measurement principles are similar to PLI and PL spectroscopy: laser excitation of energy greater than the band gap energy of the material to be tested is used and the subsequent photoluminescence emission is collected, however this time, the collection is in respect to time. TRPL aims to measure the time-response of a single photon that has been emitted from a semiconductor via PL. Because PL emission is dominated by quantum mechanics, which is probabilistic in nature, TRPL requires many successive measurements for statistical accuracy. A pulsed laser source is typically used for excitation, with pulses on the order of 100s of kHz. As with the previous PL characterization methods described earlier, care is taken to filter out all laser light to make sure that only PL emission is detected by a PMT. The time-correlated single photon counting (TCSPC) technique with a PMT that has a response time on the order of 100s of picoseconds is the most common method for detecting single photon emission. The simplest analogy for this technique is a stopwatch. The start of the pulse origination from the laser acts as the "Start", while the detection of a photon acts as the "Stop", and the time difference is collected in "bins" to generate a histogram response curve. From this curve, charge carrier lifetime in semiconductors can be determined. A simplified diagram is provided in Figure 22 below.[41]

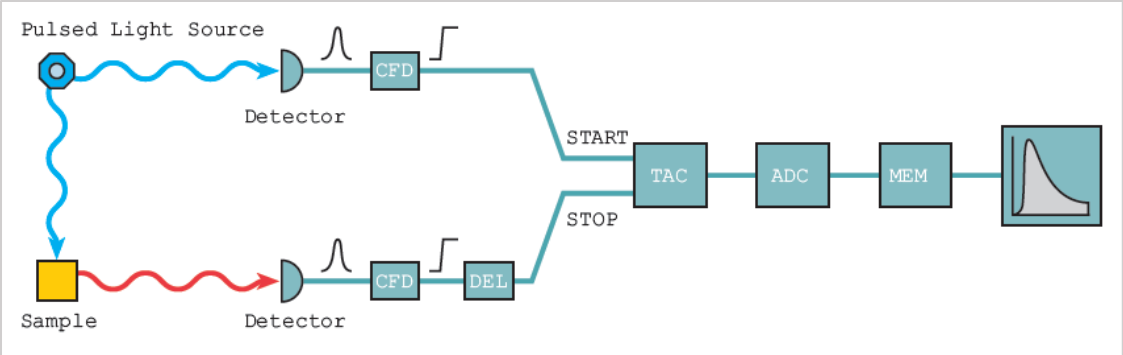

Figure 22. Simplified schematic of a typical TRPL set up.

This technique was performed by a collaborating researcher, Deborah McGott, at NREL on device and mirror structures with PbTe:Tl and SnTe:Tl back contact buffer layers to assess the effects on carrier lifetime. There, two fiber coupled diode lasers with excitation at 670 nm and 405 nm, with a 150 ps pulse width at a repetition rate of 1 MHz, in conjunction with an avalanche photodiode detector, were used to perform measurements.

TRPL measurements explore minority carrier lifetimes in the material being tested. The lifetime of a material is of crucial importance due to its relation to the V_{oc} of a device shown below.

$$V_{oc} = \frac{kT}{q} \ln\left(\frac{g_0 N_d \tau_p}{n_i^2}\right) \tag{46}$$

where N_d is the majority carrier concentration, n_i is the intrinsic carrier concentration, g_0 is the generation rate, and τ_p is the minority carrier lifetime. Recall that the V_{oc} is related to the overall efficiency of a solar device through the following

$$\eta = \frac{V_{oc} J_{sc} FF}{P_{in}} \tag{47}$$

Through this we can see that if we can determine a way to increase the minority carrier lifetime in a photovoltaic device, we should be able to increase the device efficiency, hence the attention we are giving to lifetime measurements based on TRPL.

It would be misleading to say that the lifetime as measured by TRPL *is* the minority carrier lifetime in the material being tested. The charge carrier dynamics in TRPL, especially when performed on a device structure, are simply too complex to make this simple statement. Instead, TRPL measurements give an *effective* lifetime that we associate with the minority carrier lifetime. Indeed, TRPL studies of effective lifetimes in CdTe solar cells, performed by Metzger et al. [9], correlate well with measured device performance, particularly improvements in V_{oc} as shown in Figure 23 below.

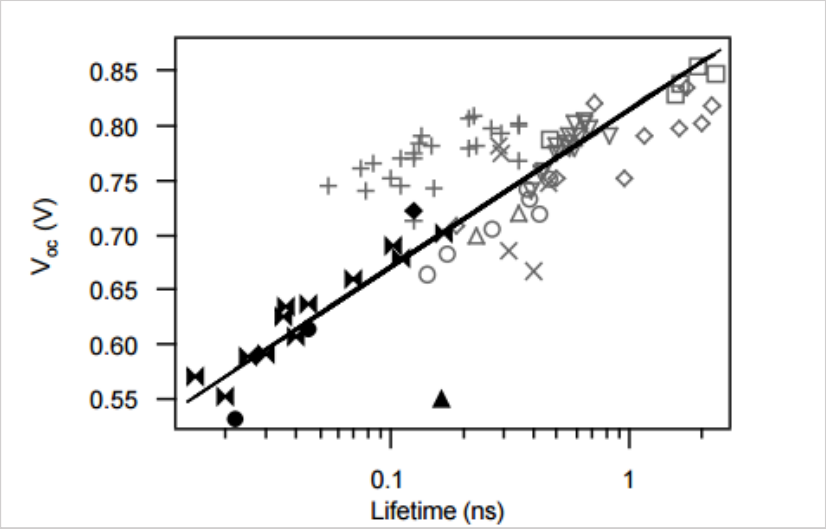

Figure 23. Results of previously reported research showing improvements in lifetime lead to improvements in V_{oc}.

The histogram produced from TRPL measurements is typically interpreted with a bi-exponential fit, i.e. there are two lifetime parameters that the curve depends on. In order to find the effective lifetime, the following approximation is typically taken

$$\frac{1}{\tau_{eff}} = \frac{1}{\tau_{bulk}} + \frac{1}{\tau_{surf}} \tag{48}$$

Where τ_{eff} is the effective lifetime (the overall measurement lifetime), τ_{bulk} is the minority carrier lifetime in the bulk, and τ_{surf} is the lifetime associated with the surface of the material. Through the form of the previous relation, we see that whichever term is larger, τ_{bulk} or τ_{surf}, will dominate and give a rough estimate of τ_{eff}. The lifetime of the bulk is dependent on Shockley-Reed Hall, Auger, and Radiative recombination through

$$\frac{1}{\tau_{bulk}} = \frac{1}{\tau_{SRH}} + \frac{1}{\tau_{Auger}} + \frac{1}{\tau_{Rad}} \tag{49}$$

Depending on the type of material being tested, one or more of these recombination mechanisms may dominate, giving more insight into the charge dynamics. However, determining specifics can be incredibly difficult, especially if performing TRPL on a device. Using the appropriate software, a fit can be performed on the TRPL histogram to determine the two separate lifetimes. This fit follows the form

$$I = I_o\left[A_1 \exp\left({}^{-t}/_{\tau_1}\right) + A_2 \exp\left({}^{-t}/_{\tau_2}\right)\right] \tag{50}$$

Where I is the intensity of the PL emission, A_1 and A_2 are constants, and τ_1 and τ_2 are the lifetimes associated with the faster and slower portions of the bi-exponentially decay, respectively.[42] Often, the longer lifetime from the bi-exponential decay, τ_2 is correlated with the bulk lifetime, τ_{bulk}, while the short τ_1 is correlated with the surface lifetime,

τ_{surf}. In practice, one is typically most interested in the longer lifetime as it is the strongest indicator of device performance.

2.9 Variable Angle Spectral Ellipsometry

At its core, spectral ellipsometry measures the change in polarization of reflected light incident on a thin-film sample, and compares this change to a model to extract materials properties. The properties, such as layer thickness, refractive index or dielectric constant, determine the exact nature of the change in polarization. This technique exploits the phase information, or polarization state, inherent in the incident and reflected light beams.

To describe in more detail, we need a working definition of light. Light is composed of many electromagnetic waves that can be described using Maxwell's equations. The result of Maxwell's equations give us two equations that totally describe an electromagnetic plane wave[43]

$$\tilde{E}(z,t) = E_0 e^{i(kz-\omega t+\delta)} \tag{51}$$

$$\tilde{B}(z,t) = \frac{E_0}{c} e^{i(kz-\omega t+\delta)} \tag{52}$$

Note how the above are complex values. The physical fields are the real parts of $\tilde{E}(z,t)$ and $\tilde{B}(z,t)$ and are depicted in Figure 24.[43] Using Euler's formula to get the real portion of the expression above, we can describe the electric field as

$$E(z,t) = E_0 \cos(kz - \omega t + \delta) \tag{53}$$

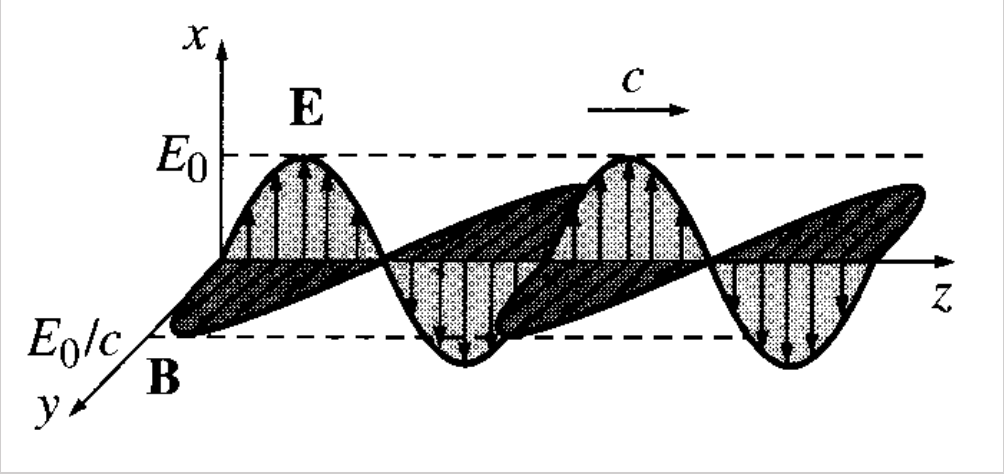

Figure 24. The physical electric and magnetic fields in an electromagnetic plane wave

Now we need to define polarized light. All light, regardless of its polarization can be described as the superposition of two orthogonal electromagnetic plane wave components. These electromagnetic plane waves are typically decomposed into an s component, which is perpendicular to the plane of incidence, and a p component, which is parallel to the plane of incidence. Depending on the phase difference between the s and p components, the light with be polarized differently. If the two components are in phase (the phase difference is zero), then the light is said to be linearly polarized. If the two components are out of phase by 90°, and their amplitudes are equal then the light is said to be circularly polarized. Anywhere in between these two scenarios, the light is said to be elliptically polarized. See Figure 25 below

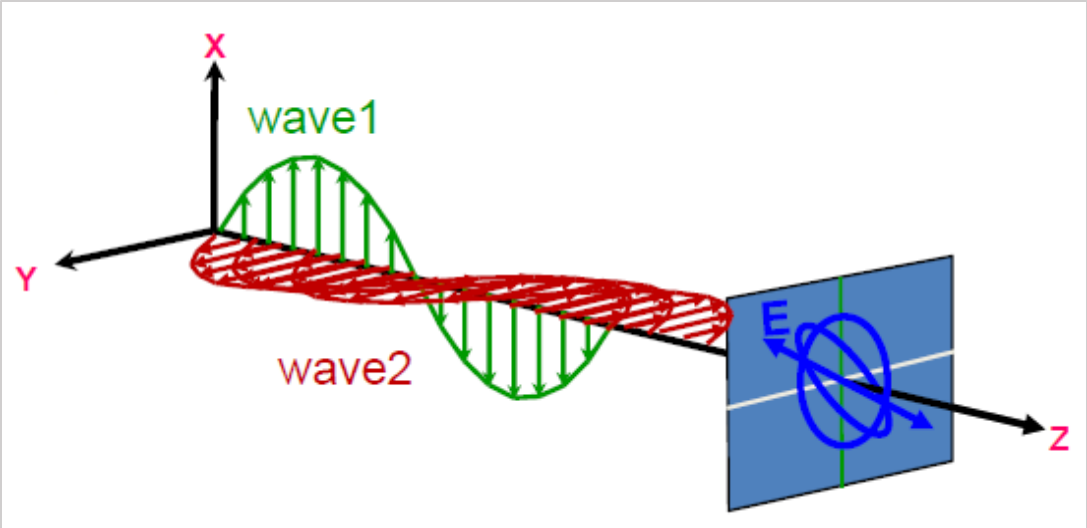

Figure 25. Superposition of a p component with multiple s components, showing the different kinds of polarization. Copyright protected by Woollam company

When light is incident on a material, the material differentiates between the s and p components, and interacts with the two differently. Ellipsometry measures this change in the s and p components after reflection. It does this by determining the complex reflectance ratio, ρ, which is defined as

$$\rho = \frac{\widetilde{R_p}}{\widetilde{R_s}} = \tan(\Psi)\, e^{i\Delta} \tag{54}$$

Where

$$\widetilde{R_p} = \frac{\tilde{E}_p^{reflected}}{\tilde{E}_p^{incident}} \tag{55}$$

$$\widetilde{R_s} = \frac{\tilde{E}_s^{reflected}}{\tilde{E}_s^{incident}} \tag{56}$$

And Ψ and Δ are the specific values that are measured by the instrument. From the relation of ρ above, we can see that Ψ describes the ratio of the amplitudes of the two polarized components, while Δ describes the phase difference between the two.[44]

To determine these values, a typical spectral ellipsometry setup consists of an incident light source that is linearly polarized, typically by using a polarizer, and is then passed through a compensator (typically a quarter-wave plate). After the light has reflected, it is then passed through a secondary polarizer, called an analyzer, and then falls onto the detector (see Figure 26 below). The data that is collected is then compared to a model based on the sample being tested. Most of these models assume that the sample is composed of a discrete number of well-defined layers that are optically homogeneous and isotropic. These models can determine material properties such as film thickness, index of refraction, extinction coefficient and band gap energy to name a few. In this study, ellipsometry was used to determine film thickness of $CdSe_xTe_{1-x}$ alloys and provide an estimate of the band gap energy of the alloy.

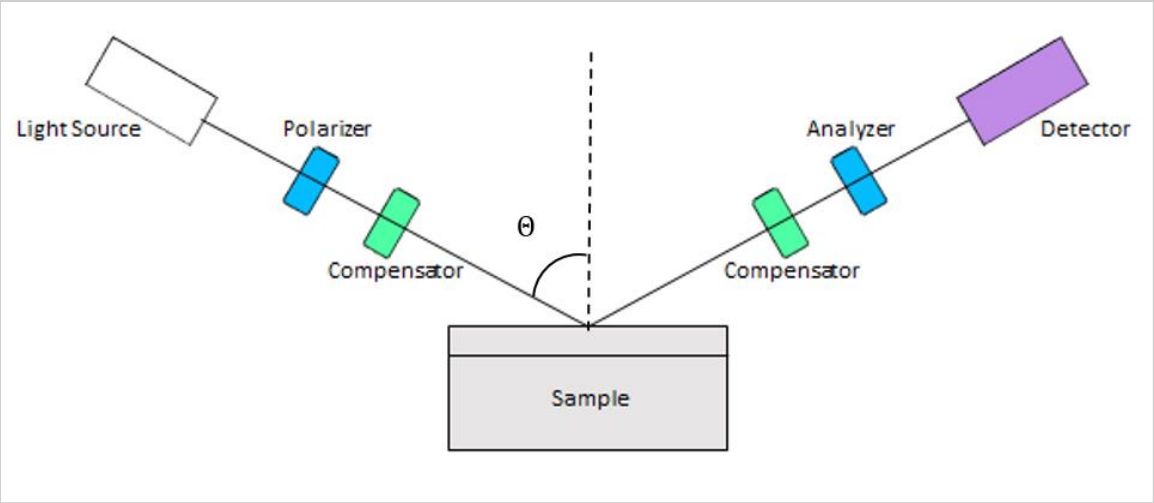

Figure 26. Typical setup for spectral ellipsometry measurements.

2.10 Current Density-Voltage Measurements

For this measurement technique, a completed solar cell is illuminated under AM1.5G conditions using a solar simulator equipped with a lamp designed to mimic the spectrum of the sun. A four-probe configuration is used to contact the device. A current probe and a voltage probe are placed on the back contact of the device, within very close proximity to one another in a Kelvin probe configuration. The same probe configuration is then applied to the front contact of the device. Either current or voltage is then sourced and swept across the cell, while the other is measured. That is, if current is sourced, then voltage is measured and vice versa. This, in combination with a known contact area, produces the typical current density-voltage (JV) response curve for solar cells. From this information, device parameters such as short circuit current density (J_{sc}), open circuit voltage (V_{oc}), fill factor (FF) and efficiency (η) can be measured.

JV measurements were performed by research collaborators at NREL using a Newport Oriel 6” Class ABA solar simulator equipped with a xenon lamp and AM1.5G filter and a Keithley 2400 source-measure unit. It is configured to illuminate the bottom of samples for superstrate architecture devices. Signatone Kelvin probes were used to make four wire measurements. The reference cell used to calibrate the system, calibrated by NREL’s certification group, was a 2x2 cm GaAs cell from PV Measurements to minimize the mismatch factor to CdTe cells. This technique was used to assess the effect on overall device performance for devices with PbTe:Tl back-contact buffer layers.

3. RESULTS AND DISCUSSION

3.1 PbTe

3.1.1 Structures grown for investigations

A variety of structures were fabricated tailored for specific characterization techniques to study the efficacy of PbTe:Tl layers in CdTe based solar cells. MBE was used to deposit all PbTe:Tl layers. These structures include: Hall Structures, XPS structures, Mirror structures, and Device structures. For Hall, Mirror, and Device structures, a series of structures were fabricated with varying levels of Tl incorporation to elucidate the effects of carrier concentration on the overall efficacy of the PbTe:Tl films in CdTe solar cells.

3.1.1.1 Hall Structures

Hall Structures were used to calibrate the Tl_2Te source in the Pb-chalcogenide MBE chamber, yielding requisite control of the carrier concentration in the PbTe:Tl films needed for the studies focused on effects of carrier concentration in the film. To do this, a series of single crystal PbTe:Tl films were grown via MBE on CdTe(211)B substrates, with varying levels of Tl incorporation, achieved by varying the Tl_2Te source temperature in increments of 20°C between samples in the series. The substrates used were prepped for growth using a standard Br:Methanol chemical-mechanical polishing procedure. The film layers in these structures are shown below in Figure 27. The thickness of the grown films was verified for each sample using profilometry on the step edges created by the mask clips on the corners of the sample. Hall was then performed on these samples using small dots of In to contact to the grown film.

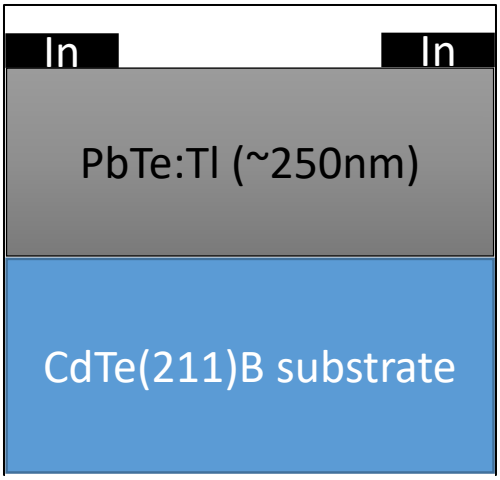

Figure 27. Hall structure layer design.

3.1.1.2 XPS Structures

The XPS structures were designed for XPS measurements in which the VBO with CdTe was to be determined. There were two forms of this structure grown via MBE: CdTe(211)B substrate/PbTe:Tl (p ~ 6.5 x 10^{19} cm^{-3})(250 nm) and CdTe(211)B substrate/PbTe:Tl (p ~ 6.5 x 10^{19} cm^{-3})(~ 10 nm). The substrates used in these structures were prepped using the same polishing procedure as the Hall structures. Due to the extreme dependence on the surface condition of samples for XPS, these samples were exclusively for XPS measurements to minimize contamination of the surface. The film layers for these structures are shown in Figure 28.

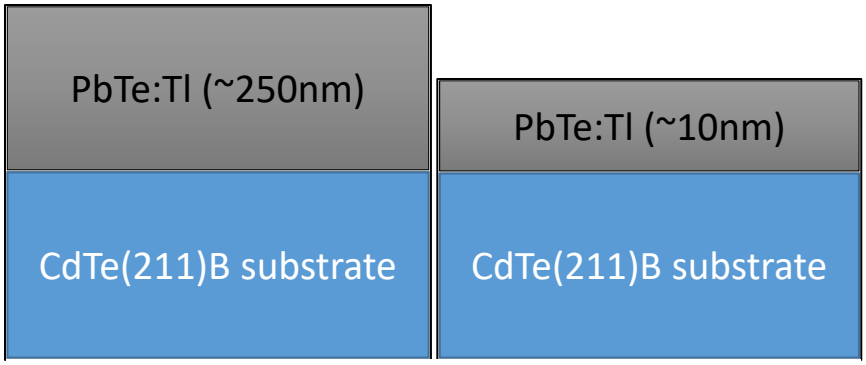

Figure 28. Layer designs for XPS structures in the PbTe investigation.

3.1.1.3 Mirror Structures

The so-called mirror structure is a specific device design that isolates the back interface of a solar cell device as developed by research collaborators at NREL. A typical mirror structure stack as fabricated at NREL includes: a highly fluorine doped tin oxide layer (SnO_2:F) followed by an intrinsic SnO_2 layer deposited on glass via metal organic chemical vapor deposition (MOCVD), an alumina layer (Al_2O_3) deposited via radio frequency (RF) sputtering, an oxygen doped CdS layer (CdS:O) also deposited via RF sputtering, a thick CdTe layer and a cadmium chloride ($CdCl_2$) treatment, both performed via close-space sublimation (CSS), and followed by a copper chloride ($CuCl_2$) dip process to dope the CdTe layer. Except for the Al_2O_3 layer, this stack represents a typical solar cell device as fabricated at NREL. The Al_2O_3 layer is optically transparent and acts as an electron reflector or "mirror". Thus, when the device is probed from the back, with the use of the Alumina layer, we have electronically isolated the back surface/interface so that we may study the dynamics between the CdTe absorber layer and the back contact of the device while eliminating the effects of the front surface/contact from the measurement.

At the start of July 2017, I participated in a 6-month long internship at NREL, where I performed all of the above-mentioned processes, except for the Al_2O_3 layer deposition, to fabricate CdTe solar devices on a regular basis for research. At this time, I developed the $CuCl_2$ dip process and performed stability testing on devices using this method of Cu incorporation. Due to the extended shelf life of samples that were $CuCl_2$ dipped versus samples that had a thin layer of Cu deposited via thermal evaporation and then annealed, researchers at NREL decided to adopt the $CuCl_2$ dip process as part of their standard device fabrication process for research. Previously, Cu incorporation at NREL occurred while depositing the back contact, i.e. Cu deposition followed by ZnTe deposition and subsequent annealing. The $CuCl_2$ dip method also helped to decouple the back-contact deposition and the Cu incorporation, allowing researchers to manipulate the back contact separately from doping the CdTe absorber. Some of this work was also shared with collaborators at the University of Toledo and used as supporting material for a manuscript submitted to IEEE as part of the 2019 Photovoltaic Specialists Conference (PVSC). Mirror structures as described above were shipped to TXST from NREL for subsequent MBE deposition of PbTe:Tl films with varying Tl concentrations. Due to the polycrystalline nature of the CdTe layer as deposited by CSS, subsequent PbTe:Tl deposition was also polycrystalline. The film stack in these mirror structures is shown in Figure 29. These mirror structures were designed for the optical characterizations in this investigation, namely, PLI and TRPL measurements.

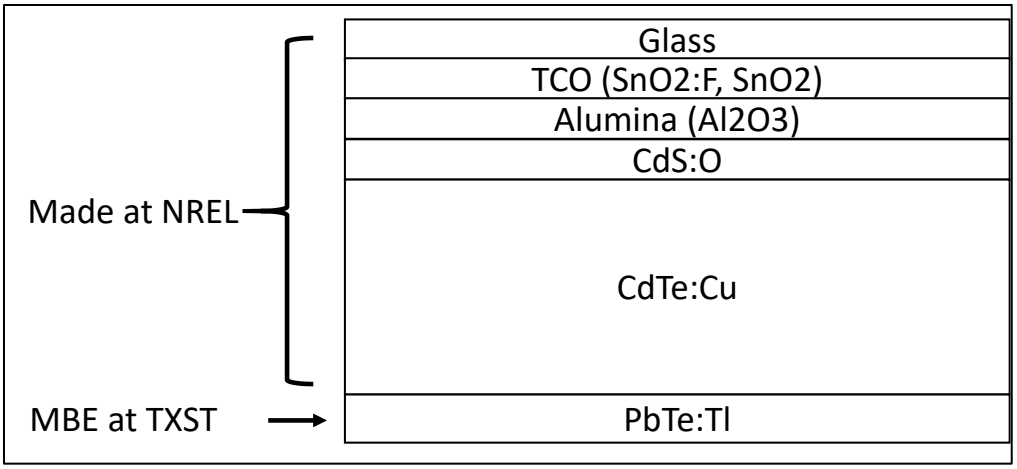

Figure 29. Layer design for mirror structures used in the PbTe investigation.

3.1.1.4 Device Structures

The last structure to be investigated will be the typical solar cell device structure for CdTe cells. A typical device structure as fabricated at NREL includes: SnO_2:F/i-SnO_2 deposited on glass via MOCVD, followed by CdS:O deposited via RF sputtering, followed by a CdTe layer and a $CdCl_2$ treatment, both performed via CSS, and finished with a $CuCl_2$ dip process for doping. As mentioned previously, I fabricated many devices during my time at NREL. Device stacks were fabricated by collaborators at NREL and shipped to TXST for MBE deposition of a series PbTe:Tl back contact buffer layers with varying doping levels. Once again, due to the polycrystalline nature of the CdTe layer, any subsequent layers were also polycrystalline. After optical characterizations were performed, these devices were shipped back to NREL for back contact metallization, achieved through the use of thermal evaporation of gold (Au), and electrical characterization. The film stack in these device structures is shown in Figure 30. These devices were designed to undergo both optical and electrical characterizations, namely, PLI, TRPL, JV and JVT measurements.

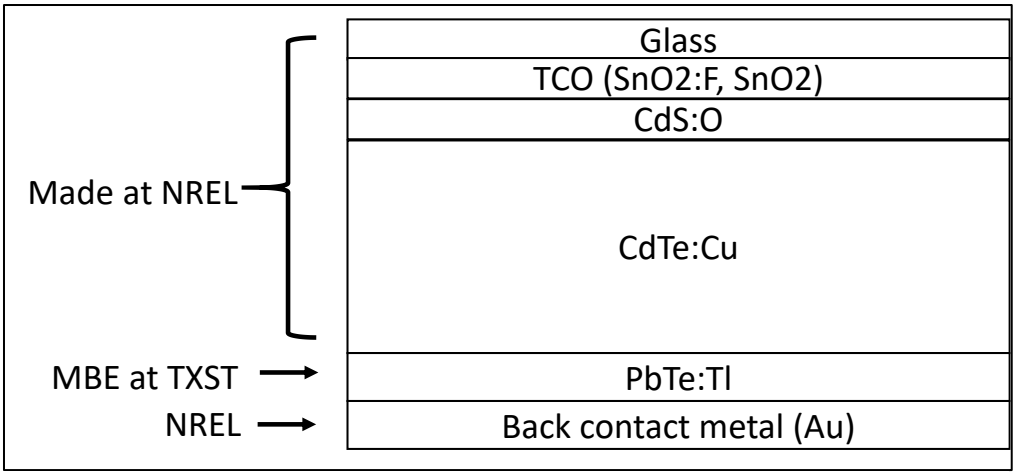

Figure 30. Layer design for CdTe solar cell devices used in the PbTe investigation.

3.1.2 Controlling Carrier Concentration

Before investigation of doping levels in PbTe:Tl films in more advanced structures could commence, calibration of the Tl_2Te source cell was needed to determine appropriate source temperatures for various, desired carrier concentrations. This was done with the use of Hall structures, varying the Tl_2Te source by 20°C between growths and performing simple Hall measurements.

Early in the growth of the series, apparent carrier type switching occurred (n-type carrier concentrations were measured) when attempting lower levels of Tl incorporation. Initially, this was attributed to possible contaminants at the surface of the substrate. Atomic hydrogen cleaning was introduced into the growth process before the substrate was placed in the Pb-chalcogenide growth chamber. However, n-type carrier concentration detection via simple Hall continued to persist. It was suspected that high levels of carbon monoxide (CO) and carbon dioxide (CO_2) were present in the chamber and contributing to the n-type carrier detection. CO and CO_2 can be extremely detrimental for p-type PbTe growth dynamics. With the use of a residual gas analyzer

(RGA) CO and CO_2 presence in the chamber was confirmed. To minimize these levels, we began regular use of a TSP in this chamber. Still, n-type carrier concentrations were detected. An In melting point calibration was done on the manipulator of the chamber to determine if there was a substantial offset between the set temperature and the real temperature of the sample surface. The system was also placed into an "internal bake" configuration overnight, where the temperature of the manipulator was elevated to 500°C to encourage outgassing of the walls of the chamber and the manipulator, which could then be pumped away by any of the various pumps in the chamber. However, PbTe:Tl films were still showing n-type carrier concentrations via simple Hall.

At this point, a grown PbTe:Tl layer that showed negative carrier concentration was sent to EAG Laboratories for secondary ion mass spectroscopy (SIMS) analysis to determine the presence of possible contaminants in the grown film. SIMS results showed the presence of bismuth (Bi), C, and O in the film. Bismuth telluride (BiTe) is one of the source materials installed in the Pb-chalcogenide chamber, and though not purposefully heated during growth, was likely contributing to ambient Bi in the chamber. The presence of Bi in this film was of utmost concern. Bi contamination in p-type PbTe films is highly detrimental because Bi, a Group V element, has one more electron than Pb, a Group IV element, and substitutes for Pb in the lattice structure. This in turn means that any p-type contribution due to the Tl incorporation will be negated by the extra electron from the Bi contamination. The BiTe source had previously been used for Bi-doping in PbTe thermoelectric structures as well as some growth of BiTe films. Thus the chamber and substrate manipulator were contaminated with Bi.

At this point, another In melting point calibration was done in the atomic hydrogen chamber, again to account for an difference between the set temperature of the manipulator and the actual temperature of the sample surface. CO and CO_2 signatures as observed by the RGA were still substantial, particularly once the sample/holder were loaded into the chamber, suggesting that the sample or holder were significant sources of CO and CO_2. The sample holder was then cleaned using a Br:Methanol solution and baked overnight at 240°F. Since the holder had been cleaned and the thermal mass of the holder had been changed due to this, another In melting point calibration was performed in the Pb-chalcogenide chamber. A sample was then grown specifically for SIMS analysis to determine if any of our source materials were contaminated. This stack consisted of a 600 nm layer of potentially non-stochiometric PbTe (only the PbTe source material was open), followed by 600 nm of stochiometric PbTe (this layer had both the PbTe and the Te sources open), and finished with a 600 nm layer of PbTe:Tl (where all three source materials were kept open). SIMS analysis on this sample showed no detectable Bi contamination which could only be detected at levels greater than $1x10^{17}/cm^3$ by SIMS. From this point onward, all growths were performed on a cleaned and baked sample holder. However, n-type carrier concentrations persisted. Another sample was sent for SIMS and showed what could be interpreted as particulate Bi contamination on the surface of the sample, prior to growth. This particulate Bi could have landed on the sample surface due to shutter movement in the system. The SIMS results of this sample, P1419, is shown below in Figure 31.

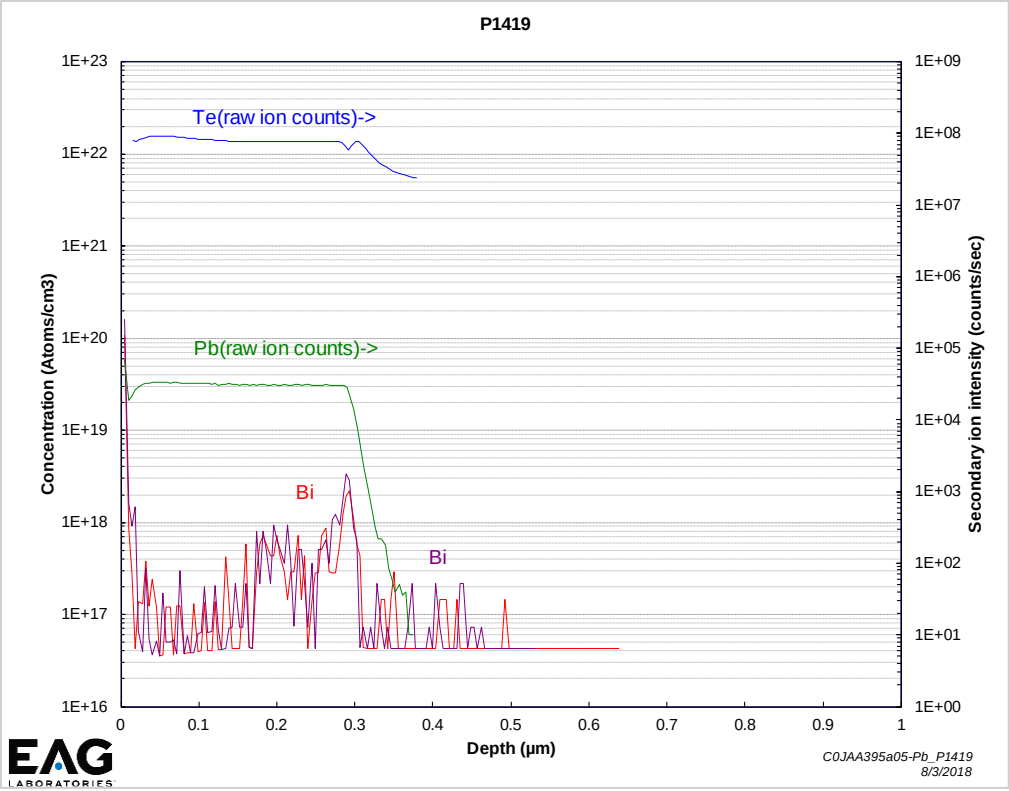

Figure 31. SIMS depth profile of a PbTe:Tl sample showing Bi contamination – provided by EAG Laboratories.

It was decided to open the chamber and perform a deep clean. This involved thorough vacuuming of the system and refilling all relevant source materials. TSP filaments were also replaced. From here, the growth series was essentially "reset", i.e. growths were performed at the upper limits of the Tl incorporation where p-type carrier concentrations were reliably detected, and slowly lowered until n-type carrier concentrations resurfaced, occurring at a lower Tl_2Te source temperature of 360°C. It was suspected that something at the interface of the CdTe substrate and the PbTe film may have still been interfering with the measurement. To investigate this, a PbTe:Tl film was grown intentionally thick to about 1.5 μm, which was about 5x the typical film thickness, to minimize effects of the interface with the Tl_2Te source cell at 360°C. This structure

clearly showed p-type carrier concentration based on simple Hall results. This result suggested the presence of multiple carrier types existing within the PbTe:Tl film with an n-type conduction layer either between the CdTe and PbTe, or on the PbTe free surface.

To properly investigate the presence of multiple carrier types in the PbTe:Tl films, it was decided to measure the "apparent" n-type films using variable field Hall with the use of the PPMS. Analysis of these measurements followed the previously described formalism presented in section 2.4.2 Variable Field Hall, but with necessary modifications applicable to the PbTe system as developed by Dr. Craig Swartz, a collaborating research member at TXST. Namely, adjustments must be made to the conductivity tensor as presented in equations (35)-(39) for semiconductors with anisotropic valleys, where the mobility μ_i is directionally dependent – even if the lattice and band structure have an overall cubic symmetry.[45] A variable field analysis was previously developed for X-valley semiconductors.[46] Although it was erroneously assumed that L-valley semiconductors would have the same conductivity tensor as X-valley semiconductors, as a function of n and μ. To our knowledge, an accurate L-valley tensor does not appear in the literature.

To find the conductivity tensor, we begin with the semiclassical equations governing charge carrier motion in an electric (E) and magnetic (B) field with a scattering/damping force given by mv/τ. In steady state, the net force on a carrier of charge q should average to zero so that

$$0 = q\vec{v} \times \vec{B} + q\vec{E} - \overleftrightarrow{m}\vec{v}/\tau \tag{57}$$

where τ is the scattering time for charge carriers, $\vec{v}$ is the average (drift) velocity of the charge, and $\overleftrightarrow{m}$ is the effective mass tensor. When the z-axis is directed along the longitudinal axis of the L-valley, $\overleftrightarrow{m}$ is diagonal with components m_t, m_t, and m_l, and we can define the mobilities as

$$\frac{1}{\mu_t} \equiv \frac{m_t}{\tau q} \tag{58}$$

For the x and y directions, and

$$\frac{1}{\mu_l} \equiv \frac{m_l}{\tau q} \tag{59}$$

For the z direction. Substituting these definitions into Eq. (49) and solving for the electric field, we find

$$\vec{E} = \left(\frac{1}{qn}\right)\begin{pmatrix} \frac{1}{\mu_t} & -B_z & B_y \\ B_z & \frac{1}{\mu_t} & -B_x \\ -B_y & B_x & \frac{1}{\mu_l} \end{pmatrix}(qn\vec{v}) \tag{60}$$

This can be simplified, by recognizing that $qn\vec{v}$ is the electric current density $\vec{J}$, where n is the carrier concentration, so that the first two terms in equation above is identified as the resistivity tensor $\overleftrightarrow{\rho}$,

$$\vec{E} = \overleftrightarrow{\rho}\vec{J}. \tag{61}$$

The inverse is the conductivity tensor, but what is of most interest is the conductivity tensor for 8 L-valleys which are not aligned along the z-axis, as illustrated in Figure 32.

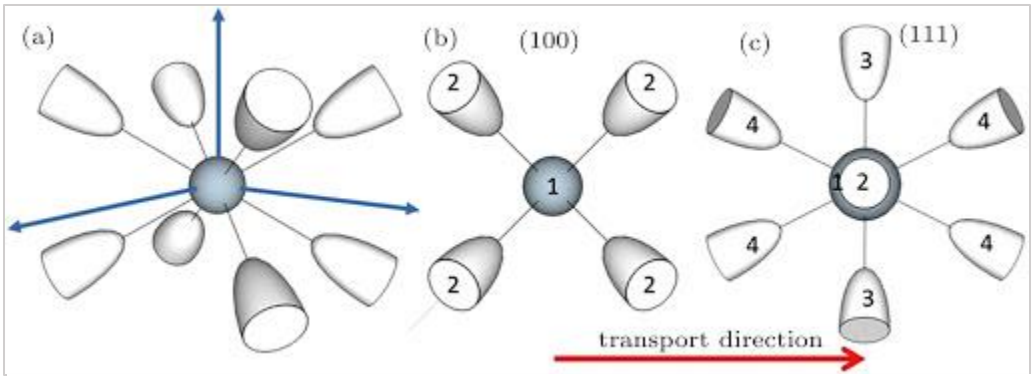

Figure 32. The 8 L-valleys present in PbTe which are not aligned along the z-axis which exhibit anisotropy

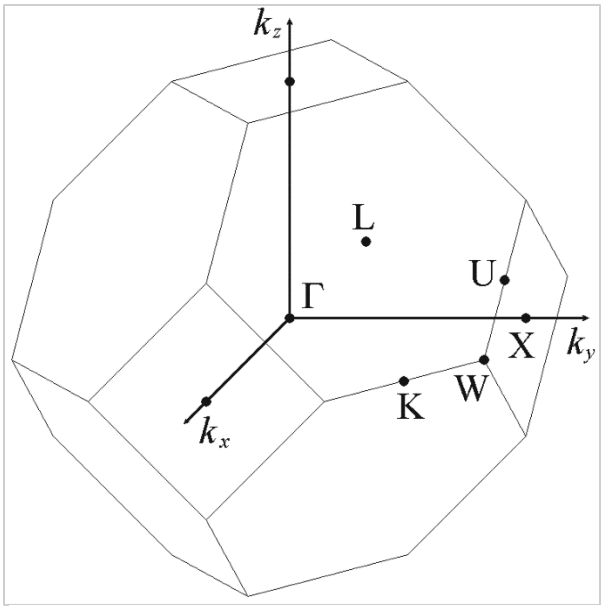

Figure 33. The first Brillouin zone for an fcc lattice structure depicting the location of the L-point, as well as other points of interest.

The upper four L-valleys are reached by a rotation of θ about the $(+1,+1,0)/\sqrt{2}$, $(+1,-1,0)/\sqrt{2}$, $(-1,+1,0)/\sqrt{2}$, and $(-1,-1,0)/\sqrt{2}$ axes. The angle θ is defined by

$$cos\theta = \sqrt{2/3} \equiv c \tag{62}$$

$$sin\theta = \sqrt{1/3} \equiv s \tag{63}$$

So that θ is about 55°. The matrix $\overleftrightarrow{R}$, for a rotation about an arbitrary axis (U, V, W) is given by[47]

$$\overleftrightarrow{R} = \begin{pmatrix} U^2 & UV & UW \\ VU & V^2 & VW \\ WU & WV & W^2 \end{pmatrix}(1-c) + \begin{pmatrix} c & -Ws & Vs \\ Ws & c & -Us \\ -Vs & Us & c \end{pmatrix}. \tag{64}$$

For each valley, the conductivity tensor is given by

$$\overleftrightarrow{\sigma} = \overleftrightarrow{R}^{-1}\overleftrightarrow{\rho}^{-1}\overleftrightarrow{R} \tag{65}$$

Where the values of B_x, B_y, and B_z for a given valley are set by $\left(B_x, B_y, B_z\right) = \overleftrightarrow{R}\,\overrightarrow{B_A}$, and the applied magnetic field is in the z-direction, $\overrightarrow{B_A} = (0,0,B)$. The lower four L-valleys are then found by a rotation of $180° - \theta$, or by changing $c \to -c$.

The conductivity tensors for all 8 valleys are averaged together to obtain, for the measurement condition of $\vec{E}$ in the x-y plane and $\vec{B}$ along the z-axis,

$$\overleftrightarrow{\sigma} = \begin{pmatrix} \sigma_{xx} & \sigma_{xy} & 0 \\ -\sigma_{xy} & \sigma_{xx} & 0 \\ 0 & 0 & \sigma_{zz} \end{pmatrix} \tag{66}$$

Where

$$\sigma_{xx} = \frac{nq\bar{\mu}}{1+\hat{\mu}^2B^2} \tag{67}$$

$$\sigma_{xy} = \frac{nq\hat{\mu}^2}{1+\hat{\mu}^2B^2} \tag{68}$$

$$\sigma_{zz} = \frac{nq(\bar{\mu} + \mu_t^2\mu_l B^2)}{1+\hat{\mu}^2B^2} \tag{69}$$

And we have made the following definitions

$$\bar{\mu} \equiv \frac{2\mu_t + \mu_l}{3} \tag{70}$$

$$\hat{\mu}^2 \equiv \frac{\mu_t + 2\mu_l}{3}\mu_t. \tag{71}$$

Given an anisotropy ratio of $10 = \mu_t/\mu_l$, even a pure PbTe sample without an n-type parasitic layer would give a small-B single field Hall concentration of 1.2 times n. Further corrections of the Hall factor may be made by taking inelastic polar optical phonon (POP) scattering into account, though standard treatments are in error and a corrected scattering rate expression should be used.[48] Though use was made of these conductivity tensor components in the previous reference, they have not to our knowledge been explicitly given before now. It is worth emphasizing again that the above formalism was developed by Dr. Craig Swartz.

Using this corrected conductivity tensor, the data for variable field Hall measurements on the thick PbTe that showed p-type carrier concentrations (vs the thin sample grown under the same conditions which showed n-type carrier detection) was fitted assuming two carrier types and the results are shown in Figure 34. A single layer fit without the thin n-type conduction is shown to demonstrate that a single layer charge carrier model is untenable, and to show that variable field analysis allows multiple conducting layer to be found independently of variable thickness studies.

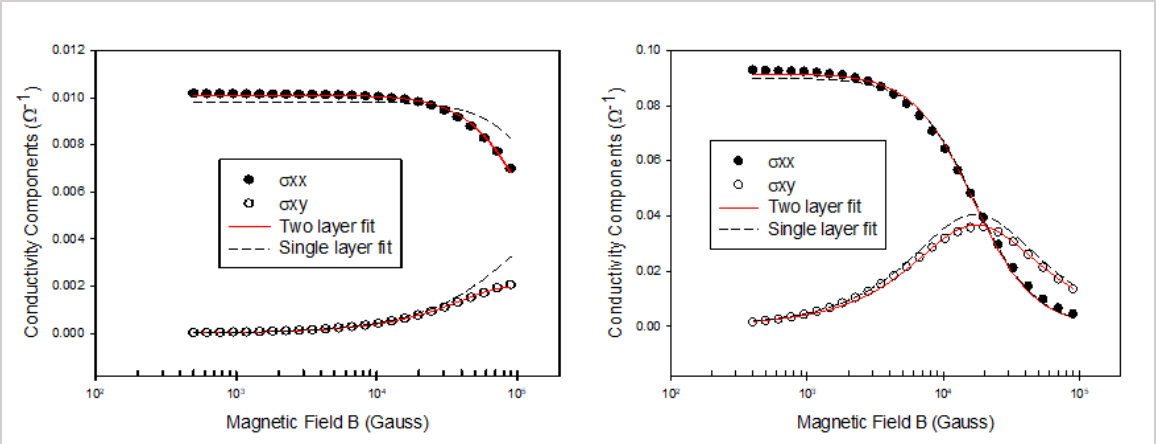

Figure 34. Variable field hall results using modified conductivity tensor. *(Left) Data and fit for measurements taken at room temperature. (Right) Data and fit for measurements taken at 80 K.*

Once satisfied that a two-carrier fit was appropriate, variable field Hall was repeated on previously grown thin PbTe:Tl layers, both those that had presented as positive and negative overall type via simple Hall, at room temperature and at 80 K. The results of the multi-carrier fit analysis are summarized in Figure 35 and Figure 36. A nearly constant thin sheet of n-type charge carriers was found in all samples on the order of $1x10^{13}/cm^2$. This analysis also showed that we had successfully varied the p-type carrier concentration over more than an order of magnitude. With these results, we had successfully calibrated the Tl_2Te source temperature to provide predictable carrier concentrations in PbTe:Tl films deposited on other structures in this investigation.

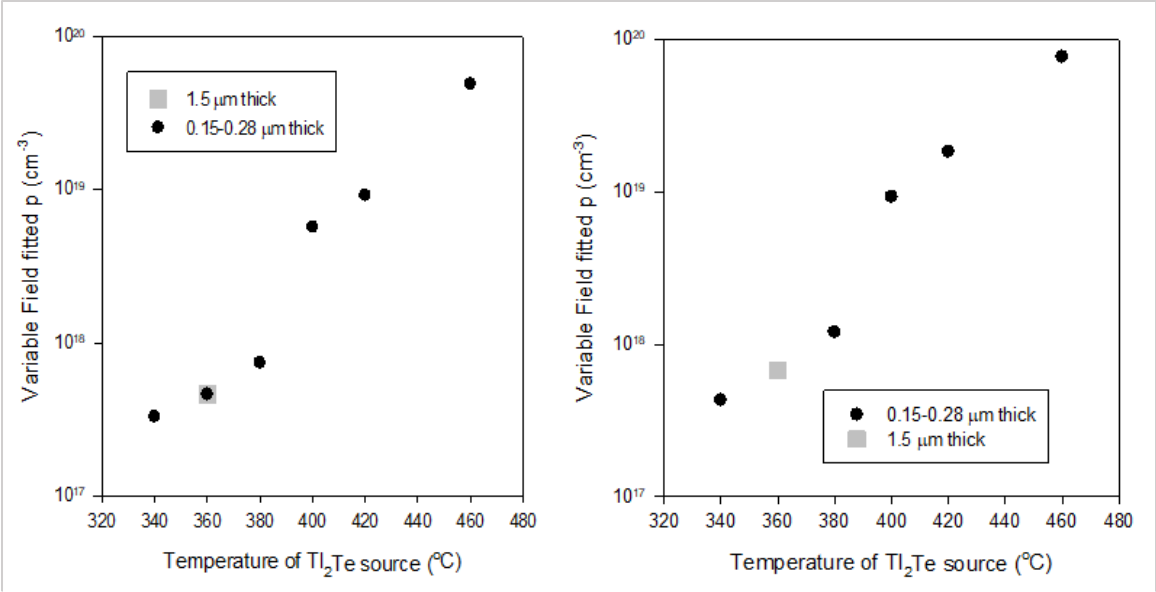

Figure 35. Aggregated p-type carrier concentration results of variable field Hall using multi-carrier fit for (Left) room temperature data and (Right) data taken at 80 K.

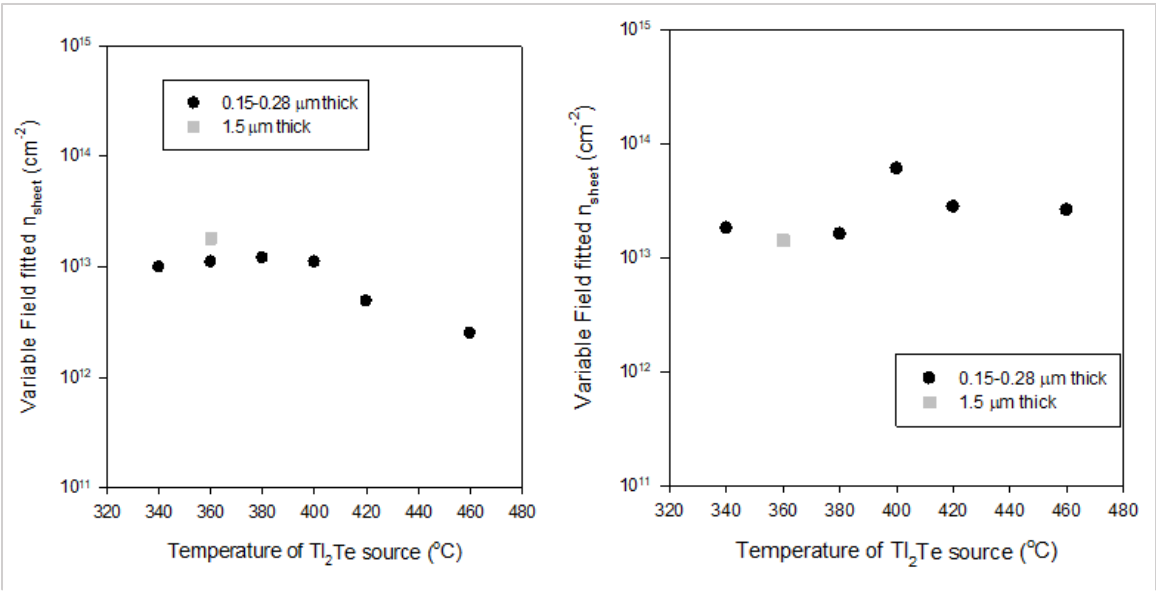

Figure 36. Aggregated n-type carrier sheet concentration results of variable field Hall using multi-carrier fit for (Left) room temperature data and (Right) data taken at 80 K.

3.1.3 Lifetime and Recombination

During my internship at NREL, I added PbTe:Tl and SnTe:Tl layers to device structures for a separate project designed to study the effects of novel back interface preparation techniques on CdTe solar cells. In this study, preliminary TRPL results looked promising.[49] This gave us added impetus to examine PbTe and TRPL was repeated on standard CdTe device structures and mirror structures specifically grown to investigate the effects of carrier concentration on the overall device performance.

An initial, cursory investigation of this was done with a small series of mirror structures with carrier concentrations: $p \sim 6.5x10^{19}/cm^3$ and $p \sim 6.0x10^{18}/cm^3$. For comparison, a control sample that consisted of a bare CdTe film (i.e. this sample had no back-contact buffer layer) was also measured via TRPL. The TRPL results from this cursory investigation are shown in Figure 37. Lifetimes in these data are identified by the slope of the exponential traces. Here, smaller slopes correspond to longer lifetimes. It is worth noting that we see two apparent lifetime components: an initial, quick decay, as well as a longer decay time. The initial decay is representative of the transient state, in which excess charge carriers have been generated due to the laser excitation and are still diffusing throughout the layer and "settling" into an equilibrium state. The longer decay is much more representative of the bulk material properties. With this in mind, we can clearly see that the PbTe:Tl layer with $p \sim 6.5x10^{19}/cm^3$ well out-performs the baseline lifetime. Increased lifetime is indicative of decreased interface carrier recombination. The PbTe:Tl layer with $p \sim 6.0x10^{18}/cm^3$, however, shows the opposite with a significant drop in lifetime compared with the baseline, indicating enhanced recombination behaviors in PbTe layers with this level of Tl incorporation.

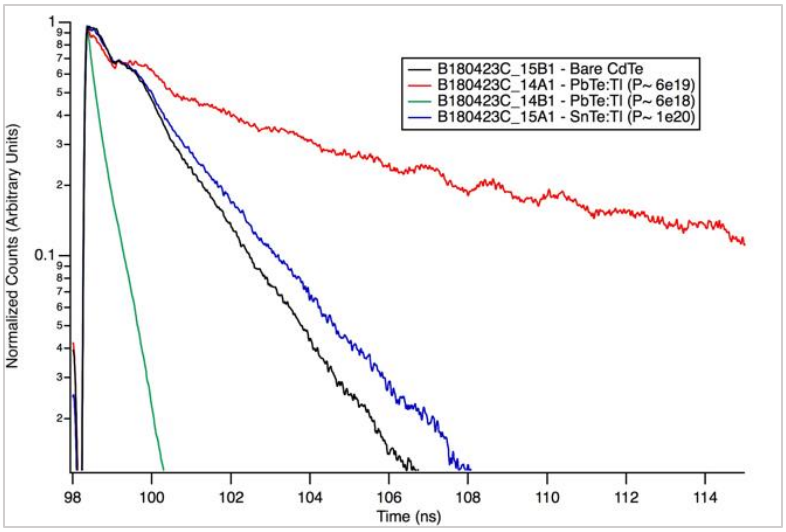

Figure 37. TRPL results on a cursory series of mirror structures with PbTe:Tl back contact buffer layers with varying carrier concentrations on the order of one order of magnitude.

This dramatic change in behavior for a change in carrier concentration of one order of magnitude spurred a more detailed investigation seeking to identify a "turn on" level of Tl incorporation. To accomplish this, another series of mirror structures and device structures were grown with the following carrier concentrations: $p \sim 6.5x10^{19}/cm^3$ (sample P1441), $p \sim 2.5x10^{19}/cm^3$ (sample P1442), $p \sim 1.0x10^{19}/cm^3$ (sample P1443), and $p \sim 6.0x10^{18}/cm^3$ (sample P1444). For comparison, control samples that consisted of bare CdTe films (i.e. these samples had no back-contact buffer layers) were also measured via TRPL (sample B_14A2). All base mirror and device structures provided by NREL were provided from the same growth batches. JV analysis of the 16 other devices in these batches fabricated with the standard process showed an efficiency spread between 13.7% and 16.5% with an average efficiency of 15.5%, so it is worthwhile to note that the base structures used in this study indicated variability in the bare material quality.

A summary of the TRPL results of the second round of mirror structures is shown in Figure 38. While the improvement in lifetime for the highest doped PbTe:Tl film over the control is less obvious, we believe this to be due to the inherent variability we found in the underlying material quality. Upon closer inspection, we see that the bulk lifetime component in the PbTe:Tl layer with carrier concentration $p \sim 6.5x10^{19}/cm^3$is longer than that of the control sample, indicating that the bulk lifetime as discussed in Eq. 47 of this sample was longer than that of the control. All other doping levels considered show marked decreases in lifetime performance in comparison to the control, indicating enhanced recombination behaviors in these samples. Based on these results, we can expect that device performance in samples below the carrier concentration threshold of $p \sim 6.5x10^{19}/cm^3$ will be negatively affected by the inclusion of the PbTe:Tl back-contact buffer layer.

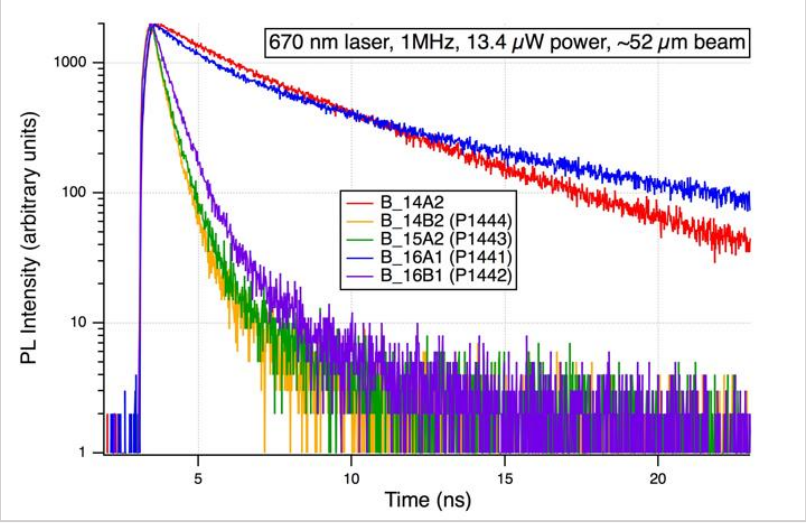

Figure 38. TRPL results on a series of mirror structures with PbTe:Tl back-contact buffer layers, with a more detailed look at how carrier concentration effects lifetime.

TRPL was then repeated on device structures with similar carrier concentrations, the results of which are summarized in Figure 39. Interpretation of the data is a bit more difficult, but there is significant improvement in the lifetime for the highest doped PbTe:Tl layer. All other doping level layers investigated only show a modest improvement over the baseline, which had no back-contact buffer layer deposited. This suggests that devices with the highest doped PbTe:Tl back contact-buffer layer could out perform the baseline devices.

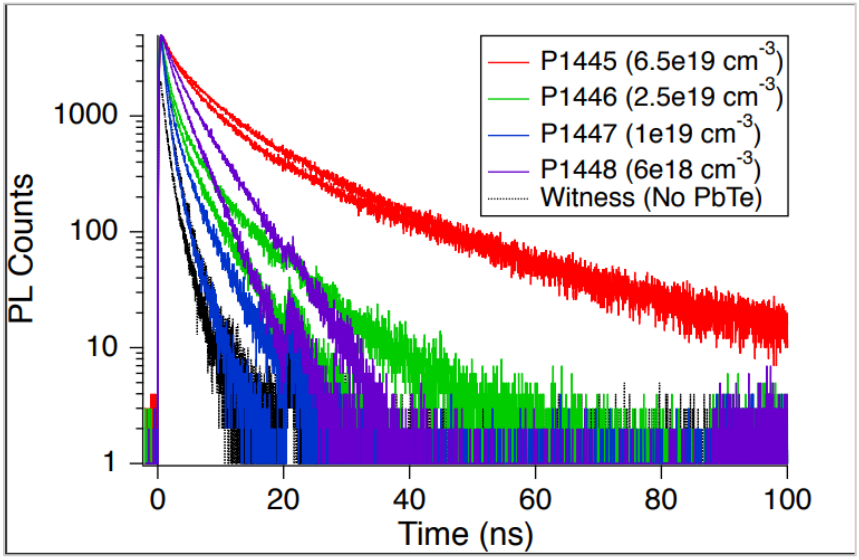

Figure 39. TRPL results on the series of device structures with PbTe:Tl layers where the carrier concentration was varied.

PLI was performed on both sets of mirror structures discussed in the TRPL section above and results of the entire set of mirror structures is shown in Figure 40. From this, we note that there appear to be two groups of results: the controls and the highest doped PbTe:Tl samples, and all other carrier concentrations considered. Here, we can more easily see the variability inherent in the bare material quality. We also

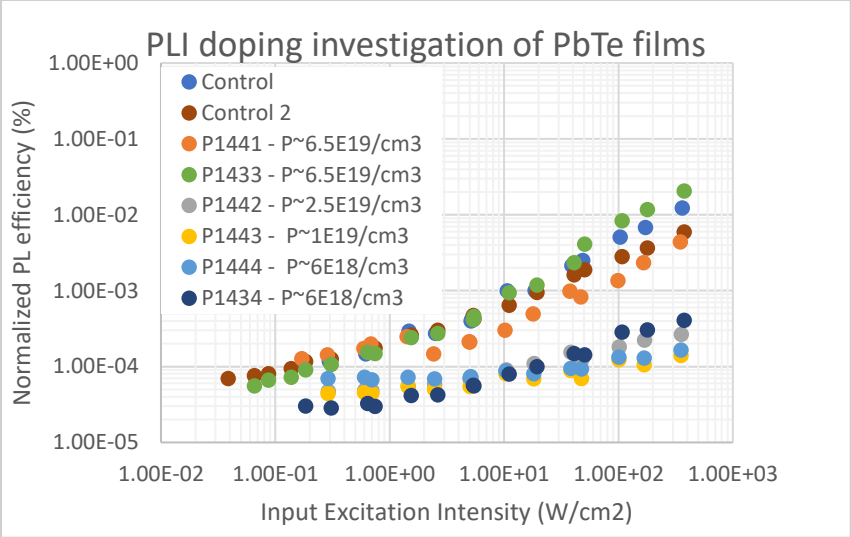

Figure 40. PLI results of all mirror structures with PbTe:Tl back-contact buffer layers.

see that the trends found in TRPL are reflected here as well. Specifically, sample P1433 shows increased radiative recombination compared to the control, indicating a decrease in defect and surface/interface related recombination in this sample, which supports the longer lifetime TRPL results. Also of note, sample P1441 shows decreased radiative recombination at high injection levels, while showing increased radiative recombination at lower injection levels. At lower injection levels, we have a steady state configuration where we have well-defined linear parameters. The response in this range could be interpreted as more bulk-like but is still likely surface dominated. At higher injection levels, non-linear recombination is occurring, and we see the effect of defect state filling with the high density of excess carriers that have been injected by the laser excitation. The larger the PLI response in this region, the less defects are present to “trap” excess carriers, and a larger radiative recombination component is represented. This could be interpreted to mean that the response at low levels is more representative of the bulk recombination behaviors. This specifically supports the TRPL results of this sample, that

show a decreased surface lifetime, but an increased bulk lifetime over the baseline. More detailed characterization and analysis is needed to support this.

For all other carrier concentrations considered, we see decreased radiative response compared to the bulk, indicating increased defect or surface/interface related recombination. This is directly supported by the TRPL results showing decreased lifetimes in these samples.

PLI was not performed on device structures due to the complex nature of the recombination behaviors in a device. Analysis of the PL response of these structures would be non-trivial and is beyond the scope of this dissertation.

3.1.4 Electrical Measurements

JV measurements were taken on the series of device structures with varying carrier concentrations. Unfortunately, there were a number of issues that made interpretation of data and comparison of results difficult. First, the inherent variability in the base material quality complicated interpretation as discussed previously. This makes it difficult to make direct comparisons of results as the base material introduced a significant amount of uncertainty. Further, deposition of the Au contacts was done with a shadow mask, which can result in growth slightly under the edges of the mask, leading to an inaccurate determination of the contact area, crucial for efficiency calculations. Initially JV results showed evidence of bleed-through current as well, due to the highly conductive nature of the PbTe:Tl film. To eliminate this, the devices had to be manually isolated using a blade to scrape away film layers. This further complicated accurate determination of the contact area. To compensate for this, the J_{sc} values of the curves presented were normalized to a typical value for that of CdS/CdTe devices, specifically to

24.5mA/cm^2. Lastly, some of the Au contacts were deposited on areas of the samples where no PbTe existed allowing direct contact to the underlying CdTe, further complicating the results of the series. Any devices where Au was deposited in areas without PbTe layers were basically useless to this study. Because of these complications, less data than ideal is presented here. Ideally, this study would have been repeated over many devices to overcome the uncertainty inherent in the base material quality so that statistically relevant comparisons could be made.

Figure 41 shows the JV results for the "best" performing devices on each sample. Efficiency data will not be provided as interpretation is difficult, for the reasons discussed above. Of particular interest in these curves is the roll-over exhibited, especially for the lower doped PbTe:Tl back-contact buffer layers. What we observe is that as the doping levels decrease, the roll-over appears to become more pronounced. This suggests that at lower doping levels, a back-contact barrier is present and negatively affecting the performance of the device. The purple trace, representative of the lowest doped PbTe:Tl back-contact buffer layer, was also a less than ideal device in that some of the Au contact on this device was in direct contact with the CdTe. For this reason, we cannot say unambiguously that there is a monotonic trend in roll-over present for the devices. However, there is a clear difference between low doped PbTe contacts, the heaviest doped PbTe contact, and the witness sample with the heavy-doped PbTe exhibiting the smallest level of rollover.

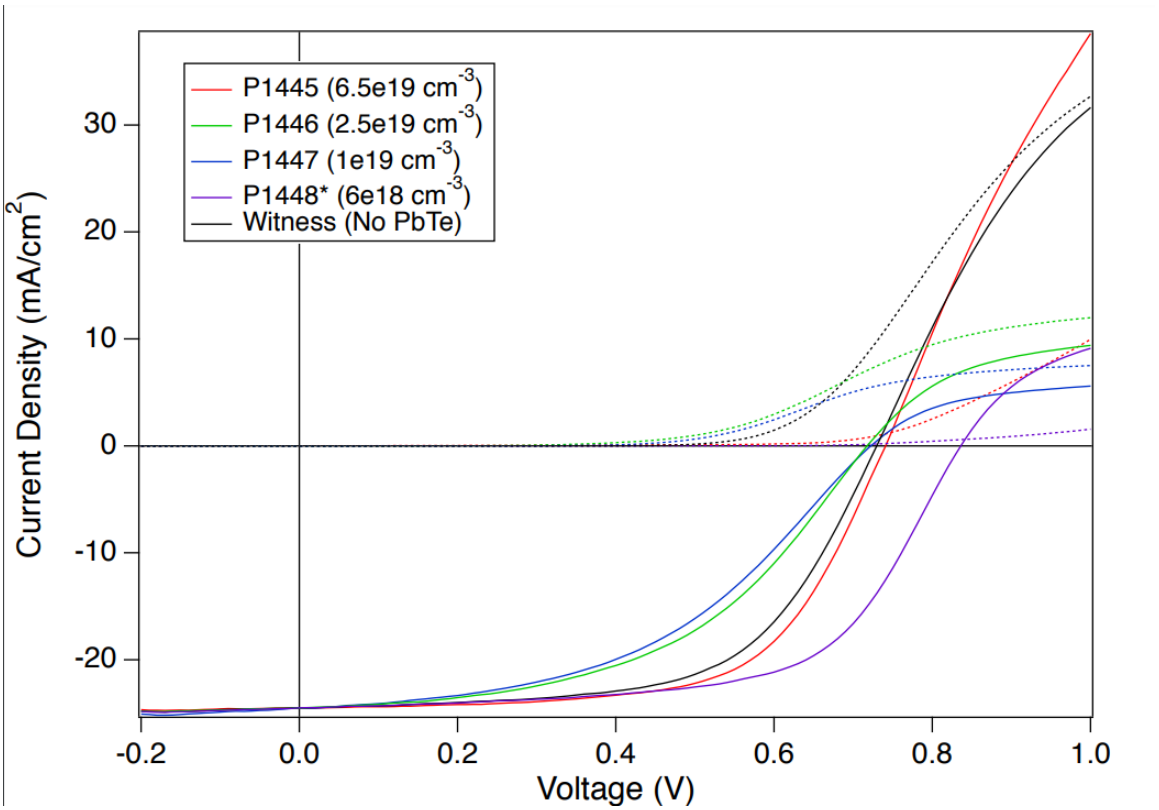

Figure 41. JV results of the "best" performing devices with PbTe:Tl back-contact buffer layers.

3.1.5 Valence Band Offsets

Using the structures specifically fabricated for XPS characterization, XPS measurements were performed on single crystal PbTe:Tl/CdTe films at NREL by Dr. Craig Perkins. Only the maximum Tl incorporation ($p \sim 6.5x10^{19}/cm^3$) was considered for this study. Here, the core-level or Kraut method was employed to determine the VBO between PbTe and CdTe. In this method, specific core-level peaks are monitored for two semiconductors, X and Y, as well as the valence band maxima (VBM) for each semiconductor. First, the VBM and specific core-level energies are measured for the two bulk semiconductors in separate measurements. Second, a thin heterojunction of the two semiconductors is measured to identify any apparent shifts in the core-levels due to the

formation of the junction. This method can be summarized through the following expression

$$\Delta E_v = (E_{CL}^Y - E_{VBM}^Y) - (E_{CL}^X - E_{VBM}^X) - \Delta E_{CL} \tag{72}$$

Here, ΔE_v is the VBO between semiconductors X and Y, E_{CL} is the energy of the core-level peak, E_{VBM} is the VBM position, and ΔE_{CL} is the shift in core-level peaks in the thin heterojunction sample. Figure 42 does an excellent job of identifying the different quantities pictorially.[50] In this study, the Cd 3d5/2 and the Pb 4f doublet (7/2 and 5/2) core level peaks were monitored. A full spectrum survey of thick PbTe:Tl film is shown below in Figure 43 as an example of the spectra data. The VBM of both semiconductors were identified by fitting the data to a broadened, theoretically determined density of states. Fitting of the core-level peaks was performed according to ISO Standard 15472.

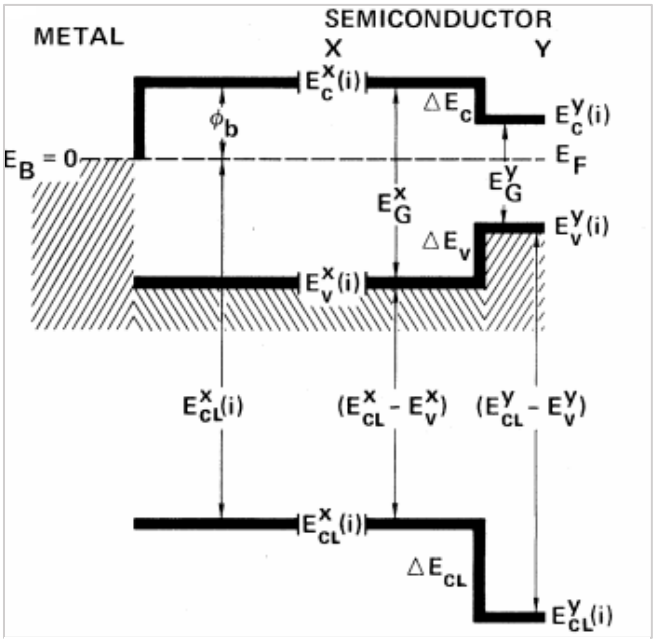

Figure 42. Band diagram depicting the figures of merit needed for accurate determination of the VBO while employing the Kraut method.

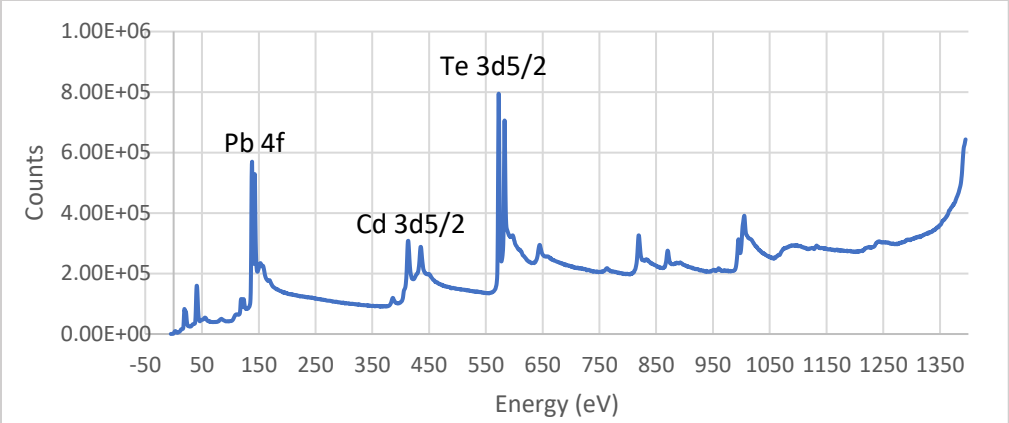

Figure 43. Full spectrum XPS survey data where the peaks of interest in determining the VBO between PbTe/CdTe have been indicated.

Using the Kraut method, the VBO between PbTe/CdTe was determined to be 0.34 eV. Previous XPS results for PbTe/CdTe(111) yielded a VBO of 0.135 eV, significantly smaller than we report here.[51] While the reported VBO here does not agree with previous XPS results, it could be related to the different crystal orientations used – (211)B for our layers. We note that theoretical results of the PbTe/CdTe(100) polar plane predicts a VBO of 0.37 eV, in good agreement with results presented here.[52]

To better understand the relationship of the valence and conduction bands at the interface, we need to develop a band alignment diagram. Once the VBO was known via the Kraut method, the Fermi levels of both semiconductors were calculated. For the PbTe:Tl film, a carrier concentration of $p \sim 6.5x10^{19}/cm^3$ results in degenerate doping concentration and thus the Fermi level was calculated following the work of Dmitriev.[53] That of the CdTe layer was determined using standard techniques for non-degenerate carrier concentrations applicable to device structures. Based on the calculated Fermi levels and the measured VBO, a first-approximation depiction of the band alignment for

PbTe:Tl/CdTe is shown in Figure 44. Note that the PbTe for this doping density is highly degenerate with a Fermi level 200 meV inside the valence band.

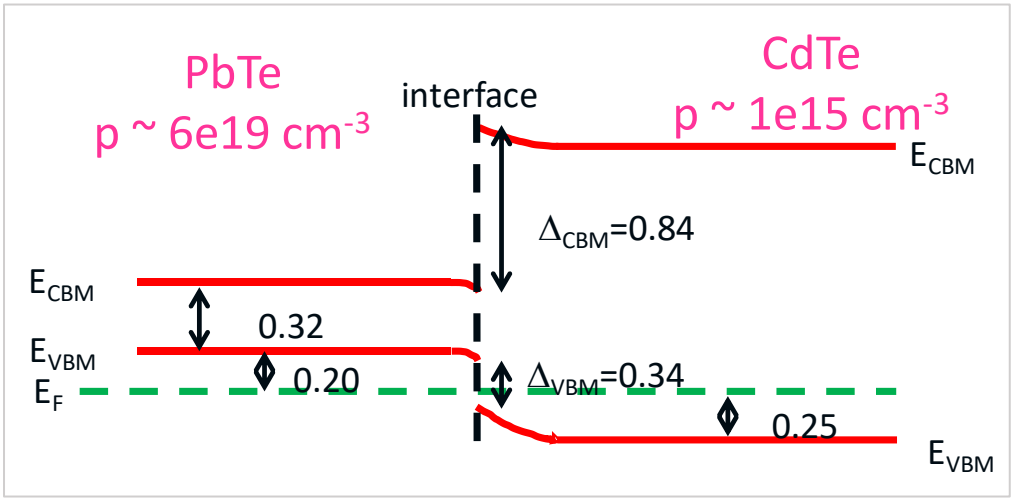

Figure 44. A rough, first approximation, hand-drawn band alignment diagram for a PbTe/CdTe interface

To maintain the measured VBO between the two materials, we see that band bending must occur at the interface. In the case of high Tl doping in PbTe, we predict that this band bending will occur in our favor, causing upwards band bending in the CdTe layer, acting as an electron reflector at the back interface, which should decrease recombination at the back of the device, while simultaneously causing downward band bending in the PbTe layer, acting as a hole injector which should increase carrier collection. We also note that there is no apparent barrier at the interface for hole transfer, suggesting ohmic contact between the two materials, at least at the high end of carrier concentrations considered in the PbTe layer.

To explore this further, we used SCAPS modeling to produce a series of band alignment diagrams with varying carrier concentrations in the PbTe:Tl layer. Recall from

section 1.2. that SCAPS modeling is based on inputted χ values and doping levels. As shown before, χ values from the literature do not accurately model the true behavior of the PbTe/CdTe interface. To use SCAPS in a meaningful way here, we assign values for χ for each material such that the real, measured VBO is reflected in the band alignment with respect to the vacuum reference. SCAPS uses carrier concentration as an input parameter and calculates the Fermi level using a non-degenerate model. In order to model degenerate PbTe using SCAPS, we inputted an artificially large carrier concentration to force calculation of the "correct" PbTe Fermi level. PbTe has a valence band effective density of states on the order of $6.5x10^{18}/cm^3$, so any carrier concentrations higher than this will likely be degenerate. The intent was to approximate the desired interface, even though some parts of the model were less than perfect, to see if predictions would match experiment results. Other inputted material parameters for CdTe, such as the relative dielectric permittivity, charge carrier thermal velocities, and charge carrier mobilities were taken from the work of Gloeckler et al.[54] In the work by Gloeckler et al, SCAPS modeling was performed to evaluate the effects of longer majority carrier lifetimes on the order of 500 ns – 1 μs. Due to this, the mobilities and thermal velocities in our SCAPS modeling may overestimate the carrier lifetimes in the CdTe films. Models that employ too large of a carrier lifetime can overestimate the efficacy of the film and subsequently, the efficacy of the device.[55] In future work, SCAPS modeling investigating the effects of carrier lifetimes may be of interest.

Using this approach we were able to not only confirm the first-approximation band alignment diagram and the subsequent band bending for the highest carrier concentration considered, we were also able to explore how the band bending at the

interface changes with varying carrier concentrations in the PbTe layer. In one SCAPS series, summarized in Figure 45, the carrier concentration in the PbTe:Tl layers was allowed to vary from $1x10^{17}/cm^3$ to $1x10^{22}/cm^3$ in a logarithmic fashion, while the CdTe layer was held at $2x10^{14}/cm^3$, relevant for industry levels associated with Cu doping in CdTe devices. For the non-degenerate carrier concentrations $1x10^{17}/cm^3$ and $1x10^{18}/cm^3$, SCAPS was able to accurately calculation the Fermi positions. In order to force a Fermi level position of -0.2 eV below the VB associated as calculated by Dmitriev, with a real carrier concentration of $6.5x10^{19}/cm^3$, which is degenerately doped, we had to input an artificially high carrier concentration of $1x10^{22}/cm^3$.[53] For the inputted carrier concentrations $1x10^{19}/cm^3$, $1x10^{20}/cm^3$, and $1x10^{21}/cm^3$, we explore the dynamics of the bands as the PbTe:Tl layer becomes degenerately doped.

In all carrier concentrations considered, there is no presence of a hole barrier in the VB. Also promising, is the existence of an electron reflector in the CB for all carrier concentrations considered, however it is clear that the effectiveness of this electron reflector is highly dependent on the carrier concentration in the PbTe:Tl layer, where the degenerately doped layers show the most electron reflection behavior. At the real carrier concentrations of $1x10^{17}/cm^3$ and $1x10^{18}/cm^3$ the electron reflector behavior in the CB may not be sufficient to adequately decrease carrier recombination at the interface. This is supported by PLI and TRPL results which show increased recombination behaviors for the lower doped PbTe:Tl layers as compared to the degenerately doped samples. SCAPS modeling also suggests a gradient in the CdTe VB that is conducive to hole injection.

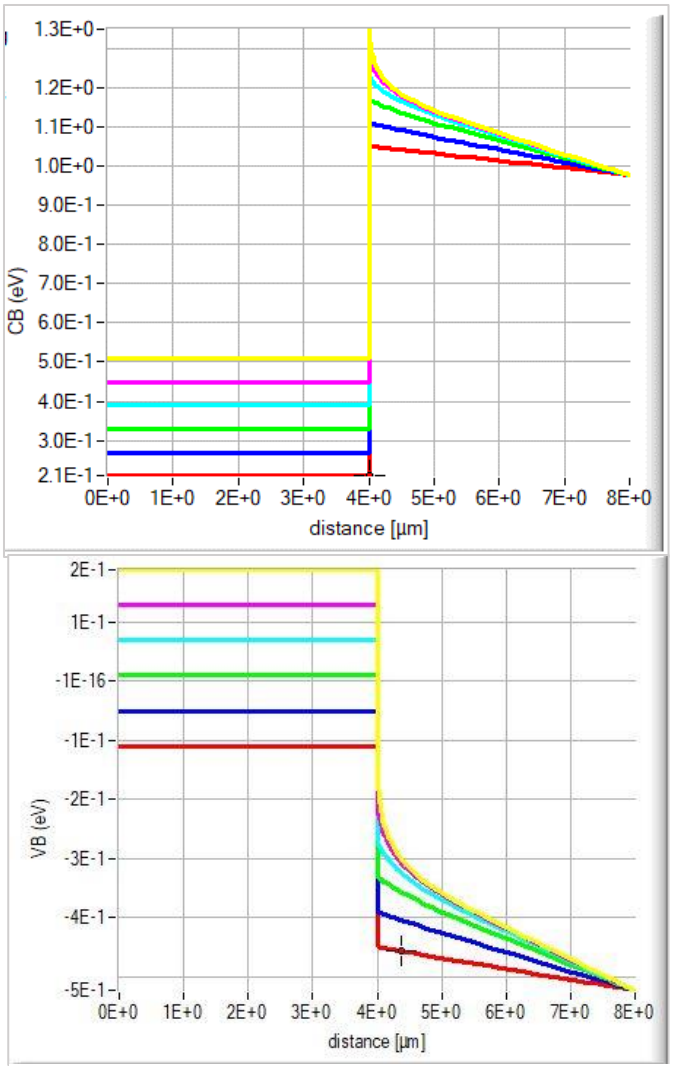

Figure 45. SCAPS modeling of PbTe/CdTe band alignment for various PbTe:Tl layer carrier concentrations, with the CdTe carrier concentration held constant at $2x10^{14}/cm^3$. *(Top) CB dynamics and (Bottom) VB dynamics are presented. The inputted PbTe:Tl carrier concentrations for each trace are: yellow - $1x10^{22}/cm^3$, pink - $1x10^{21}/cm^3$, cyan - $1x10^{20}/cm^3$, green - $1x10^{19}/cm^3$, blue - $1x10^{18}/cm^3$, red - $1x10^{17}/cm^3$.*

This model series was repeated with an increased CdTe carrier concentration of $6x10^{14}/cm^3$, closer to the condition for industry use and is summarized in Figure 46. Once again, the carrier concentrations in the PbTe:Tl layer was varied between $1x10^{17}/cm^3$ and $1x10^{22}/cm^3$. This time, we see evidence of significant hole barriers in

the VB of the CdTe layer and electron injection in the CB of the CdTe layer at PbTe:Tl with non-degenerative carrier concentrations. This sort of band structure in a device would have incredibly poor performance due hole blocking, decreasing overall current collection in the device. At degenerately doped carrier concentrations we see both hole injection and electron reflection behavior in the valence and conduction band, respectively, indicating that at those levels, increased carrier collection and decreased carrier recombination at the interface will occur. This is the ideal band bending to have to improve CdTe solar cell device design.

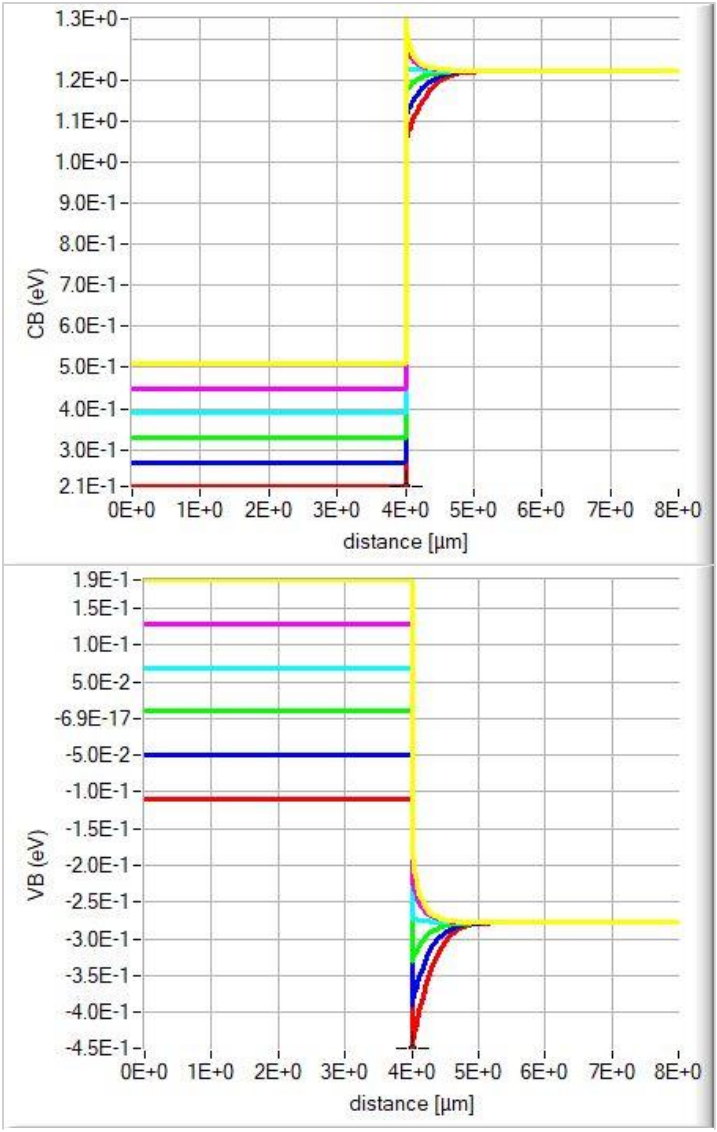

Figure 46. SCAPS modeling of PbTe/CdTe band alignment for various PbTe:Tl layer carrier concentrations, with the CdTe carrier concentration held constant at $6x10^{14}/cm^3$. *(Top) CB dynamics and (Bottom) VB dynamics are presented. The inputted PbTe:Tl carrier concentrations for each trace are: yellow - $1x10^{22}/cm^3$, pink - $1x10^{21}/cm^3$, cyan - $1x10^{20}/cm^3$, green - $1x10^{19}/cm^3$, blue - $1x10^{18}/cm^3$, red - $1x10^{17}/cm^3$.*

Finally, the highest PbTe:Tl carrier concentration was held steady at a real concentration of about $6.5x10^{19}/cm^3$ (artificially inputted as $1x10^{22}/cm^3$) while allowing the CdTe layer carrier concentration to vary. The CdTe layer was varied from

current industry standards to industry goals for increased device efficiency, that is from $2x10^{14}/cm^3$ to $2x10^{16}/cm^3$. These results are summarized in Figure 47. Here, we see that in all CdTe layer carrier concentrations considered, a PbTe:Tl back-contact

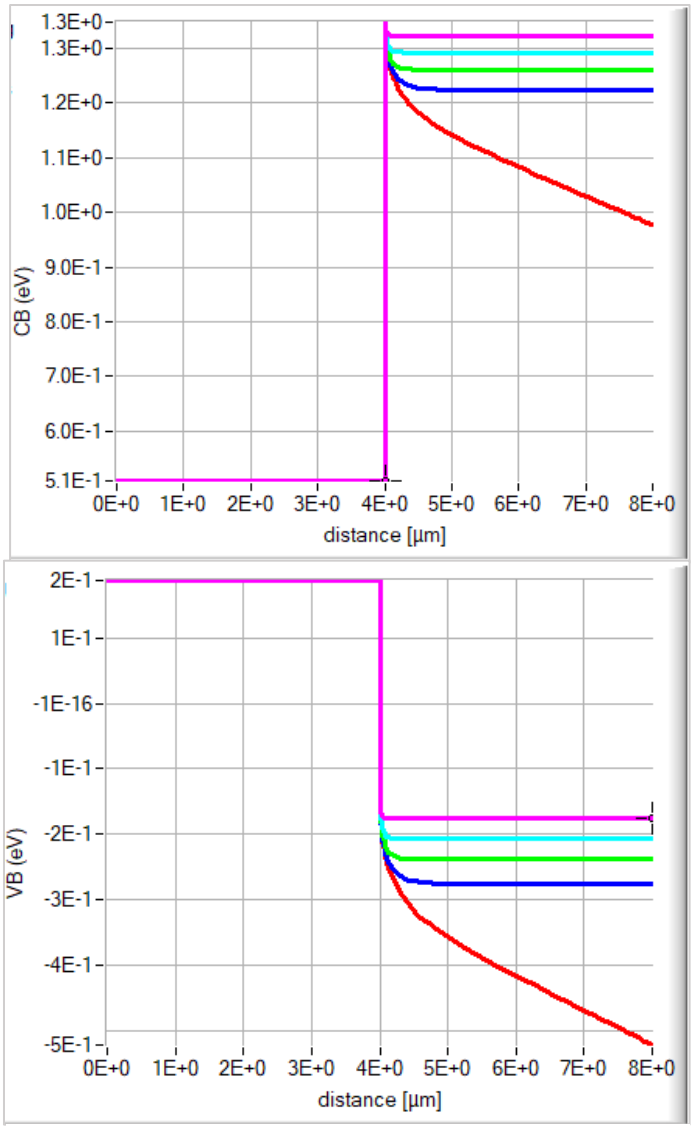

Figure 47. SCAPS modeling of PbTe/CdTe band alignment for various CdTe layer carrier concentrations, with the PbTe carrier concentration held constant at $6x10^{19}/cm^3$. *(Top) CB dynamics and (Bottom) VB dynamics are presented. The inputted CdTe carrier concentrations for each trace are: pink - $2x10^{16}/cm^3$, cyan - $6.32x10^{15}/cm^3$, green - $2x10^{15}/cm^3$, blue - $6.32x10^{14}/cm^3$, red - $2x10^{14}/cm^3$.*

buffer layer with a corresponding Fermi level of 0.2 eV below the VB appear to be appropriate for device use. Once again, we see the desired lack of a hole barrier and the presence of an electron reflector in the device. It is worth noting though that the electron reflector in the CB at higher doped CdTe layers may not be sufficient to adequately decrease carrier recombination at the interface.

One thing that still needs to be addressed here is that the XPS measurements indicated an *n-type* surface, despite the degenerate levels of p-type doping that occurred during growth and measured by Hall. This result meant that we could not directly use the XPS alignment measured for the thin heterojunction and prompted us to calculate the Fermi level positions in the first place, rather than rely on the XPS measurements of the Fermi position. Though presented last, XPS measurements were one of the first measurements performed in the study of PbTe:Tl back-contact buffer layers. This n-type surface as measured by XPS was not easily understood until the Hall investigations resulted in apparent carrier type switching. Once variable field Hall confirmed the existence of two carrier types, it was then believed that the measurement of the n-type surface via XPS was confirmation that a thin n-type layer occurs at the surface of the PbTe layer as it was consistently observed for both thick and thin heavily p-type layers. A similar n-type conduction layer was observed in a previous study of CdTe grown on PbTe.[56] In that study, it was postulated that the n-type layer only exists at the interface between the CdTe and the PbTe. However, in this study, the fact that XPS is an extremely surface sensitive technique combined with the fact that an n-type surface was measured on the PbTe layers, we postulate that the n-type layer exists on the free surface of the PbTe layer. It is important to note that at this point in time, we do not have

unambiguous proof and there will need to be further research to confirm. We do note that the XPS of the thin PbTe/CdTe sample did not suggest the potential well predicted by Jin et al.[56] Also, the clear correlation between the TRPL and PLI results support the measured VBO and would not give such agreement if there were also a large sheet of charge at the interface.

3.2 SnTe

3.2.1 Structures grown for investigations

To study the efficacy of SnTe:Tl layers in CdTe based solar cells, a similar approach was taken to that of the PbTe:Tl study. Namely, there were a variety of structures used for specific characterizations. From the onset of the investigation, it was believed that carrier concentration in SnTe:Tl films could not be controlled due to the fact that carrier concentration levels in SnTe films is dominated by intrinsic Sn vacancies in the lattice structure.[57] Limited availability of single crystal CdTe substrates did not permit for a direct investigation of this using a series of Hall structures as done in the PbTe investigation. With that being said, XPS structures and Mirror structures designed with the exact same film structure as those presented in section 3.1 with the exception that all PbTe:Tl layers became SnTe:Tl layers, were used in this study. Because an in-depth carrier concentration study could not be done, simple Hall was performed on a couple of SnTe:Tl films and showed a consistent carrier concentration of $p{\sim}1x10^{20}/cm^3$ irrespective of background Tl doping.

3.2.2 Lifetime and Recombination

In the same previous study of novel back interface preparation techniques referenced in the previous PbTe section, very preliminary TRPL results of devices using SnTe:Tl back-contact buffer layers looked promising. TRPL was repeated on a standard CdTe mirror structure to investigate the efficacy of SnTe:Tl back-contact buffer layers. All base mirror structures provided by NREL were provided from the same growth batches as those in the PbTe:Tl study.

The TRPL and PLI results of the SnTe:Tl layers are shown in Figure 48 and Figure 49, respectively. In both cases, performance of structures with SnTe:Tl layers is on par with baseline samples, providing no meaningful assessment of their inclusion in device structures. At best, we can say that from a lifetime and recombination standpoint, structures with SnTe:Tl back-contact buffer layers do not appear to negatively impact device performance.

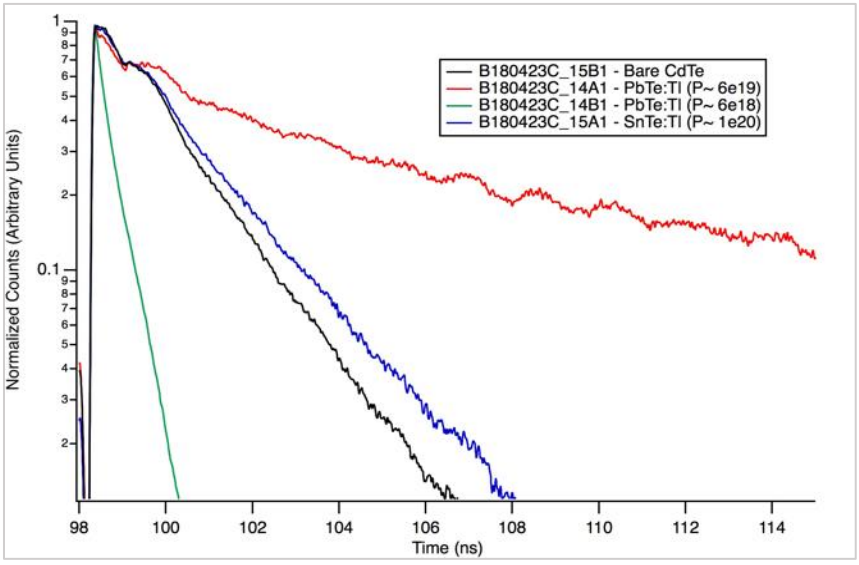

Figure 48. TRPL results of a mirror structure with SnTe:Tl back-contact buffer layer compared with the baseline results.

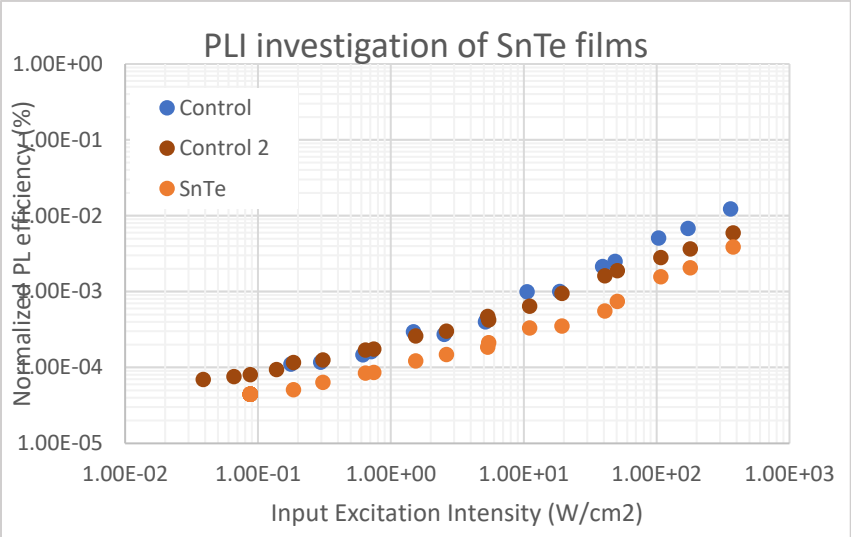

Figure 49. PLI results of a mirror structure with SnTe:Tl back-contact buffer layer as compared to the baseline samples.

3.2.3 Electrical Measurements

Due to the extenuating circumstances regarding the COVID-19 pandemic, time did not permit for a detailed investigation of device structures with SnTe:Tl back-contact buffer layers. However, in the same preliminary study referenced in the previous section, and the PbTe investigation section, JV-temperature (JVT) measurements were performed on devices with SnTe:Tl back-contact buffer layers. JVT measurements are performed the same as JV measurements, but with the sample held at various temperatures. In these measurements, the "roll-over" or saturation current is identified at each temperature test. The saturation current is given by

$$J_0(T) = AT^2 \exp\left(-\frac{\Phi_B}{kT}\right) \tag{73}$$

where J_0 is the saturation current, A is a constant, T is the temperature in Kelvin, k is the Boltzmann constant, and Φ_B is the back-contact barrier height. This expression can be rearranged for the back-contact barrier height

$$\Phi_B = -\left(\frac{\ln\left(\frac{J_0}{AT^2}\right)}{kT}\right). \quad (74)$$

Using this relation, contact barrier height can be identified as the slope of an Arrhenius plot of $J_0(T)/T^2$ vs $1/kT$. Figure 50 below comes from this study and clearly shows the roll-over present in devices with SnTe:Tl back contact buffer layers.[49] In that study, a back-contact barrier height of 0.59 eV was found for devices with SnTe:Tl back-contact buffer layers, indicating that devices with SnTe layers will have sub-optimal band alignment for carrier collection.

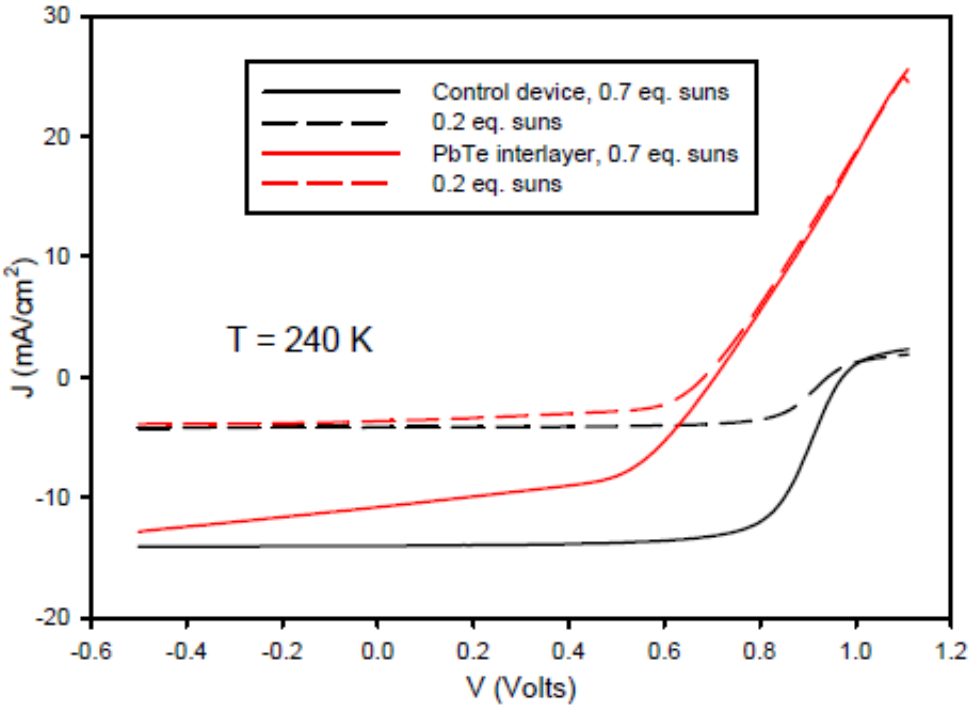

Figure 50. JV curves of devices with PbTe:Tl and SnTe:Tl back-contact buffer layers. *The SnTe:Tl curve clearly shows roll-over, indicating sub-optimal band alignment.*[49]

3.2.4 Valence Band Offsets

Using the structures specifically fabricated for this characterization, XPS was performed on single crystal SnTe:Tl/CdTe films at NREL by Dr. Craig Perkins. The Kraut method was again employed as described in the PbTe section. In this study, the Cd 3d5/2 and the Sn 3d5/2 core-level peaks were monitored and fit using ISO Standard 15472. The full spectrum survey for the thin SnTe:Tl layer is shown below in Figure 51 as an example. The VBM of both semiconductors was identified by fitting the data to a broadened, theoretically determined density of states.

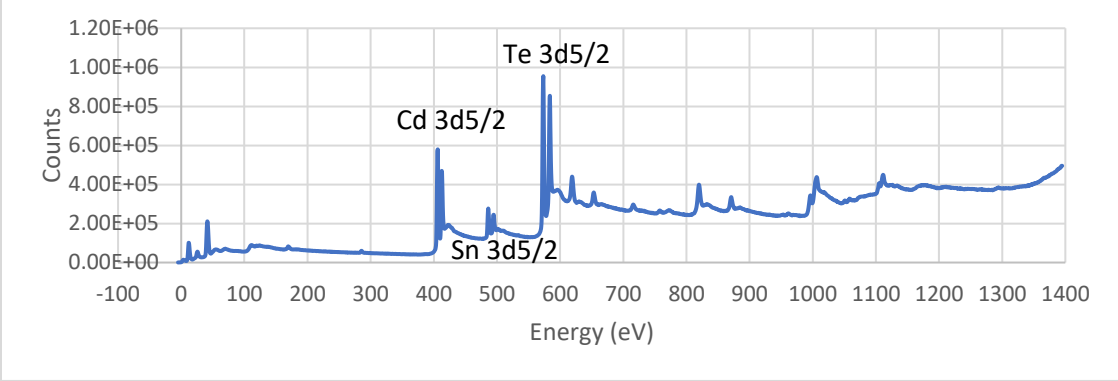

Figure 51. Full spectrum XPS survey data where the peaks of interest in determining the VBO between SnTe/CdTe have been indicated.

Employing the Kraut method, the VBO between SnTe/CdTe was determined to be 1.25 eV. To our knowledge, this is the first time the VBO between SnTe/CdTe has been directly measured via XPS. The band alignment for the SnTe:Tl/CdTe junction as measured by XPS is shown in Figure 52 for a CdTe film with a carrier concentration of $1x10^{15}/cm^3$. From this, we predict a substantial hole barrier of 0.58 eV, in excellent agreement with JVT results. Importantly, both techniques indicate that ***SnTe is not a suitable material*** for CdTe solar devices.

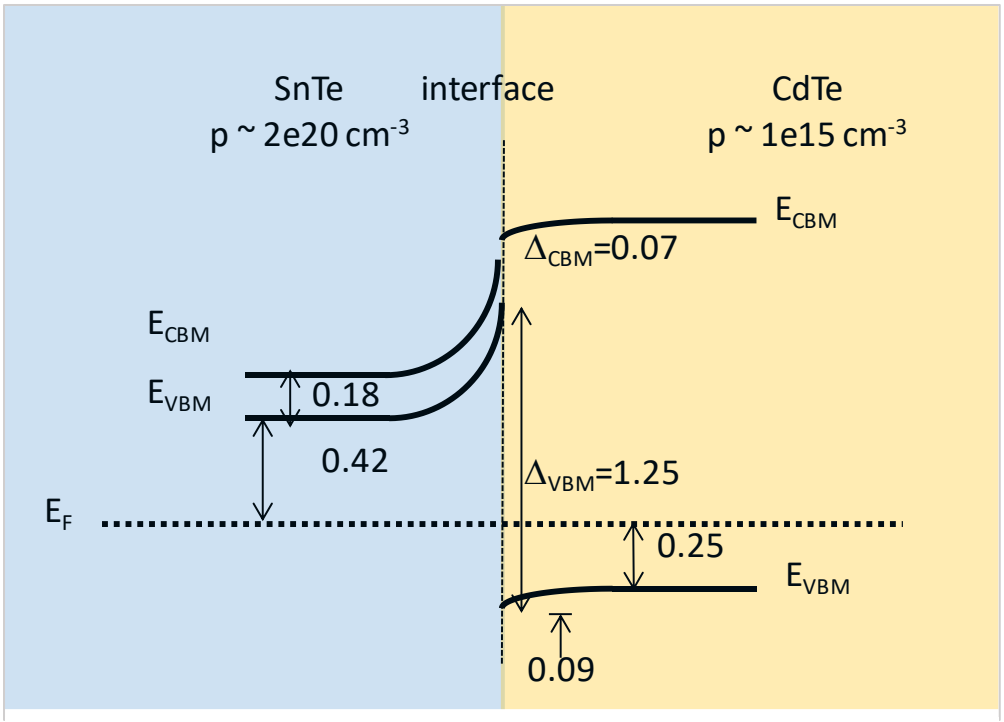

Figure 52. Band alignment diagram for SnTe/CdTe interface as measured by XPS showing a substantial hole barrier of 0.58 eV.

3.3 CdSeTe alloys

The initial investigation plan for the CdSeTe alloy series was meant to study the entire alloy range. Unfortunately, due to the COVID-19 emergency, growth of the entire series was unable to be accomplished. Presented here are the partial results of the intended series. Of note are the two binary endpoints in this investigation. Further research is needed to fill in the valence and conduction band dynamics in the mid-range of the alloy system through the region of technical relevance for solar cells; that is, in the range $0.4 < x < 0.8$ for CdSeTe alloys with the smallest band gap that can be doped p-type.

3.3.1 Growth Structure

To investigate the CdSeTe alloy series, a single sample structure was needed for complete analysis of the valence and conduction band dynamics. The general structure used was as follows: Single crystal substrate/CdSeTe alloy with uniform composition (3μm thick)/CdTe cap (30 nm thick). The CdSeTe layers were grown intentionally thick so as to encourage relaxation of the film so that strain affects could be neglected from the analysis. Due to the varying lattice parameter associated with varying Se composition, substrates of different materials were used in an effort to decrease lattice mismatch for all alloy compositions considered. This was of critical importance for higher Se composition alloys, as CdSe naturally forms a hexagonal lattice structure (the wurtzite structure), as opposed to a zinc-blende structure exhibited in CdTe. In samples where the Se composition required a higher lattice mismatch, superlattice structures consisting of six, thin, alternating layers of CdSeTe and CdSe, were introduced at the interface between the substrate and the 3 μm thick CdSeTe alloy layer to further encourage rapid relaxation of the thick film by adding interfaces where mismatch defects could collect. RHEED was crucial during this growth work to monitor the crystalline quality of the alloy growth film. As mentioned previously, InSb(100) and GaSb(100) substrates were used in this growth structure. For samples that used GaSb(100) substrates, a buffer layer of ZnTe, approximately 250 nm thick, was deposited on the substrate first. These structures are shown in Figure 53. Note that, for CdSeTe alloys with low x-values, crystal quality was kept reasonably good until $x > 0.4$. At higher Se concentrations, I was unable to obtain good crystalline quality for $x < 0.85$ It may be necessary to obtain alloy substrates to lattice-match in this region in order to grow reasonable quality CdSeTe.

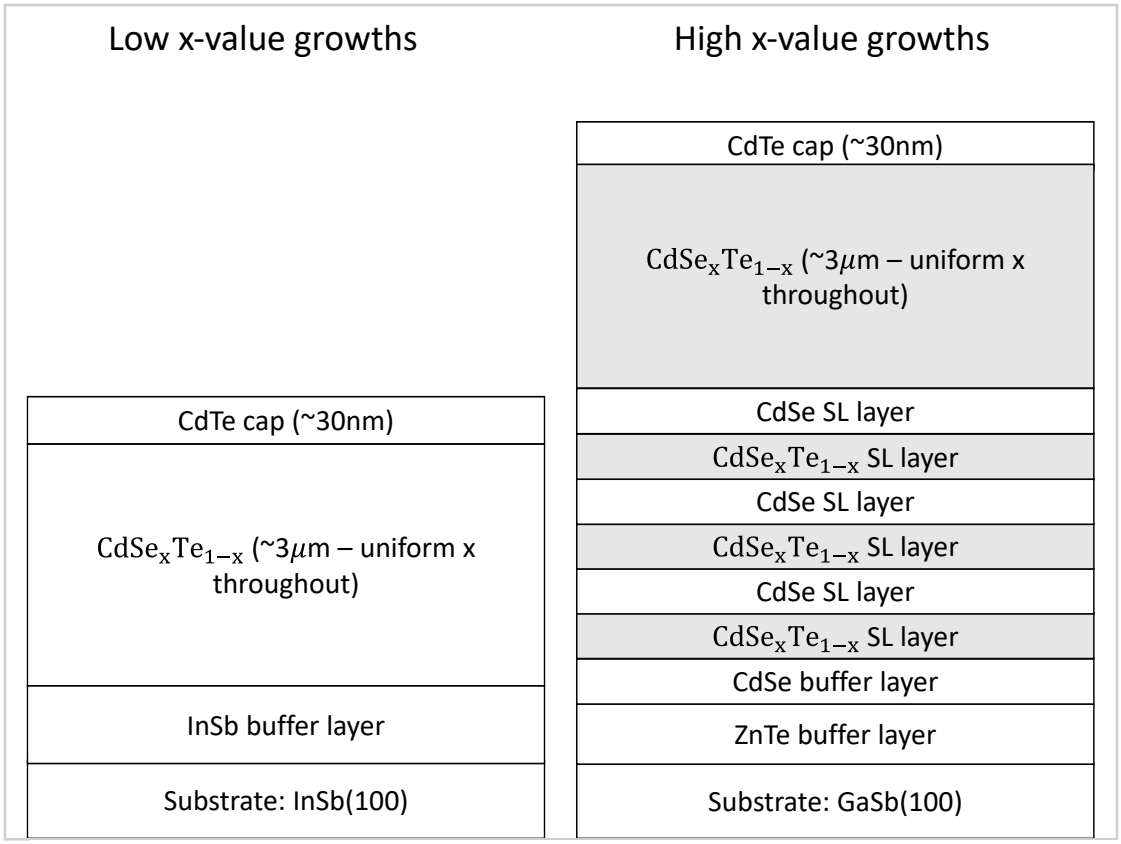

Figure 53. Growth structures used for the $CdSe_xTe_{1-x}$ alloy investigation.

3.3.2 Film thickness and Band gap determination

3.3.2.1 Ellipsometry

Accurate modeling of the layers is highly dependent on a robust material knowledge. Initially, modeling of the CdSeTe layers was done in an attempt to identify the peak in n, which is very near the band gap value, to identify the band gap of the film. Modeling in this way however, resulted in poor fits due to the novel nature of the films we were considering. This approach to determine the band gap energy was abandoned early on. Instead, the focus for ellipsometry measurements turned to determining the thickness of CdSeTe alloy layers. For materials that are less well known, a return to basic

fundamentals of thin-film interference is necessary in order to find film thicknesses. Recall Snell's law

$$n_1 \sin\theta_1 = n_2 \sin\theta_2 \tag{75}$$

which describes how light refracts as it passes through mediums with different indices of refraction, n_1 and n_2. This expression can be used to find the refraction angle, θ_t, within the film. Now recall the condition for constructive interference in thin films:

$$2nt\cos\theta_t = m\lambda_m. \tag{76}$$

Here, t is the film thickness, λ_m is the wavelength at which constructive interference occurs, corresponding to the refraction order m. This condition is simultaneously true for all integer values of m, meaning that for the $m+1$ order

$$2nt\cos\theta_t = (m+1)\lambda_{m+1} \tag{77}$$

must also be true. Eqs (76) and (77) can be rearranged to solve for m and set equal to each other such that we arrive at an expression for the thickness of the film, t

$$t\left(\frac{1}{\lambda_{m+1}} - \frac{1}{\lambda_m}\right) = \frac{1}{2n\cos\theta_t} \tag{78}$$

Using the interference fringes in the raw data, we were able to identify constructive interference peaks, and determine the film thickness of the CdSeTe films. An example of the interference fringes found in one of the CdSeTe alloy films is shown below in Figure 54. The thickness results are summarized in the following section in Table 4.

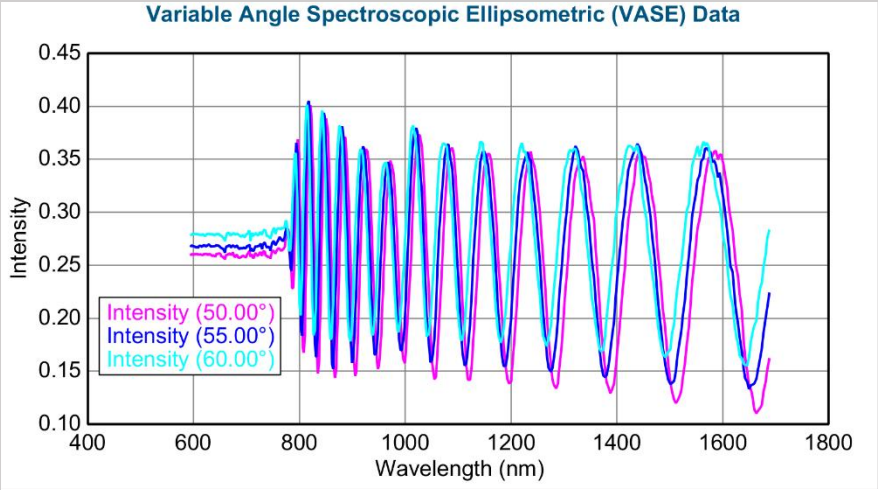

Figure 54. An example of the interference fringes in the intensity data from ellipsometry measurements for sample z-877 used to determine the film thickness

An estimate of the band gap energy of the CdSeTe film can also be found by identifying the onset of the interference fringes. This was used as a quick turn-around measurement to provide feedback for growth dynamics. There were a series of CdSeTe growths where we attempted to use varying BEP ratios of Cd, Se, and Te, separately to create our CdSeTe films. Ellipsometry on these samples showed no appreciable change in the onset of the interference fringes, indicating that the actual Se composition was not changing between growths. This was later confirmed with EDS measurements and PL spectroscopy measurements. The band gap estimates are also shown in Table 4, as well as how they compare to the band gap as determined by PL spectroscopy, in the following section.

3.3.2.2. PL spectroscopy

One of the simplest questions we sought to answer in this investigation was that of band gap dynamics through the alloy system. There is a robust history that shows that the CdSeTe alloy system exhibits band gap bowing as we move from one binary to the

other.[21,58,59,60] For a general CdX_xY_{1-x} alloy, the band gap of the alloy $E_g(x)$ can be expressed as

$$E_g(x) = xE_{g_{CdX}} + (1-x)E_{g_{CdY}} - bx(1-x) \tag{79}$$

where $E_{g_{CdX}}$ and $E_{g_{CdY}}$ represent the binary band gaps of semiconductors CdX and CdY, and b is the so called bowing parameter in eV.[61] Upon investigation of the literature, there also exists a large spread in the reported bowing parameters for this system ranging from 0.59 eV up to 0.996 eV from both theoretical and experimental approaches. [21,58,59,60] Some of these reported values are reflected in Figure 55. From this figure, we clearly see that knowing the band gap of the alloy alone is not enough information to accurately determine the composition of the alloy due to the quadratic nature of the overall band gap dynamics in the system. To complicate matters further, there also exists a spread in the reported band gap values for cubic CdSe ranging from 1.66 eV to 1.74 eV.[60]

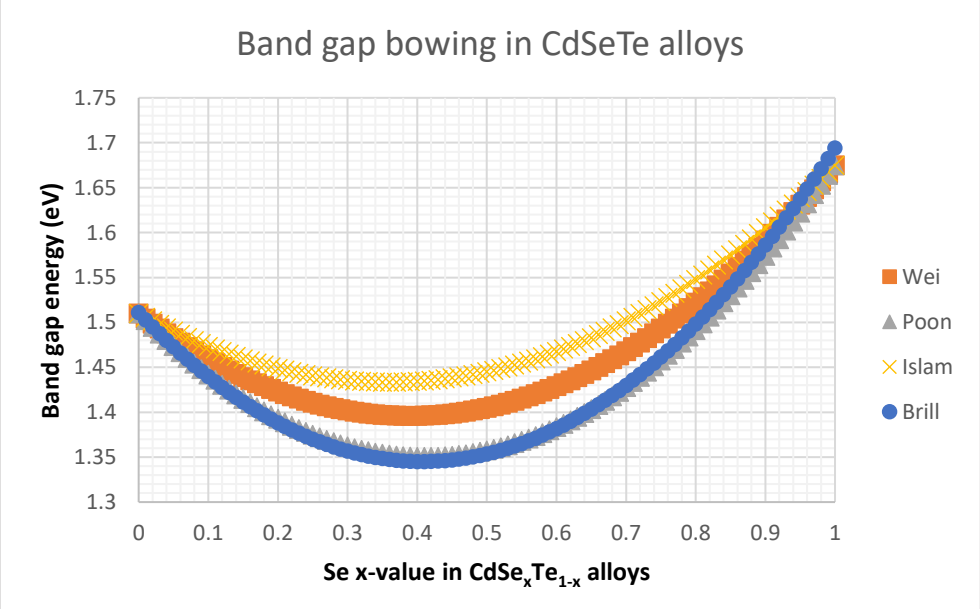

Figure 55. Summary of reported band gap bowing parameters for $CdSe_xTe_{1-x}$ alloys and band gap values of CdSe found in the literature.

Due to this wide spread of available bowing parameters, it was decided that during this study, the band gap of CdSeTe alloys would be directly measured using PL spectroscopy. As described previously, PL spectroscopy measures a photoluminescence spectrum which was then fit using a Voigt line shape. An example of PL spectrum data and subsequent fitting is shown in Figure 56. Once the peak in the PL response, λ_{peak} was identified, the band gap energy was determined by assuming the peak represents the band gap energy and the following relation was used

$$E_g = \frac{hc}{\lambda_{peak}} \tag{80}$$

where h is Planck's constant and c is the speed of light. This was performed for all samples in the series. These results are summarized in Table 4 where we have compared the band gap estimates as determined by Ellipsometry. Figure 57 below shows how the ellipsometry estimates line up with the PL spectroscopy results.

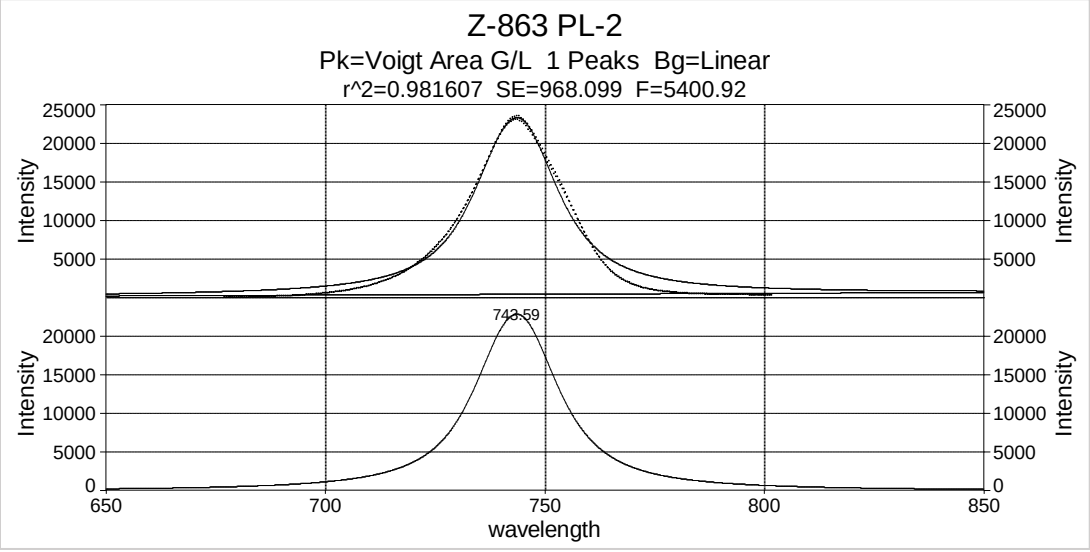

Figure 56. Example PL spectrum data and subsequent fitting.

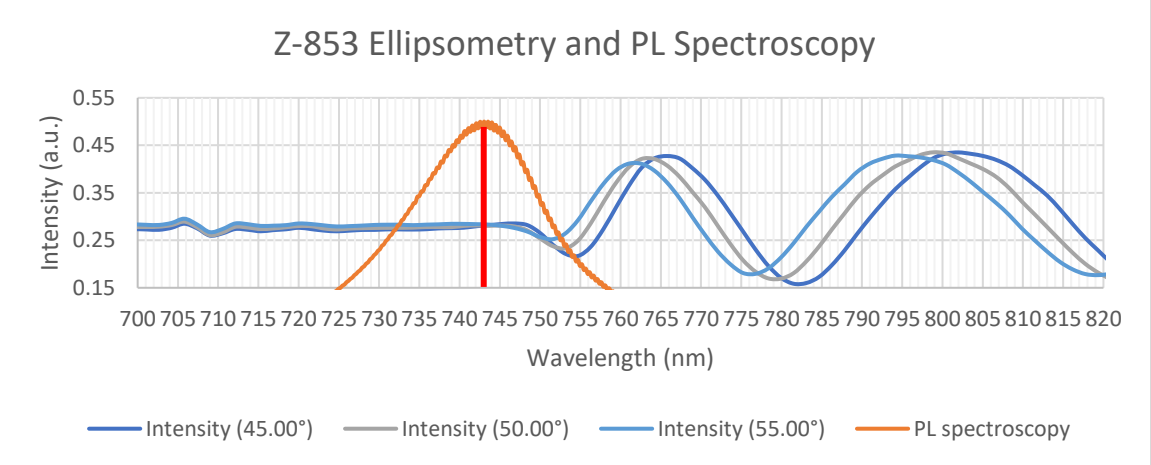

Figure 57. Comparison of the band gap value identified by PL spectroscopy and ellipsometry.

Table 4. Summary of thickness determination of CdSeTe films and band gap identification via ellipsometry and PL spectroscopy.

Sample Number	Thickness (nm)	Ellipsometry Band gap estimate (eV)	PL Spec Band gap (eV)
Z-853	2384	1.67	1.669
Z-860	1831	1.67	1.667
Z-863	1977	1.67	1.668
Z-864	2065	1.67	1.669
Z-872	2330	1.58	1.547
Z-874	3093	1.56	
Z-877	3398	1.61	1.605
Z-883	3519	1.62	

In general, we see great agreement between the ellipsometry estimates and the PL spectroscopy results. In the above table, samples with no PL spectroscopy results

reported had significant defect bands present in the PL response and clear identification of the band gap was not possible. We note that our samples consistently suggest a band gap energy of around 1.67 eV for cubic CdSe.

3.3.3 Compositional determination

To determine the Se composition in the series growths, two approaches were taken: an indirect measurement, XRD, and a direct measurement, EDS. XRD was used to determine the lattice parameter of the grown CdSeTe layer. If Vegard's law holds true in this system, then we should expect to see a linear dependence of the lattice parameter on the Se composition. These means that XRD was used as the indirect method of determining the lattice parameter. These measurements were then verified directly with quantifiable analysis of EDS measurements of the CdSeTe film.

3.3.3.1 X-ray Diffraction

Recall from the XRD section that the lattice parameter of a grown film can be determined through the following relationship

$$a_0 = \frac{\lambda\sqrt{h^2 + k^2 + l^2}}{2sin\theta} \tag{81}$$

Vegard's Law assumes a linear relationship between the lattice parameter of a ternary alloy in relation to its' two binary points. This is represented explicitly for the CdSeTe system in Figure 14, back in section 2.1.5. While the above relationship provides a path for direct lattice parameter determination, it is crucial to note that accurate determination of the lattice parameter can be extremely difficult. This is evidenced by the fact that XRD scans of different single-crystal substates of the same material produced slightly different 2θ peak positions, even after substrate peak optimization, due to slight errors in sample

alignment. To get around this error in lattice parameter, it was decided to instead evaluate the lattice mismatch between the substrate peak, serving as an internal standard, and the CdSeTe film peak. By evaluating the mismatch, we eliminate various alignment errors by using the a relative measurement of the two lattices thereby eliminating the requirement for accurate position of the individual peaks. An example XRD spectrum and subsequent fitting is shown in Figure 58. A summary of XRD results is shown in Table 5.

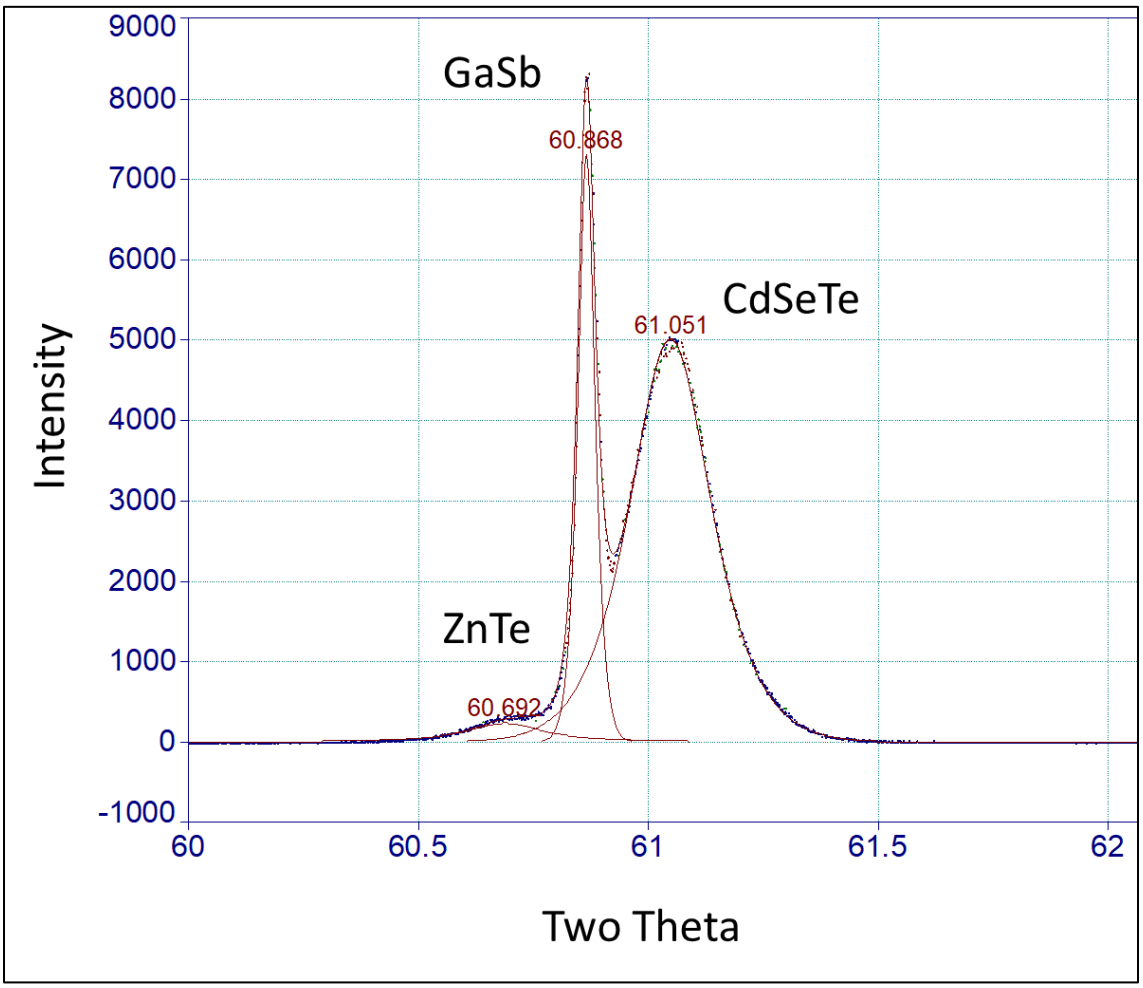

Figure 58. Example XRD spectrum data and subsequent fitting*. Here, the GaSb substrate, CdSeTe and ZnTe peaks are identified*

Table 5. Summary of XRD results determining the Se x-value in $CdSe_xTe_{1-x}$ films

Sample Number	GaSb(400) 2θ position	CdSeTe(400) 2θ position	Difference	Se x-value
z-853	60.815	60.918	0.103	0.981
z-863	60.815	60.902	0.087	0.986
z-864	60.734	60.831	0.097	0.975
z-874	60.735	60.262	-0.473	0.844
z-877	60.732	60.798	0.066	0.968
z-883	60.735	60.813	0.078	0.972

3.3.3.2 Energy Dispersive Spectroscopy

While XRD is the most commonly used technique for x-value determination, the complications of accurate peak determination and accounting for thermal expansion mismatch strain can introduce uncertainty. For a more direct method of determining the Se composition, standardized quantitative EDS was performed using single-crystal CdSe, CdTe and ZnTe standards, and analyzed with the open source NIST-DTSAII EDS software. The most accurate way to quantify an EDS spectrum is to do so with a standards-based approach where known standards are measured under the identical conditions as the unknown sample. By comparing spectra from standards taken with the same instrument, at the same working distance, and with the same beam energy, many of the less well-known fundamental parameters cancel out of the quantification equations. If the standards are similar in composition to the unknown, then the correction factors for each are typically similar and cancel regardless of magnitude.

One of the biggest advantages of x-ray generation and emission is that the process is largely dominated by properties of the elements in the material, and *not* on the chemistry that binds the elements together. This means that the shape of the x-ray line families (such as K, L, M) does not depend on the chemical nature of the element; x-rays generated from an element in form and in the presence of other elements will be shaped the same. The intensity of the x-rays emitted by an element in a material of unknown composition will be linearly proportional to the amount of that element in atomic percent in the material. Thus, by comparing the intensity of the x-rays in the unknown, by comparing the intensity of x-rays in a known standard, we should be able to deduce the composition. Castaing's first estimate of the composition, also known as the K-ratio, is this comparison of the x-ray intensities for a given element between the unknown sample and the standard,

$$K = \frac{I_{sample}}{I_{standard}} \tag{82}$$

The K-ratio can then be used to determine the composition of the element through the follow

$$C_{sample} = KC_{standard}. \tag{83}$$

To obtain a more accurate calculation of the composition, we must apply correction factors, commonly referred to as ZAF corrections. In the ZAF acronym, Z refers to corrections associated with difference in mean atomic number, back scatter efficiency, and subsequent electron stopping power. The back scatter correction compensates for x-ray generation last because higher mean atomic number atoms backscatter more electrons than those of lower atomic number, while the electron stopping power is related to the

energy lost by an electron due to passing through the valence shell of the material. A refers to corrections associated with differences in x-ray absorption based on the material, which accounts for the fact that x-rays emitted by a certain element will be poorly absorbed by atoms of the same element, but may be strongly absorbed by other elements present in the sample. If the x-ray is strongly absorbed by other elements, then F corrects for differences in the production of secondary x-rays or x-ray fluorescence, that is the emission of x-rays due to the absorption of characteristic x-rays emitted by another element. Further discussion of these correction factors is beyond the scope of this dissertation however it is important to note that these correction factors were applied by the NIST-DSTAII EDS software used in this study.

For this study, the Cd, Se, and Te compositions were determined in our CdSeTe samples. Specifically, the CdSe standard was used to identify the x-ray line shapes associated with Cd and Se transition energies, as well as provide intensities for a known stoichiometric substance. The ZnTe standard was used to identify the Te x-ray line shapes as well as the intensity associated with a 50 atm% Te material. The CdTe standard was less useful here, as the Cd and Te transitions overlap and thus clearly identification of the necessary line shapes was not possible. An example spectrum is shown in Figure 59 below comparing the spectra of the unknown to the CdSe and ZnTe standard spectra, while the results of quantitative EDS analysis are summarized in Table 6.

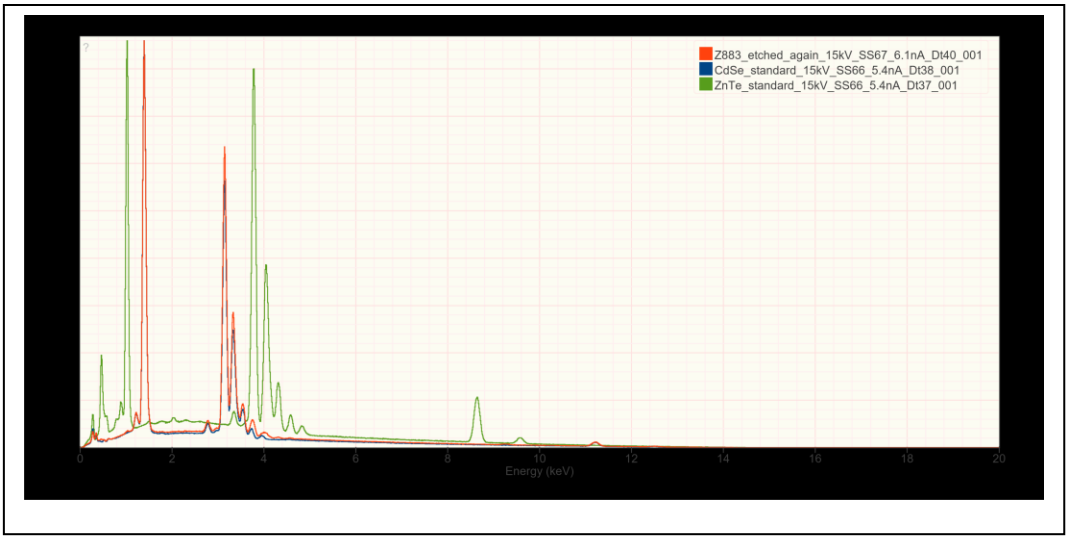

Figure 59. EDS spectrum data example with standard spectra shown for comparison.

Table 6. Summary Se x-values as determined by EDS for $CdSe_xTe_{1-x}$ films.

Sample	Se x-value	Uncertainty
z-813	0.186	±0.0074
z-853	1.0	±0.002
z-864	0.991	±0.0014
z-872	0.936	±0.0054
z-874	0.884	±0.0062
z-877	0.932	±0.0048
z-883	0.949	±0.003

By comparing the Se x-values found in Table 5 using XRD and Table 6 using EDS, we see quite a bit of discrepancy between the two. Specifically, we see that the XRD technique both under and over-estimates some of the Se x-values compared with the results from EDS. This may be explained by the fairly large thermal expansion

coefficient mismatch between GaSb and CdSe. To our knowledge, the thermal expansion coefficient for CdSe has not been measured or reported in the literature. But we can make predictions on its value based on trends in other materials. For instance, the thermal expansion coefficient for the materials ZnS, ZnSe, and ZnTe gets progressively larger as we move from the sulfide, selenide, and telluride materials. Based on calculations of elastic constants, it is reasonable to assume that a similar trend can be found for the CdS, CdSe, and CdTe materials, indicating that the thermal expansion coefficient for CdSe should be about the same as either endpoint.[62] Thus, if the CdSe film is relaxed at growth temperature, due to the large thermal expansion mismatch between CdSe and the GaSb, the film will be compressed after it cools to room temperature. It is plausible then, that the out of place lattice parameter of the CdSe film as measured by XRD is shifted to accommodate this. To use XRD more accurately, an in-plane measurement (asymmetric reflection) is likely needed.

3.3.4 Valence Band Offsets

Low x-value CdSeTe growth structures in this investigation were initially sent to the University of Malaga in Spain for XPS characterization using the equipment described in the XPS section of this dissertation. This initial work was performed by Dr. Tom Myers and collaborating researcher Dr. Dietmar Leinen at the University of Malaga. Se x-value in these samples were determined using EDS, XRD, and cathodoluminescence. All three techniques agreed within $\Delta x \sim 0.01$. As mentioned in the PbTe and SnTe investigations, the Kraut method for determining the VBO between two materials is the most common method used. The energy positions of the core-levels can be determined with high accuracy by applying an appropriate peak fitting procedure.

However, the correct position of the VBM must be determined with care. There are two common methods used to determine the VBM: one is the linear extrapolation of the low-binding energy edge of the valence band, and the other is the comparison of the experimental spectrum with an appropriately broadened theoretically determined density of states, as performed in the PbTe and SnTe investigations. Both methods however can lead to a significant uncertainty in the energy position for the VBM. The difficulties associated with accurate determination of the VBM are described in detail by List et al.[63]

Determining VBOs within an alloy system bring its own challenges, but also offers potential advantages. For example, ternary alloy systems have one component that is present throughout the full range of the alloy system from one binary endpoint to the other. In the CdSeTe system, that common elemental component is Cd. If the Cd core-level is deep enough, alloying should not change its binding energy (BE) position. Perusal of the XPS literature suggests that the Cd 3d5/2 core-level is significantly less, it at all, perturbed by chemical bonding than that of either Te or Se core-levels. A good example is the difficulty in using the Cd 3d5/2 position to identify the chemical state – indeed, the Cd MNN is recommended as a better choice to look for chemical shifts.[64] Also, the Cd 3d5/2 peak occurs at essentially the same energy in CdTe and CdSe, according to the NIST XPS database.[65] The same cannot be said for Te or Se, which typically exhibit significant chemical shifts. Thus, if the Cd 3d5/2 BE remains constant throughout the alloy, it can serve as an internal reference point allowing us to account for the effects of changes in surface band bending, as well as serve as a reference level in the alloy to allow determination of VB shift directly without the need of the complication of a HJ.

Two approaches were taken to determine the constancy of the Cd 3d/52 BE. In the first, the peak widths of the various core-levels were measured as we sputtered through a HJ. This was done for several CdTe/CdSeTe and CdTe/CdMgTe (not studied in this dissertation but discussed in detail here to illustrate the robustness of this approach) HJs. Since the XPS signal will come equally from both the binary and the alloy near the HJ, if there is a significant peak shift related to the differing chemical environment, we will see the FWHM broaden in the region of the interface. For the CdTe/CdMgTe HJ, the Cd 3d5/2 FWHM varied by 15 meV on average, and for the CdTe/CdSeTe HJ the FWHM varied an average of only 5 meV. These results were comparable to the broadening observed for the Mg 1s and Se 3d FWHM's, averaging 13 meV and 7 meV respectively, both of which originate on only one side of the interface and should therefore exhibit no broadening. In contrast, the Te 3d5/2 averaged a 37 meV increase in FWHM at the CdTe/CdMgTe HJ and a 9 meV increase at the CdTe/CdTeSe HJ.

The measured shift in the Cd 3d5/2 BE was then used to correct for the energy shifts due to surface band bending as the HJ was etched through. Figure 60 shows the shift in the as-measured and corrected VB the Mg 1s BE in the CdTe/CdMgTe HJ while Figure 61 shows the same for the VB and Se 3d energies in the CdTe/CdSeTe HJ. Based solely on the as-measured data there seems to be a shift in the Mg and Se energies in the HJ. However, using the measured shift in the Cd 3d5/2 energy to correct for shifts due to the surface band bending dynamics we can see that both the Mg 1s and the Se 3d energies are actually constant, as they should be, and there is less structure in the VB energy as we pass through the HJ. Not shown is the effect on the Te 3d5/2 BE – once corrected for any surface potential shifts, there was a 37 meV shift to higher energy in passing through the

CdTe/CdMgTe HJ and a 17 meV shift to lower energy in the CdTe/CdSeTe HJ. This is consistent with the larger FWHM observed for the Te 3d5/2 peak at the HJ.

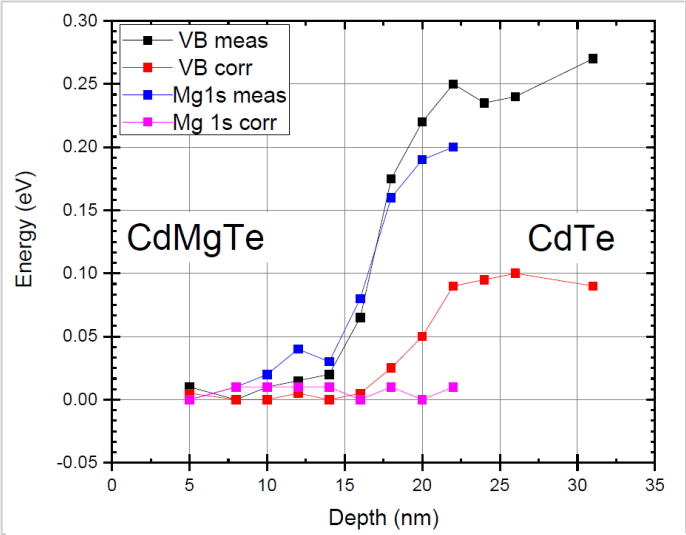

Figure 60. XPS data, both raw and corrected, for the VB and the Mg 1s peak energies in a CdTe/CdSeTe heterojunction. *Once corrected using the shifts in energy observed in the Cd 3d5/2 peak, the Mg peak is constant, as expected.*

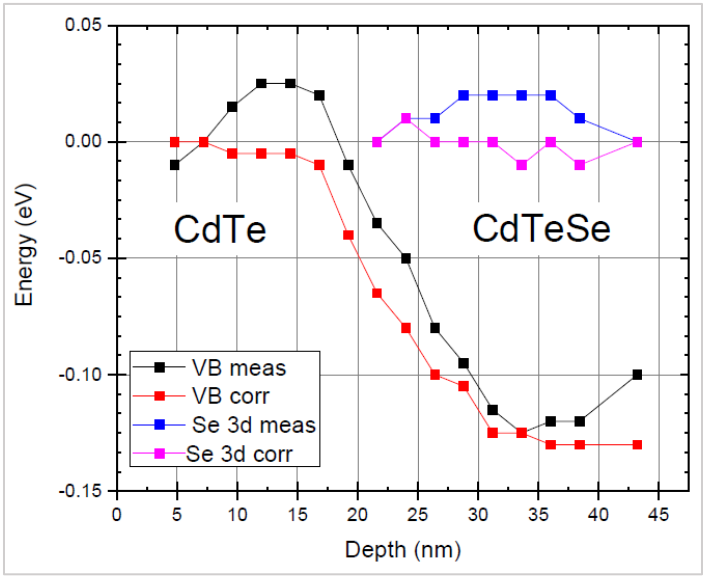

Figure 61. XPS data, both raw and corrected, for the VB and the Se 3d5/2 peak energies in a CdTe/CdSeTe heterojunction. *Once corrected using the shifts in energy observed in the Cd 3d5/2 peak, the Se peak is constant, as expected.*

With band bending correctly accounted for by using the Cd 3d5/2 peak as a reference, the need to determine the exact position of the VBM is removed through utilizing the similarity of the valence band in the alloy and allows one to measure the VBO directly. This can be done in one of two different ways, both requiring alignment of the two VB spectra to a common point. First, one can shift the one of the spectra so that the VB spectra line up and overlap on the low energy side.[66] This is illustrated in Figure 62. The VBO can then be measured directly as the (apparent) difference in peak energy between the two Cd 3d5/2 peaks. The other option is to line up the Cd 3d/52 peaks of the two spectra, then perform a least-squares fit of the VBM edges for both spectra, identify the 50% point for both VB edges, and measure the energy difference between the two.

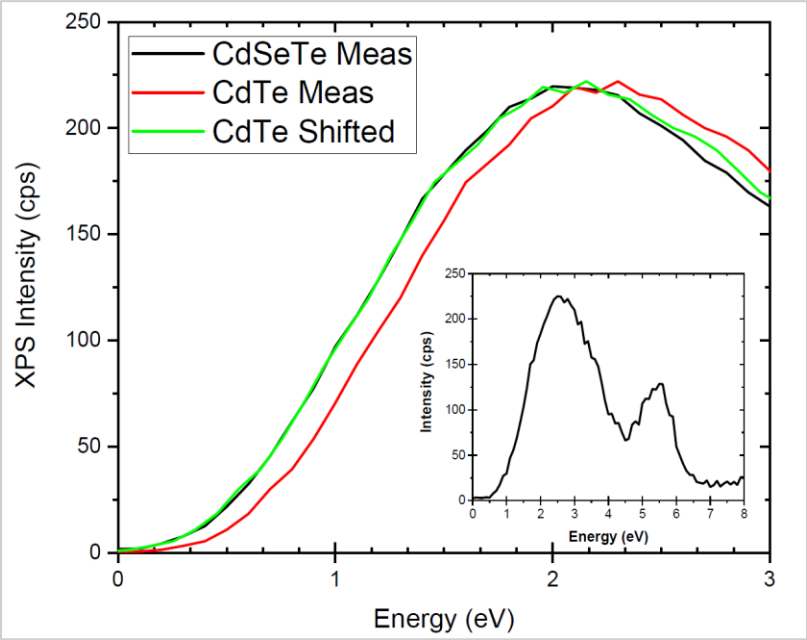

Figure 62. VB spectra example, illustrating manually shifting one spectrum so that the two line up. *With the VBs lined up, the VBO can be determined directly as the apparent difference in energy of the Cd 3d5/2 peaks. The inset shows a more complete valence band spectrum for CdTe illustrating higher order structure.*

Both methods were performed on spectra acquired under both Ar+ and C_{60}^{+} etching. To assess the robustness of the relative shifts in energies, the Cd 3d5/2 peak was also fitted using two methods. First, fitting was performed according to ISO Standard 15472 on the Cd 3d5/2 peak, and the VBO was determined by both shifting the balance band and by determining the 50% points. This analysis was performed a second time, using mixed Lorentzian-Gaussian fitting for the Cd 3d5/2 peak. A standard deviation of 4 meV was observed in the results of analyzing the corrected VBO between these techniques, indicating that as long as the same technique is used in determine the difference, either approach could be used for correcting the shifts in surface band bending and establishing energy difference. Everything discussed so far in this section is based off of work by the author and others that has been accepted for publication in Applied Surface Science. The VBO results of this work are summarized in Table 7.

Table 7. Summary of $CdSe_xTe_{1-x}$/CdTe VBOs determined via XPS at University of Malaga in Spain using the modified ternary technique discussed above.

Se x-value (±0.01)	**VBO (eV) Ar^+ (±0.03)**	**VBO (eV) C_{60} (±0.03)**
0.118	-0.062	-0.061
0.118	-0.059	-0.066
0.190	0.040	-0.040
0.190	-0.044	
0.195	-0.030	-0.069
0.195	-0.035	-0.049
0.314	-0.084	-0.119
0.314	-0.095	-0.101
0.365	-0.132	-0.114
0.365	-0.114	-0.129

Once we were confident that the above approach was valid and consistent, it was intended that this approach would be repeated on as many CdSeTe samples as possible, with the author traveling to the University of Malaga to aid in data acquisition. As mentioned at the beginning of this chapter though, extenuating circumstances related to the COVID-19 emergency did not allow for a full characterization of the entire series, nor did it allow for travel. To the VBO at the high Se x-value range, a select set of samples

were sent to ThermoFisher for XPS analysis. The procedure outlined above was provided to ThermoFisher to guide data acquisition. With the software provided by ThermoFisher to analyze results, a quicker method was used to analyze the data. In this instance, the depth profile was analyzed to determine the CdTe region and the CdSeTe region. Once these regions were identified, the peak energy of the Cd 3d5/2 peak energy was averaged together for each region and the difference was found for the CdTe region and the CdSeTe region. Then, the VBM was normalized and averaged for each corresponding region and plotted together. The 50% points were identified, and a difference was taken. The difference in the 50% points and the difference in Cd 3d5/2 peak energies were then added together to determine the VBO. While this technique did potentially introduce a little more uncertainty in the results, the speed at which the analysis could be performed was vital for completion of this dissertation work. Results for these samples are shown in Table 8.

Table 8. Summary of $CdSe_xTe_{1-x}$/CdTe VBOs determined by XPS performed at ThermoFisher.

Sample number	**EDS Se composition**	**VBO with CdTe**
Z-853	1.0	-0.474
Z-877	0.932	-0.451
Z-883	0.949	-0.481

By plotting these three data points and performing a linear fit to estimate the dependence over this limited compositional range, we estimate a VBO between CdSe and CdTe of -0.478 eV. This fit is shown below in Figure 63. Also shown, are two lines

representing a variance of 0.015 eV from this fit, illustrating that the data falls between these bounds suggesting the uncertainty is reasonable.

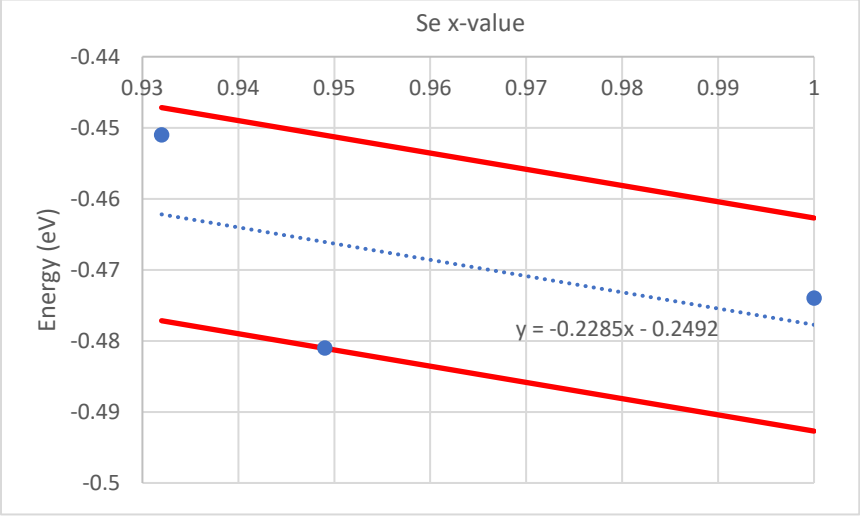

Figure 63. Linear fit of the VBOs of the three high x-value $CdSe_xTe_{1-x}$ films to determine the CdSe/CdTe VBO. *Also shown in red are estimates of the variance of ±0.015eV.*

In addition to the above results from ThermoFisher, another sample, Z-887 was also analyzed. This sample had a structure of: GaSb(100) substrate/ZnTe (~600nm)/CdSe (~50nm)/CdTe(~50nm). The intention for this growth structure was to try to find both the VBO between CdTe/CdSe, and to find the VBO between CdSe/ZnTe. However, growth of this structure did not go as planned, as Zn was detected by XPS throughout the structure. This was likely due to insufficient time to allow the Zn furnace to cool before initiating the growth of the subsequent layers. Because of this, the (intended) CdSe layer was actually CdZnSe, and the offsets with CdSe could not be determined. However, we applied the same procedure as outlined above to look at the VBO between CdTe/ZnTe and found a VBO of -0.040 ±0.030 eV. While this relatively small VBO does not support the recent theoretical calculation, theory has gone back and forth over the years.

Experimental results of the VBO however, have remained on the order of -0.05±0.05 eV for quite some time. Angle-resolved synchrotron radiation measurements of MBE grown ZnTe on CdTe(100) substrates measured a VBO of 0.00±0.05 eV.[67] XPS measurements of ZnTe deposited via thermal evaporation on CdTe found a VBO of -0.05±0.1 eV.[68] XPS measurements of sputtered ZnTe on CdTe found a VBO of -0.1±0.05 eV.[69] Our results for the VBO between ZnTe/CdTe agree nicely with all of these, within experimental uncertainty.

3.3.5 Valence and Conduction Band Variation through the alloy series.

At this point we can finally put everything together to get a clear picture of the valence and conduction band dynamics. All results have been summarized in Table 9 and put together to create a (partial) band alignment profile diagram for a graded CdSeTe alloy layer and how the bands relate to the CdTe bands in Figure 64.

Table 9. Summary of all $CdSe_xTe_{1-x}$/CdTe VBOs as measured by XPS both at the University of Malaga and at ThermoFisher. **Indicates data that was not directly measured but estimated using the band gap bowing parameter presented by Brill which fits well in this region of the alloy range.*

Se x-value	**VBO (eV) Ar^+**	**VBO (eV) C_{60}**	**VBO (eV) ThermoFisher**	**CBO (eV)**
$(\pm \mathbf{0.01})$	(± 0.03)	(± 0.03)	(± 0.03)	
0.118	-0.062	-0.061		-0.144*
0.118	-0.059	-0.066		-0.141*
0.19	-0.04	-0.04		-0.158*
0.19	-0.044			-0.162*
0.195	-0.03	-0.069		-0.150*
0.195	-0.035	-0.049		-0.155*
0.314	-0.084	-0.119		-0.241*
0.314	-0.095	-0.101		-0.252*
0.365	-0.132	-0.114		-0.295*
0.365	-0.114	-0.129		-0.277*
0.932			-0.451	-0.356
0.949			-0.481	
1.0			-0.474	-0.315

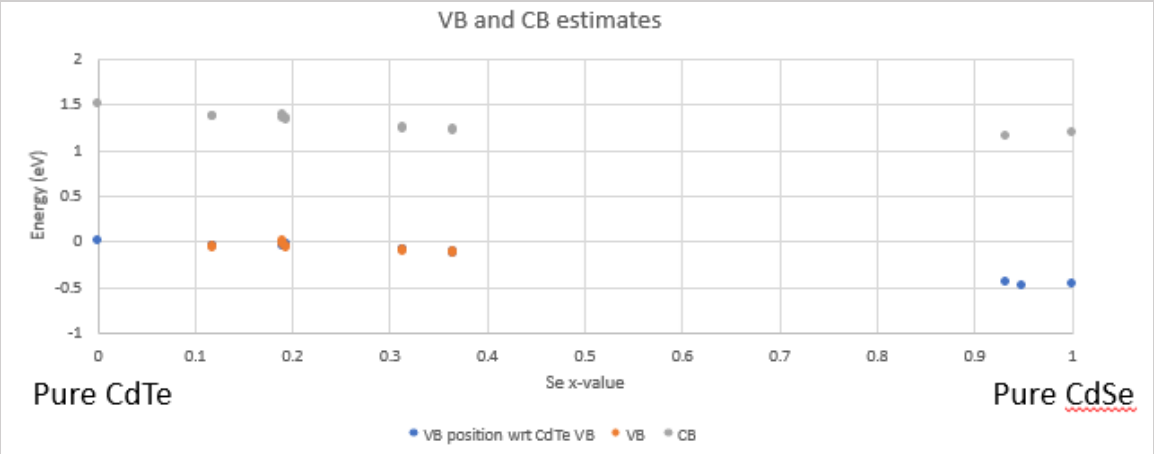

Figure 64. Rough estimate of VB and CB dynamics as we move through the $CdSe_xTe_{1-x}$ alloy series.

From this, we see that the CB and VB change at approximately the same rate, though with more movement in the VB overall. This means that as we move from pure CdSe to pure CdTe, the VB and CB steadily rise, indicating the presence of an internal electric field that both acts as a hole injector and an electron reflector for the CdTe layer. These dynamics are ideal for p-type carrier collection in the CdTe layer. However, due to the large gap in the data, one needs to be cautious about what happens in that region. Figure 65 provides more insight. Here, the data collected in this work is compared with others found in the literature, as well as a theory calculation of the VB dynamics for the entire CdSeTe alloy range.[27,70] From this, we see our data fit very well with the recent theory calculations, lending significant credence to both the calculation and our results, which indicate a VBO between CdTe/CSe of -0.478 eV.

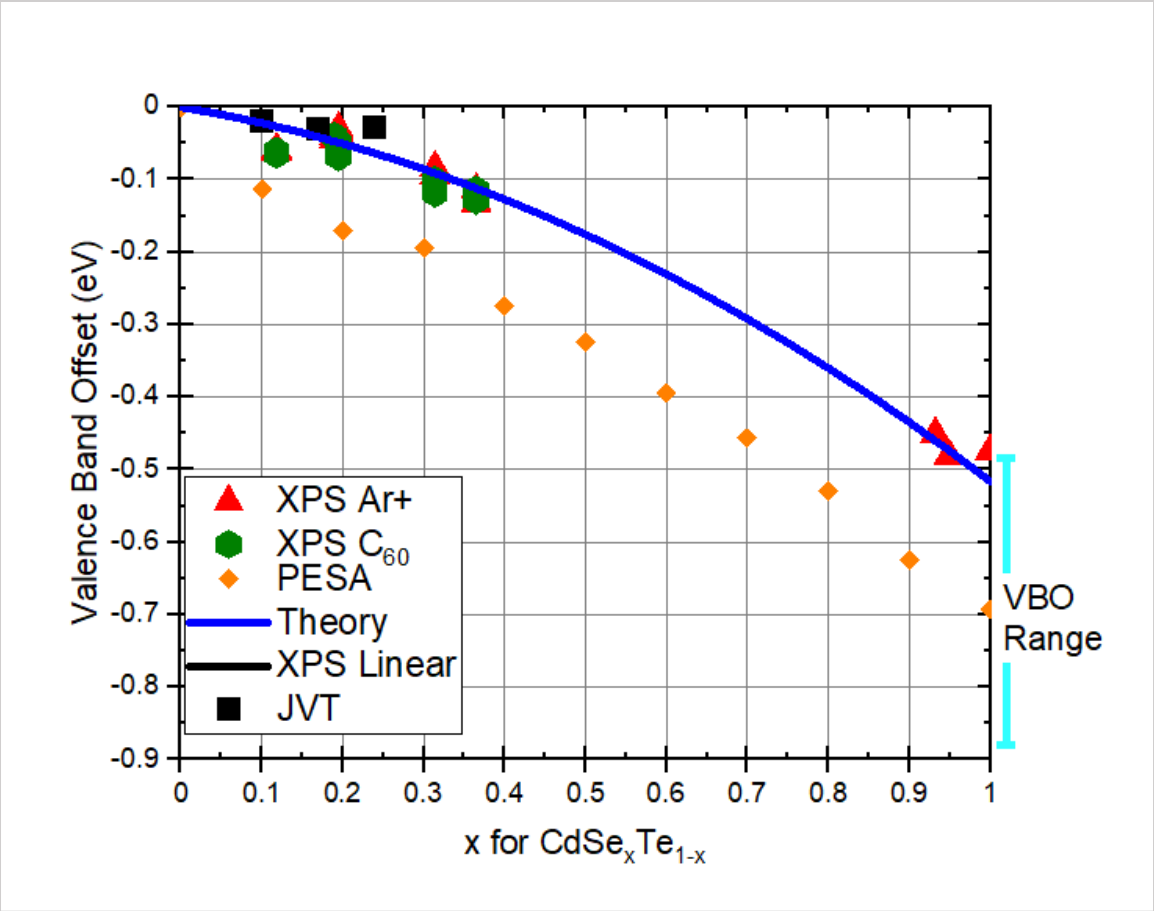

Figure 65. VB dynamics determined from VBOs of $CdSe_xTe_{1-x}$/CdTe heterojunctions.

4. CONCLUSIONS

Through the course of this work, there are several notable conclusions to make. Let's begin with the PbTe:Tl back-contact buffer layer investigation. While establishing carrier concentration control in PbTe films, it was discovered that a two-dimensional n-type layer exists in the film which remains fairly constant at a level of $1x10^{13}/cm^2$ regardless of intended p-type doping. While the location of this layer has not been unambiguously determined, XPS results showing an n-type surface on both thick and thin heavily p-type PbTe:Tl films suggests that it exists on the free surface of the PbTe film.

Using the Kraut method, XPS was used to identify a VBO between PbTe and CdTe of 0.34 eV. This VBO, in conjunction with modified SCAPS modeling, was then used to calculate band alignment diagrams, which indicated band bending in a desired configuration for some of the carrier concentrations considered. Specifically, we found that for a CdTe device with carrier concentration of $p{\sim}2x10^{14}/cm^3$, PbTe:Tl films will cause hole injecting and electron reflecting band bending behaviors in the CdTe VB for all carrier concentrations of the PbTe:Tl considered. This is an ideal configuration for use in CdTe-based solar cells. It is worth noting that the hole injecting and electron reflecting behaviors for the PbTe:Tl layers that are non-degenerate may not be sufficient to reduce carrier recombination at the back interface.

For a more aggressively doped CdTe layer with carrier concentration $p{\sim}6x10^{14}/cm^3$, the dynamics of the VB and CBs is highly dependent on the carrier concentration in the PbTe:Tl film. For PbTe:Tl films with degenerate doping levels, we see the desired hole injecting and electron reflecting behaviors in the CdTe layer. For non-degenerate doping levels however, we see the opposite: hole blocking and electron

injecting behavior in the CdTe layer. This suggests that at this level of CdTe carrier concentration, non-degenerate doping levels in the PbTe:Tl layer would negatively impact overall device performance as it will lead to increased recombination at the back interface while simultaneously blocking collection of the majority charge carrier.

Finally, we saw that if the CdTe layer carrier concentration is allowed to vary between $2x10^{14}/cm^3$ and $2x10^{16}/cm^3$, and we apply a PbTe:Tl back contact buffer layer with a real carrier concentration of $p{\sim}6.5x10^{19}/cm^3$, the device exhibits the desired band bending behavior for increased device efficiency: both electron reflection and hole injection occurs at all CdTe carrier concentrations. It is worth noting that the hole injection and electron reflection behaviors exhibited in the highest doped CdTe layer may not prove sufficient to decrease recombination at the interface. While highly dependent on the carrier concentrations in the films, all of this leads us to conclude that PbTe:Tl back-contact buffer layers can be advantageous for use in CdTe solar cell devices, but careful consideration of the carrier concentrations in both layers is necessary.

TRPL on mirror structures with carrier concentrations of $p{\sim}6.5x10^{19}/cm^3$show increased lifetimes over bare CdTe structures. This is supported by PLI results showing decreased recombination behavior in structures with the same carrier concentrations. This also agrees well with the JV results showing improved device performance with the highest doped PbTe:Tl back-contact buffer layers. In addition, TRPL and PLI results agree well with SCAPS modeling which predicts a more effective electron reflector (and less recombination behaviors) for higher carrier concentrations in the PbTe:Tl layer. The improvement in roll-over in JV measurements with increased doping in the PbTe:Tl layer agrees well with the SCAPS modeling and the XPS VBO determination as well.

Future work on PbTe:Tl films should focus on electrical characterizations. Specifically, more device structures with PbTe:Tl films need to be made to allow for more JV measurements to be taken. By repeating this over a large sample set, more meaningful comparisons can be made between the performance of device with and without PbTe:Tl films. As a follow up, a JVT study would provide nice information about the presence or absence of a hole barrier. Particularly, a study on devices with similar carrier concentrations as those provided in the SCAPS simulations would be of utmost benefit.

SnTe:Tl back-contact buffer layers tell a very different story than that provided by the PbTe:Tl investigation. Initial TRPL results show increased lifetimes, however this seems to be the only area of improvement for these devices. A VBO of 1.25 eV was found between SnTe and CdTe, with a substantial hole barrier of 0.59 eV. To our knowledge, this is the first time this VBO has been directly measured or reported. This hole barrier would act to reflect holes back into the absorber layer of mirror structures, explaining why lifetimes would increase. However this hole barrier is detrimental to carrier collection in solar cell devices, and thus, we conclude that SnTe:Tl films are not appropriate for use in CdTe devices.

While the COVID 19 pandemic limited the course of the CdSeTe alloy investigation, significant results were obtained that describe the basic evolution of the VBO in this system. Through this work, we found that ellipsometry proved to be a useful tool, both for determining the film thickness, as well as providing a first estimate for the band gap value of the CdSeTe alloy layer. PL spectroscopy was able to provide a more accurate determination of the band gap, but the quick turnaround associated with

ellipsometry provided critical feedback for growth conditions. Standards-based quantitative EDS also provided the most accurate means of determining the alloy composition. While XRD measurements of the out-of-plane lattice parameter provided estimates of the Se x-value that were in the ballpark of x-values determined by EDS, these measurements only provide a first estimate of the composition. The discrepancy in the XRD measurements is likely due to the fairly large linear thermal expansion coefficient mismatch between GaSb and CdSe. For a more accurate determination of Se content using XRD, an in-plane measurement is likely needed.

Most note-worthy is the development of an alternative method for determining how the VBOs can be measured in ternary alloys that exhibit VB similarity. Namely, if a core-level, present throughout the system, is deep enough so as to not be affected by alloying, then it can serve as an internal reference point, negating the need to determine the exact position of the VBM, a significant source of error when employing the Kraut method. With this internal reference level identified, one can then take any apparent changes in this energy level to correct for band bending induced by the changes in the surface of the material as the junction is etched through. The VBO can then be measured directly in one of two ways. One may either line up the spectra to the internal reference point, perform a least squares fit on the VBM, identify the 50% points and measure the VBO as the difference, or one may line up the spectra to the VBM and measure the VBO as the apparent difference in energy of the internal reference energy level. This technique proved particularly robust, yielding an uncertainty on the order of ± 0.03 eV. The VBO between CdTe and CdSeTe for $0 < x < 0.4$ and for $x > 0.9$ were found. Using a linear fit of the high x-value VBOs, we predict a VBO between CdTe/CdSe of -0.478 ± 0.03

eV. As a bonus, we also measured the VBO between CdTe and ZnTe to be -0.040 ± 0.03 eV, which agrees well with other measured values reported in the literature.

For the CdSeTe series, it appears that the CB and VB change at about the same rate, though with more movement in the VB. This means that as we move from pure CdSe to pure CdTe, the VB gradually moves upwards, as does the CB. This gradual change in the band as we move through the grading implies the existence of an internal electric field through the layer that aids in both hole injection and electron reflection from the CdTe layer. This internal electric field is ideal for p-type carrier collection. VBO measurements in the region of technical relevance ($0 < x < 0.4$), that is, the region with the smallest band gap that can be doped p-type, show only small changes from the VB of CdTe. Due to this, any back-contact work on CdTe should also be relevant to the technologically important CdSeTe alloy contacts. Since the VBO for ZnTe is nearly VB neutral with CdTe, it should make for a better contact to $x \sim 0.3 - 0.4$ CdSeTe alloys. Future research should focus on the gap in the data presented here. Specifically, significant effort needs to be dedicated to growing high quality CdSeTe alloy films in the mid-range $(0.4 < x < 0.8)$. This may only be possible by obtaining CdSeTe substrates produced from ingot growth. Once growth of these films can be achieved, continuing the band gap determinations and the VBO determinations through this mid-range will greatly enrich the knowledge of this material system.

REFERENCES

[1] Fraunhofer Institute for Solar Energy Systems, *PHOTOVOLTAICS REPORT* (2019).

[2] K.A.W. Horowitz, R. Fu, X. Sun, T. Silverman, M. Woodhouse, and M.A. Alam, *An Analysis of the Cost and Performance of Photovoltaic Systems as a Function of Module Area* (2017).

[3] G. Fonthal, L. Tirado-Mejía, J.I. Marín-Hurtado, H. Ariza-Calderón, and J.G. Mendoza-Alvarez, J. Phys. Chem. Solids **61**, 579 (2000).

[4] W. Shockley and H.J. Queisser, J. Appl. Phys. **32**, 510 (1961).

[5] S. Uličná, P.J.M. Isherwood, P.M. Kaminski, J.M. Walls, J. Li, and C.A. Wolden, Vacuum **139**, 159 (2017).

[6] K. Durose, P.R. Edwards, and D.P. Halliday, J. Cryst. Growth **197**, 733 (1999).

[7] Z. Fang, X.C. Wang, H.C. Wu, C.Z. Zhao, Z. Fang, X.C. Wang, H.C. Wu, and C.Z. Zhao, Int. J. Photoenergy **2011**, 1 (2011).

[8] B.L. Williams, J.D. Major, L. Bowen, L. Phillips, G. Zoppi, I. Forbes, and K. Durose, Sol. Energy Mater. Sol. Cells **124**, 31 (2014).

[9] A. Luque and S. Hegedus, *Handbook of Photovoltaic Science and Engineering* (2011).

[10] A. Kahn, Mater. Horizons **3**, 7 (2016).

[11] S. Jeetendra, C.S. Naveen, P. Raghu, and H.M. Mahesh, Int. J. Eng. Res. Technol. **3**, 431 (2014).

[12] J.H. Yang, S. Chen, W.J. Yin, X.G. Gong, A. Walsh, and S.H. Wei, Phys. Rev. B - Condens. Matter Mater. Phys. **79**, (2009).

[13] K.W. Mitchell, C. Eberspacher, F. Cohen, J. Avery, G. Duran, and W. Bottenberg, Sol. Cells **23**, 49 (1988).

[14] J. Si, S. Jin, H. Zhang, P. Zhu, D. Qiu, and H. Wu, Appl. Phys. Lett. **93**, (2008).

[15] M. Burgelman, P. Nollet, and S. Degrave, *Modelling Polycrystalline Semiconductor Solar Cells* (n.d.).

[16] M.A. Matin and M. Dey, in *2014 Int. Conf. Informatics, Electron. Vis.* (IEEE, 2014), pp. 1–5.

[17] A.J. Strauss, J. Electron. Mater. **2**, 553 (1973).

[18] T. Shu, Z. Ye, P. Lu, L. Chen, G. Xu, J. Zhou, and H. Wu, EPL **116**, (2016).

[19] X. Zheng, D. Kuciauskas, J. Moseley, E. Colegrove, D.S. Albin, H. Moutinho, J.N. Duenow, T. Ablekim, S.P. Harvey, A. Ferguson, and W.K. Metzger, APL Mater. **7**, 071112 (2019).

[20] N.R. Paudel and Y. Yan, Appl. Phys. Lett. **105**, (2014).

[21] S.-H. Wei, S.B. Zhang, and A. Zunger, J. Appl. Phys. **87**, (2000).

[22] M. Ribeirão, L.R.C. Fonseca, T. Sadowski, and R. Ramprasad, in *J. Appl. Phys.* (2012).

[23] Y.H. Li, A. Walsh, S. Chen, W.J. Yin, J.H. Yang, J. Li, J.L.F. Da Silva, X.G. Gong, and S.H. Wei, Appl. Phys. Lett. **94**, (2009).

[24] Y. Hinuma, A. Grüneis, G. Kresse, and F. Oba, Phys. Rev. B - Condens. Matter Mater. Phys. **90**, (2014).

[25] J.J. Li, X. Liu, S. Liu, S. Wang, D.J. Smith, D. Ding, S.R. Johnson, J.K. Furdyna, and Y.H. Zhang, Appl. Phys. Lett. **100**, (2012).

[26] J. Jasieniak, M. Califano, and S.E. Watkins, in *ACS Nano* (2011).

[27] B.I. MacDonald, A. Martucci, S. Rubanov, S.E. Watkins, P. Mulvaney, and J.J. Jasieniak, ACS Nano (2012).

[28] E. KASPER, Le J. Phys. Colloq. **49**, C4 (1988).

[29] M.A. Herman and H. Sitter, *Molecular Beam Epitaxy: Fundamentals and Current Status* (Springer-Verlag, Heidelberg, Germany, 1989).

[30] J.F. Klem, J.Y. Tsao, J.L. Reno, A. Datye, and S. Chadda, J. Vac. Sci. Technol. A **9**, 2996 (1991).

[31] R.F. C Farrow, G.R. Jones, G.M. Williams, and I.M. Young, Appl. Phys. Lett. **39**, (1981).

[32] N. Samarth, H. Luo, J.K. Furdyna, S.B. Qadri, Y.R. Lee, A.K. Ramdas, and N. Otsuka, Appl. Phys. Lett **54**, 2680 (1989).

[33] M.E. Straumanis and C.D. Kim, J. Appl. Phys. **36**, 3822 (1965).

[34] H.M. Wang, J.H. Chang, T. Hanada, K. Arai, and T. Yao, J. Cryst. Growth **208**, 253 (2000).

[35] K.K. Lee, K. Doyle, J. Chai, J.H. Dinan, and T.H. Myers, J. Electron. Mater. **41**, 2799 (2012).

[36] J.F. Moulder, W.F. Stickle, P. Sobol, and K. Bomben, *Handbook of X-Ray Photoelectron Spectroscopy* (Perkin-Elmer Corporation, Eden-Prarie, MN, 1979).

[37] C.L. Perkins, S.H. Lee, X. Li, S.E. Asher, and T.J. Coutts, J. Appl. Phys. **97**, (2005).

[38] C.J. Powell, Surf. Interface Anal. **23**, 121 (1995).

[39] W.H. Bragg and W.L. Bragg, Proc. R. Soc. London. Ser. A, Contain. Pap. a Math. Phys. Character **88**, 428 (1913).

[40] C. Kittel, *Introduction to Solid State Physics*, 8th Edition (Wiley & Sons, 2004).

[41] M. (PicoQuant G. Wahl, Tech. Note 1 (2014).

[42] A. Kanevce, D.H. Levi, and D. Kuciauskas, Prog. Photovoltaics Res. Appl. **22**, 1138 (2014).

[43] D. Griffiths and R. College, *Introduction to Electrodynamics* (1999).

[44] D. Gonçalves and E.A. Irene, Quim. Nova **25**, 794 (2002).

[45] S.J. Allen, F. Derosa, C.J. Palmstrm, and A. Zrenner, Phys. Rev. B **43**, 9599 (1991).

[46] I. Vurgaftman, J.R. Meyer, C.A. Hoffman, D. Redfern, J. Antoszewski, L. Faraone, and J.R. Lindemuth, J. Appl. Phys. **84**, 4966 (1998).

[47] J. Wittenburg, *Kinematics: Theory and Applications* (Springer, Heidelberg, Germany, 2006).

[48] C.H. Swartz, J.E. Petersen, E.W. Welch, and T.H. Myers, J. Electron. Mater. **45**, 722 (2016).

[49] C.H. Swartz, S.R. Rab, S. Paul, M.F.A.M. van Hest, B. Dou, J.M. Luther, G.F. Pach, C.R. Grice, D. Li, S.S. Bista, E.G. LeBlanc, M.O. Reese, M.W. Holtz, T.H. Myers, Y. Yan, and J. V. Li, Sol. Energy **189**, 389 (2019).

[50] S. Siol, J.C. Hellmann, S.D. Tilley, M. Graetzel, J. Morasch, J. Deuermeier, W. Jaegermann, and A. Klein, ACS Appl. Mater. Interfaces **8**, 21824 (2016).

[51] J. Si, S. Jin, H. Zhang, P. Zhu, D. Qiu, and H. Wu, Cit. Appl. Phys. Lett **93**, (2008).

[52] R. Leitsmann and F. Bechstedt, Phys. Rev. B - Condens. Matter Mater. Phys. **76**, 125315 (2007).

[53] A. V. Dmitriev, J. Appl. Phys. **123**, (2018).

[54] M. Gloeckler, A. Fahrenbruch, and J. Sites, in *3rd Wolrd Conf. Photovolt. Energy Convers.* (Osaka, 2003), pp. 491–494.

[55] J.N. Duenow and W.K. Metzger, J. Appl. Phys. **125**, (2019).

[56] S. Jin, C. Cai, G. Bi, B. Zhang, H. Wu, and Y. Zhang, Phys. Rev. B - Condens. Matter Mater. Phys. **87**, 235315 (2013).

[57] L.A. Hemstreet, Phys. Rev. B **12**, 1212 (1975).

[58] H.C. Poon, Z.C. Feng, Y.P. Feng, and M.F. Li, J. Phys. Condens. Matter **7**, 2783 (1995).

[59] R. Islam, H.D. Banerjee, and D.R. Rao, Thin Solid Films **266**, 215 (1995).

[60] G. Brill, Y. Chen, P.M. Amirtharaj, W. Sarney, D. Chandler-Horowitz, and N.K. Dhar, in *J. Electron. Mater.* (Springer New York LLC, 2005), pp. 655–661.

[61] S.-H. Wei, S.B. Zhang, and A. Zunger, J. Appl. Phys. **87**, (2000).

[62] E. Deligoz, K. Colakoglu, and Y. Ciftci, Phys. B Condens. Matter **373**, 124 (2006).

[63] R.S. List and W.E. Spicer, J. Vac. Sci. Technol. B Microelectron. Nanom. Struct. **6**, 1228 (1988).

[64](n.d.).

[65] A. V. Naumkin, A. Kraut-Vass, S.W. Gaarenstroom, and C.J. Powell, Meas. Serv. Div. Natl. Inst. Stand. Technol. **20899**, 20899 (2012).

[66] D. Eich, D. Hübner, K. Ortner, L. Kilian, R. Becker, G. Landwehr, R. Fink, and E. Umbach, Appl. Surf. Sci. **166**, 12 (2000).

[67] D. Rioux, D.W. Niles, and H. Höchst, J. Appl. Phys. **73**, 8381 (1993).

[68] B. Späth, J. Fritsche, A. Klein, and W. Jaegermann, Appl. Phys. Lett. **90**, 062112 (2007).

[69] B. Späth, J. Fritsche, F. Säuberlich, A. Klein, and W. Jaegermann, in *Thin Solid Films* (Elsevier, 2005), pp. 204–207.

[70] J. Yang and S.-H. Wei, Chinese Phys. B **28**, 086106 (2019).

[71] N.W. Ashcroft and D.N. Mermin, *Solid State Physics* (Saunders College Publishing, 1976).

[72] S.M. Sze and K.K. Ng, *Physics of Semiconductor Devices* (John Wiley & Sons, Inc., Hoboken, NJ, USA, 2006).